

СЗ45к(07)

p-59



Учебно-  
методические  
пособия  
Учебно-научного  
центра ОИЯИ  
Дубна

УНЦ-2013-55

D. Dinev

HIGH ENERGY HEAVY ION ACCELERATORS

2013

Joint Institute for Nuclear Research  
University Centre

C 345K(07)  
D-59

D. Dinev

HIGH ENERGY HEAVY ION ACCELERATORS

*Textbook*

151406

Dubna 2013

НАУЧНО-ТЕХНИЧЕСКАЯ  
БИБЛИОТЕКА  
ОИЯИ

Reproduced directly from the author's original.

**Dinev D.**

D59 High energy heavy ion accelerators: Textbook. — Dubna: JINR, 2013. — 106 p.: ill.

ISBN 978-5-9530-0375-9

This book is devoted to the problem of acceleration of heavy ion beams to high energies. It starts with a brief review of the sources of heavy ions. The structure of the high energy heavy ion accelerator complex is discussed. Basic for the book is the description of the physical processes that are essential for the accelerator performance. These processes are: interaction of the accelerated ions with the residual gas molecules and atoms and with stripping foils deliberately intercepting the ion trajectories, ion induced vacuum pressure instability, intrabeam scattering, electron cloud effects and nuclear interactions that are specific for the colliding ultra-relativistic ion beams. These phenomena determine to a great extent the achievable parameters of the ion accelerator and the quality of the accelerated ion beams. The second part of the book is dedicated to the main accelerator systems. The specific features of the magnetic system and of the systems for injection, extraction and acceleration when the accelerated particles are heavy ions are discussed. The last chapter enlightens the ion colliders.

**Динев Д.**

Ускорители тяжелых ионов высоких энергий: Учебное пособие. — Дубна: ОИЯИ, 2013. — 106 с.: ил.

ISBN 978-5-9530-0375-9

Книга посвящена проблемам ускорения пучков тяжелых ионов до высоких энергий. Она начинается кратким обзором источников тяжелых ионов. Подробно обсуждается структура ускорительного комплекса тяжелых ионов. Основным в книге является описание физических процессов, которые определяют специфику ускорения тяжелых ионов: взаимодействие ионов с молекулами и атомами остаточного газа в камере ускорителя и с перезарядными мишенями, вызванная ионами нестабильность давления, внутривидовое рассеяние ионов, эффект электронного облака, процессы при ядерных взаимодействиях ультрарелятивистских пучков тяжелых ионов в ионных коллайдерах. Эти процессы в значительной мере определяют параметры ускорителя ионов и качество ускоренных ионных пучков. Вторая часть книги посвящена основным системам ускорителя. Обсуждаются особенности магнитной системы и систем инжекции, ускорения и вывода в случае ускорения тяжелых ионов. Последний параграф книги посвящен ионным коллайдерам.

**TABLE OF CONTENTS**

INTRODUCTION	5
PART I. BASIC PRINCIPLES AND PHYSICAL PROCESSES	7
I.1. VARIANTS OF A HIGH ENERGY HEAVY ION ACCELERATOR COMPLEX	7
I.1.1. General Remarks	7
I.1.2. Sources of Heavy Ions	7
I.1.3. Variant of the High Energy Heavy Ion Accelerator Complex with a High Current, Low Charge State Injector	10
I.1.4. Variant of the High Energy Heavy Ion Accelerator Complex with Injector of Heavy Ions in Medium Charge State, working in dc mode	15
I.1.5. Variant of the High Energy Heavy Ion Accelerator Complex with Injector of Heavy Ions in High Charge States, working in a Short Pulses Mode	17
I.2. PHYSICAL PROCESSES TYPICAL FOR HEAVY ION ACCELERATORS	19
I.2.1. Interaction with Residual Gas and Stripping Foils	19
I.2.1.1. Electron Loss	19
I.2.1.2. Electron Capture	22
I.2.1.3. Interaction with the Residual Gas and Beam Lifetime	24
I.2.1.4. Evolution of the Ion Charge State; Equilibrium Charge State Spectrum	26
I.2.1.5. Energy Loss	31
I.2.1.6. Elastic Scattering	32
I.2.2. Dynamic Vacuum Problems	34
I.2.3. Intrabeam Scattering	38
I.2.4. Electron Cloud Effects	43
I.2.5. Processes in Nuclear Interactions of Ultra-Relativistic Heavy Ions	47
PART II. ACCELERATOR SYSTEMS	49
II.1. MAGNETIC LATTICE	49
II.2. INJECTION	57
II.2.1. Single-Turn Injection	57
II.2.2. Multiturn Injection with Betatron Stacking	58
II.2.3. Multiturn Injection with Stacking in Both Horizontal and Vertical Phase Spaces	60
II.2.4. Beam Stacking with RF Acceleration	61
II.2.4.1. Principle of RF Stacking	61
II.2.4.2. Longitudinal Phase Space Topology	63
II.2.4.3. Stacking Cycle	64
II.2.4.4. Combination of Multiturn Injection and RF Stacking	65
II.2.4.5. RF Stacking Example	66

II.2.5. Combined Longitudinal and Transverse Multiturn Injection	67
II.2.6. Ion Accumulation by Stacking with Electron Cooling	68
II.2.7. Barrier Bucket Accumulation	70
II.3. Extraction	74
II.3.1. Fast Extraction	74
II.3.2. Resonant Extraction	75
II.3.3. Stochastic Resonant Extraction	82
II.3.4. RF Knock-Out Extraction	83
II.3.5. Extraction by Betatron Core	84
II.4. RF system	85
II.4.1. Ferrite Cavities	86
II.4.2. Magnetic alloy (MA) Cavities	87
II.4.3. Storage RF System	89
II.4.4. Double RF System	90
II.4.5. Transition Crossing	91
II.4.6. Superconducting Cavities	92
II.5. Ion Colliders	93
II.5.1. Luminosity	94
II.5.2. Beam-Beam Interaction	98
II.5.3. Luminosity Lifetime	100
References	102

## INTRODUCTION

Historically the investigations with accelerated beams of heavy ions began with nuclear structure studies and with synthesis of new transuranium elements. For these experiments one needs ion energies, which lie slightly above the Coulomb barrier. Tandems, linear ion accelerators and cyclotrons were used at the early times of research with heavy ion beams. Very soon the scientific interest broadened toward more deep and sophisticated experimental studies in the fields of atomic and nuclear physics and applications in cancer therapy.

When the available ion energy surpassed the 1 GeV/u threshold studies of the nuclear equation of states and search for very hot and dense nuclear matter and for phase transitions began.

The acceleration of heavy ions to high energies, i.e. to more than 1 GeV/u, is done by synchrotrons. For energies above about 10 GeV/u the fixed target mode becomes inefficient and colliding of heavy ion beams must be used.

The first synchrotrons accelerating ions, Synchrophasotron at JINR, Bevatron at LBNL and Saturn-II at Saclay, were proton machines converted to ion synchrotrons. The first two machines were weak focusing accelerators. The upgrade included improvement of the vacuum and building of new injectors but in spite of these measures only bare nuclei could be accelerated due to the poor vacuum conditions. The maximum energies were: 1.15 GeV/u for Saturn-II, 2.1 GeV/u for Bevatron and 4.2 GeV/u for Synchrophasotron. All the three machines are already out of operation.

After the successful demonstration that heavy ions could be accelerated in proton synchrotrons the AGS at BNL and the SPS at CERN started ambitious heavy ion programs. In BNL the emphasis was on the acceleration of gold ions up to 9 GeV/u. In CERN the so-called lead program was initiated. The intensity of the accelerated in SPS up to 17.7 GeV/u fully stripped lead ions reached  $4.7 \cdot 10^9$  ions/pulse.

Two synchrotrons specially built for heavy ion acceleration took the baton – SIS-18 at GSI and Nuclotron at JINR. SIS-18 accelerates all ion species up to  $U^{73+}$  to a maximum energy of 1 GeV/u and with beam intensity as high as  $4 \cdot 10^{10}$  ions/pulse. Nuclotron is a superconducting machine capable to accelerate ions with  $Z_{pr}/A_{pr} = 0.5$  up to 6 GeV/u, where  $Z_{pr}$  and  $A_{pr}$  are the projectile ion atomic and mass numbers.

The story of investigations with relativistic heavy ion beams turned over a new leaf with the commissioning of the heavy ion collider RHIC at BNL. Collisions of gold nuclei at maximum energy 2x100 GeV/u with a peak luminosity  $L = 1.5 \cdot 10^{27} \text{ cm}^{-2} \cdot \text{s}^{-1}$  were realized.

Two new accelerator complexes that will accelerate heavy ions are now under construction at GSI and JINR.

The Facility for Antiprotons and Ion Research or FAIR at GSI foresees building of two new superconducting synchrotrons: SIS-100 and SIS-300 and of several storage and cooler rings. FAIR will accelerate intense proton beams up to 29 GeV and ion beams with all ion species, including uranium, up to 34 GeV/u. The secondary beams will consist of rare isotopes and of low and high energy antiprotons.

The Nuclotron-based Ion Collider Facility or NICA at JINR will provide for ion-ion ( $\text{Au}^{79+}$ ) or ion-proton collisions in the energy range of 1-4.5 GeV/u, polarized proton-proton collisions in the energy range of 5-12.6 GeV and polarized deuteron-deuteron collisions in the energy range of 2-5.8 GeV/u. The collider luminosity will be  $6.7 \cdot 10^{27} \text{ cm}^{-2} \cdot \text{s}^{-1}$ .

Principles applied for acceleration of heavy ions are the same as those applied for acceleration of protons. The breakthroughs in acceleration of ions are related mainly with the

II.2.5. Combined Longitudinal and Transverse Multiturn Injection	67
II.2.6. Ion Accumulation by Stacking with Electron Cooling	68
II.2.7. Barrier Bucket Accumulation	70
II.3. Extraction	74
II.3.1. Fast Extraction	74
II.3.2. Resonant Extraction	75
II.3.3. Stochastic Resonant Extraction	82
II.3.4. RF Knock-Out Extraction	83
II.3.5. Extraction by Betatron Core	84
II.4. RF system	85
II.4.1. Ferrite Cavities	86
II.4.2. Magnetic alloy (MA) Cavities	87
II.4.3. Storage RF System	89
II.4.4. Double RF System	90
II.4.5. Transition Crossing	91
II.4.6. Superconducting Cavities	92
II.5. Ion Colliders	93
II.5.1. Luminosity	94
II.5.2. Beam-Beam Interaction	98
II.5.3. Luminosity Lifetime	100
References	102

## INTRODUCTION

Historically the investigations with accelerated beams of heavy ions began with nuclear structure studies and with synthesis of new transuranium elements. For these experiments one needs ion energies, which lie slightly above the Coulomb barrier. Tandems, linear ion accelerators and cyclotrons were used at the early times of research with heavy ion beams. Very soon the scientific interest broadened toward more deep and sophisticated experimental studies in the fields of atomic and nuclear physics and applications in cancer therapy.

When the available ion energy surpassed the 1 GeV/u threshold studies of the nuclear equation of states and search for very hot and dense nuclear matter and for phase transitions began.

The acceleration of heavy ions to high energies, i.e. to more than 1 GeV/u, is done by synchrotrons. For energies above about 10 GeV/u the fixed target mode becomes inefficient and colliding of heavy ion beams must be used.

The first synchrotrons accelerating ions, Synchrophasotron at JINR, Bevatron at LBNL and Saturn-II at Saclay, were proton machines converted to ion synchrotrons. The first two machines were weak focusing accelerators. The upgrade included improvement of the vacuum and building of new injectors but in spite of these measures only bare nuclei could be accelerated due to the poor vacuum conditions. The maximum energies were: 1.15 GeV/u for Saturn-II, 2.1 GeV/u for Bevatron and 4.2 GeV/u for Synchrophasotron. All the three machines are already out of operation.

After the successful demonstration that heavy ions could be accelerated in proton synchrotrons the AGS at BNL and the SPS at CERN started ambitious heavy ion programs. In BNL the emphasis was on the acceleration of gold ions up to 9 GeV/u. In CERN the so-called lead program was initiated. The intensity of the accelerated in SPS up to 17.7 GeV/u fully stripped lead ions reached  $4.7 \cdot 10^9$  ions/pulse.

Two synchrotrons specially built for heavy ion acceleration took the baton - SIS-18 at GSI and Nuclotron at JINR. SIS-18 accelerates all ion species up to  $U^{73+}$  to a maximum energy of 1 GeV/u and with beam intensity as high as  $4 \cdot 10^{10}$  ions/pulse. Nuclotron is a superconducting machine capable to accelerate ions with  $Z_{pr}/A_{pr} = 0.5$  up to 6 GeV/u, where  $Z_{pr}$  and  $A_{pr}$  are the projectile ion atomic and mass numbers.

The story of investigations with relativistic heavy ion beams turned over a new leaf with the commissioning of the heavy ion collider RHIC at BNL. Collisions of gold nuclei at maximum energy  $2 \times 100$  GeV/u with a peak luminosity  $L = 1.5 \cdot 10^{27}$  cm<sup>-2</sup>·s<sup>-1</sup> were realized.

Two new accelerator complexes that will accelerate heavy ions are now under construction at GSI and JINR.

The Facility for Antiprotons and Ion Research or FAIR at GSI foresees building of two new superconducting synchrotrons: SIS-100 and SIS-300 and of several storage and cooler rings. FAIR will accelerate intense proton beams up to 29 GeV and ion beams with all ion species, including uranium, up to 34 GeV/u. The secondary beams will consist of rare isotopes and of low and high energy antiprotons.

The Nuclotron-based Ion Collider Facility or NICA at JINR will provide for ion-ion ( $Au^{79+}$ ) or ion-proton collisions in the energy range of 1-4.5 GeV/u, polarized proton-proton collisions in the energy range of 5-12.6 GeV and polarized deuteron-deuteron collisions in the energy range of 2-5.8 GeV/u. The collider luminosity will be  $6.7 \times 10^{27}$  cm<sup>-2</sup>·s<sup>-1</sup>.

Principles applied for acceleration of heavy ions are the same as those applied for acceleration of protons. The breakthroughs in acceleration of ions are related mainly with the

invention of the EBIS and ECRIS sources of intense beams of high charge states heavy ions, with the discovery of RFQ accelerator, with the progress made in the high current linear injectors and with the introducing of electron cooling technics.

The remaining bound electrons in the multi-electron ions and the high electric charge of the fully stripped (bare) nuclei are the two major factors in which the acceleration of ions differs from the acceleration of protons.

The multi-charged ions interact with the molecules and atoms of the residual gas in the vacuum chamber of the accelerator and/or with deliberately set stripping targets. This interactions lead to loss or capture of electrons from/to the projectile electron shell and hence to a jump of the projectile charge to mass ratio. The ion cannot be further guided and focused by the accelerator magnetic system in a proper way and is lost.

On the other hand ion loss can produce vacuum pressure instability and pressure bumps, which in turn lead to more beam losses. A positive feedback could be established and the beam could be completely destroyed.

The high electric charge  $eZ_{pr}$  of the fully stripped nuclei compared with the proton charge has many positive and negative consequences. Here are some.

- As the particle charge grow up the influence of the adverse space charge effects also increases. The coherent space charge tune shift  $\Delta Q$  is proportional to  $Z_{pr}^2 / A_{pr}$ . High space charge tune shift ( $\Delta Q > 0.25$ ) results in resonance crossing and beam loss. The intensity limitations are most severe in the booster synchrotron due to the low ion velocity at injection. The cure is to have a large acceptance of the accelerator and to fill this acceptance with particles as densely as possible. Methods for multiturn injection with stacking in all the three-horizontal, vertical and longitudinal phase spaces have been developed. For a small machine like a booster synchrotron the use of large acceptance is cost-reasonable.
- The beam rigidity  $B\rho$  is inversely proportional to the ion charge. Increasing the ion charge you reduce the power necessary for acceleration to a given kinetic energy. On the other hand the less the ion charges the higher space charge limit. Hence a compromise must be worked out.
- In heavy ion colliders the luminosity and the beam lifetimes are dominated by intrabeam scattering. The intrabeam scattering phenomenon leads to particle loss out of the RF buckets and to an increase of the transverse beam emittances. This reduces the luminosity of the collider. The intrabeam scattering effect scales as  $Z_{pr}^4 / A_{pr}^2$ .

This book is devoted to the problems of acceleration of heavy ions to relativistic energies. Both ion synchrotrons and ion colliders are considered. The emphasis falls on the physical processes that make the acceleration of heavy ions something different from the acceleration of other particles. The specific features of the main accelerator systems in the case when the accelerated particles are heavy ions are discussed in details.

## Part I. BASIC PRINCIPLES AND PHYSICAL PROCESSES

### I.1. VARIANTS OF A HIGH ENERGY HEAVY ION ACCELERATOR COMPLEX

#### I.1.1. General Remarks

A high energy heavy ion accelerator complex consists of ion source and of several accelerators, connected by beam transfer lines.

It was already pointed out that when accelerated ions are in high charge state the energy gain per turn and the final energy of the accelerator are higher. The accelerator becomes more compact and sufficiently cheaper.

In view of the interaction with the residual gas and related beam losses it is preferable to accelerate bare nuclei than ions in intermediate charge state. However it is very difficult to produce intense beams of fully stripped heavy ions by the existing ion sources.

That is why in a high energy heavy ion accelerator complex the ions are stepwise ionized while they move along the chain of accelerators. To do this we let ions to pass through gaseous targets or thin solid foils. The process is known as ion stripping.

It is the ion source that lies at the root of the accelerator complex. That is why we will start with a short review of the sources of heavy ions.

#### I.1.2. Sources of Heavy Ions

One of the main factors that determine the structure of a high energy heavy ion accelerator complex is the choice of the ion source. The heavy ion sources that are nowadays in operation are listed in Table 1.

Table 1. Sources of uranium ions

Ion source	Charge state of delivered uranium ions, $i$	Beam current, emA	Pulse length, $\mu$ s
MEVVA – GSI	4	15	500
VENUS – LBNL	30	0.240	dc
EBIS – BNL	30	2.4	10
ESIS – JINR	90	7.2	10

• **Vacuum Arc Ion Sources.** These are sources of ions in low charge state,  $i$ , but with high ion beam intensity. The ion intensity can reach up to  $0.25A_{pr}/i$  in emA,  $A_{pr}$  being the projectile mass number. Vacuum arc ion sources are widely used in the GSI heavy ion accelerator complex. The achieved in GSI beam currents lie above the space charge limit of the injector RFQ section. Vacuum arc ion sources are relatively simple. They need neither gyrotron amplifiers nor superconducting magnets. The pulse length is long enough, 500  $\mu$ s or more, which allows for a kind of multiturn injection into synchrotron to be realized.

In GSI the multi casp ion source MUCIS is used for gaseous ions (deuterium, helium, argon, xenon etc.) – [1]. For example  $Ar^{1+}$  beams with 38 emA current were produced.

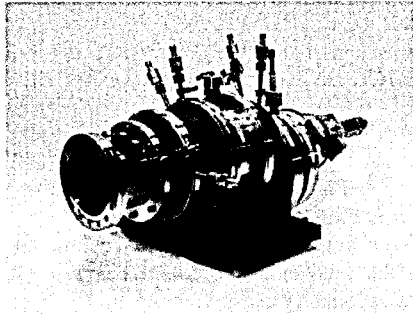


Fig. 1. Metal Vapor Vacuum Arc ion source MEVVA at GSI, Darmstadt – [2]

For metal ions the Metal Vapor Vacuum Arc ion source MEVVA – Fig. 1 has been developed – [2]. It provides uranium beams with typical total current of 24 e mA and the fraction  $U^{4+}$  reaching a rate of 67%. The new modification of MEVVA ion source, named VARIS, can generate even more intensive uranium beams. With arc current 700 A at 30 kW and a careful tuning of the extraction system the analyzed  $U^{4+}$  current has reached 25 e mA.

• **Electron Cyclotron Resonance Ion Source, ECRIS.** ECRIS was suggested by R. Geller. It is able to generate high current, medium charge state beams. The ion source operates at dc or long pulses ( $\sim 200 \mu s$ ) modes. The latter mode is called “afterglow” mode and deliver larger intensity. The ion sources of ECRIS type are very reliable and stable in operation. The recent improvements are related with raising the RF frequency and the strength of the magnetic field applying a gyrotron amplifier and superconducting solenoidal and hexapole radial cusp magnetic fields.

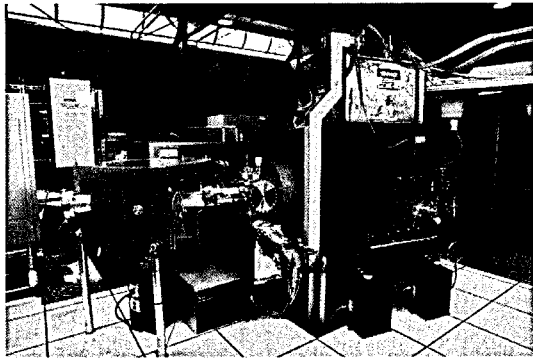


Fig. 2. ECRIS VENUS at LBNL, Berkeley– [3]

The developed in LBNL superconducting ECRIS VENUS utilizes a commercially available 10 kW – CW, 28 GHz gyrotron amplifier and has a peak magnetic field of 4 T – [3]. It can produce 240 e  $\mu A$   $U^{30+}$  or 5 e  $\mu A$   $U^{48+}$  beams.

• **Electron Beam Ion Source, EBIS.** EBIS produces ion beams in highest available charge states. The ion source was developed at JINR by E.D. Donets. For EBIS the total

extracted charge per pulse is independent of the ion species and of the ion charge state. The charge state distribution is narrow. Typically the desired charge state rate is about 20% of the total current. EBIS produces short pulses of high current and is well suited for single turn injection into synchrotrons but not for multirun injection.

The recent advantages made in BNL have used an electron gun with 10 A electron beam current and a 0.7 m long trap – [4]. A beam of  $Au^{32+}$  ions with 550 e  $\mu A$  in 15  $\mu s$  pulses has been produced. BNL EBIS could also deliver beams of  $U^{30+}$  ions with intensity  $5 \cdot 10^9$  ions in 10  $\mu s$  pulses. The time between the successive pulses is 100 ms. This source uses a 5 T superconducting solenoid.

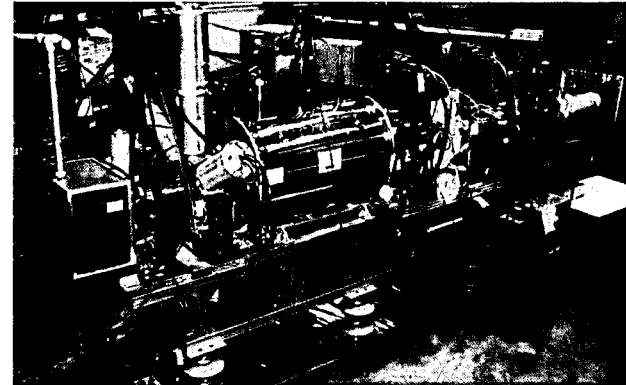


Fig. 3. Test EBIS at BNL, Brookhaven – [4]

By using of electron reflectors E.D. Donets in JINR succeeded in formation of electron strings with high linear electron space charge density, which could be used for effective production of highly charged ion beams. He called this modification of EBIS – Electron String Ion Source, ESIS – [5]. In the first tests with JINR “Krypton-2”, converted to ESIS type ion source,  $Ar^{16+}$  beams with current up to 150 e  $\mu A$  in 8  $\mu s$  pulses have been produced. The ESIS ion source could produce beams of  $Au^{31+}$  and  $Au^{49+}$  with an intensity of  $2 \cdot 10^9$  ions in 7  $\mu s$  pulses with repetition rate up to 50 Hz.

• **Laser Ion Source, LIS.** Laser ion source is also worth mentioning. It delivers short (few  $\mu s$ ) intense ion pulses and could be used for single turn injection into synchrotrons. A  $CO_2$  laser is usually applied. Recently a collaboration between ITEP and TRINITI from Russia and CERN succeeded in generating of  $Pb^{27+}$  ion beams with total extracted current of 20 e mA, a pulse width of several  $\mu s$  and repetition rate 1 Hz. A 100 J, 15  $\text{\AA}$ , 30 ns  $CO_2$  laser was used in this LIS.

To sum up – from the point of view of injection and acceleration in synchrotrons we could distinguish three groups of ion sources (Fig. 4):

- Sources of single charged ions or of ions in very low charge state, but with highest intensity, which is reached by now;
- Sources of medium charged ions with medium beam current;
- Sources for ions in highest charge states, which are reached by now, but with lower beam current.

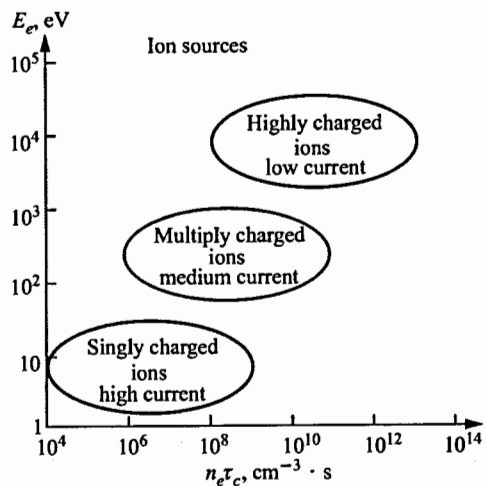


Fig. 4. Different types of ion sources. On the horizontal axis the product of electron density and confinement time is shown on the vertical axis the electron energy is shown

Three main approaches to the acceleration of heavy ions to high energies could be distinguished.

### 1.1.3. Variant of the High Energy Heavy Ion Accelerator Complex with a High Current, Low Charge State Injector

The basic idea is the use of an intensive source of ions in low charge state – Fig. 5. Acceleration of low charged ions by linear accelerators require high accelerating voltage and as the voltage gain is limited (4.2 MV/m in the GSI IH-DTL) the length of the linac becomes large. The linear injector must be split to two parts with a stripping section between them. In this way you increase the ion charge state at as low energy as this is possible. Large particle loss due to the bad stripping efficiency at low projectile energy is the price you must pay.

As the pulse length of the used ion sources is large (500 – 1000  $\mu$ s) a multiturn injection into the booster synchrotron with big number of injected turns could be realized.

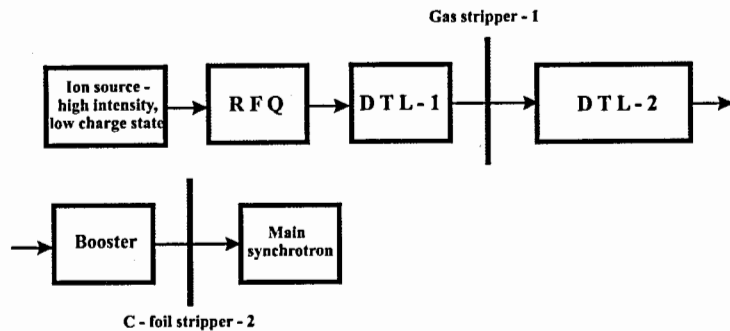


Fig. 5. Variant with a high current, low charge state injector

This approach to the high-energy heavy-ion acceleration has been developed for many years in GSI – [6,7] – Fig. 6. A multicasp ion source for gaseous ions and a metal vapor vacuum arc ion source for metal ions are used. These sources deliver intensive beams of low charged ions.

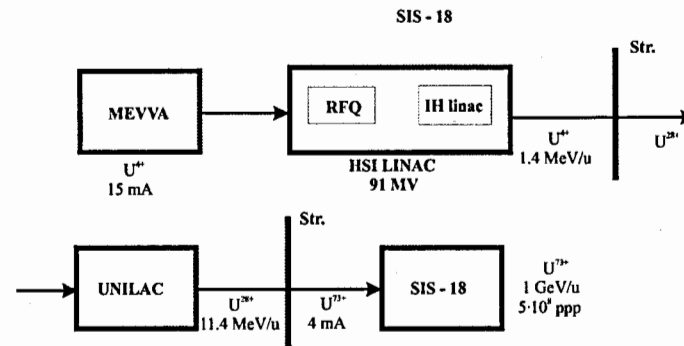


Fig. 6. Acceleration of uranium ions in SIS-18 synchrotron at GSI, Darmstadt

The first section of the GSI high current linear injector is a 36 MHz, 9.4 m long, RFQ structure, working in  $H_{110}$  mode – [8]. This first section accelerates the ions up to 120 keV/u. It is followed by a 20 m long IH drift tube linac. This IH-DTL further accelerates ions to 1.4 MeV/u, an energy that is high enough for a  $N_2$  – jet stripper to be applied. The gas stripper raises the ion charge state from  $U^{4+}$  to  $U^{28+}$ . Energy 1.4 MeV/u is too low energy and the stripping efficiency is only 12%. This is compensated by the high intensity of the source (15 emA for  $U^{4+}$ ).

The famous UNILAC then takes the baton. It pushes ions up to 11.4 MeV/u. At this energy a C – foil stripper can be applied. This second stripper raises the ion charge from  $U^{28+}$  to  $U^{73+}$ . The reported stripping efficiency is 15%. Energy of 11.4 MeV/u is high enough to guarantee small residual gas losses in the SIS-18 synchrotron.



Fig. 7. The synchrotron SIS-18 at GSI, Darmstadt

At present at GSI a new accelerator facility which will provide experiments with high energy and high intensity proton and heavy ion beams is under construction. The new facility is named FAIR – [9-10], which is abbreviation from Facility for Antiproton and Ion Research. FAIR consists of two separate superconducting synchrotrons SIS-100 and SIS-300 with equal circumferences and placed on top of each other plus a number of storage rings – Fig.8. The existing accelerator complex SIS-18 will serve as injector for FAIR accelerators.

Main parameters of FAIR are listed in Table 2.

The superconducting synchrotron SIS-100 will accelerate heavy ions ( $U^{28+}$  for example) up to 2.7 GeV/u with intensity of  $1 \cdot 10^{12}$  ions per pulse. These beams will be used for the production of secondary beams of radioactive ions. SIS-100 will accelerate also protons up to 29 GeV with an intensity of  $2.8 \cdot 10^{13}$  protons per second. These protons will be used for the production of intense antiproton beams. In SIS-100 superferic superconducting magnets with maximum field 2T and ramp rate 4 T/s will be used. SIS-300 will be applied for the acceleration of fully ionized  $U^{92+}$  ions up to 34 GeV/u. In SIS-300 superconducting magnets with two-layer  $\cos\theta$  coils will be used. The maximum field of these magnets will be 6T and the ramp rate 1 T/s. The circumferences of both machines are  $C = 2\pi \cdot 50$  m, so the beam rigidity in SIS-100 is  $B\rho = 100T \cdot m$  and in SIS-300 it is  $B\rho = 300T \cdot m$ . The upgraded synchrotron SIS-18 will serve as a fast booster for SIS-100. In booster mode SIS-18 will work with dipole ramp rate of 10 T/s. This means a repetition rate of 2.7 Hz for heavy ions and of 4 Hz for protons.

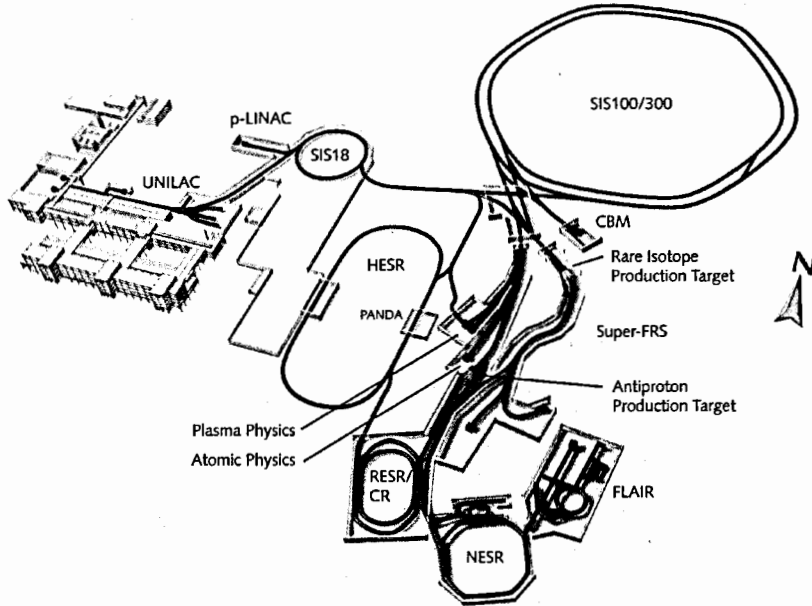


Fig. 8. FAIR at GSI, Darnstadt – [10]

Table 2. Main parameter of FAIR synchrotrons and storage rings – [10]

Ring	Circumference [m]	Beam rigidity [T·m]	Beam Energy [GeV/u]	Specific Features
Synchrotron SIS100	1083.6	100	2.7 for $U^{28+}$ 29 for protons	Fast pulsed superferic magnets up to 2 T, 4 T/s, bunch compression to $\sim 60$ ns of $5 \cdot 10^{11}$ U ions, fast and slow extraction, $5 \cdot 10^{-12}$ mbar operating vacuum
Synchrotron SIS300	1083.6	300	34 GeV/u $U^{92+}$	Pulsed superconducting cos $\theta$ -magnets up to 6 T, 1 T/s, slow extraction of $\sim 3 \cdot 10^{11}$ U-ions per sec. with high duty cycle, $5 \cdot 10^{-12}$ mbar operating vacuum
Collector Ring CR	212	13	0.740 for $A/q=2.7$ 3 for antiprotons	Acceptance for antiprotons: $240 \times 240$ mm mrad, $\Delta p/p = \pm 3 \cdot 10^{-2}$ , fast stochastic cooling of radioactive ions and antiprotons, isochronous mass spectrometer for short-lived nuclei
Accumulator Ring RESR	245	13	0.740 for $A/q=2.7$ 3 for antiprotons	Accumulation of antiprotons after pre-cooling in the CR, fast deceleration of short-lived nuclei, ramp rate 1 T/s
New Experimental Storage Ring NESR	222	13	0.740 for $A/q=2.7$ 3 for antiprotons	Electron cooling of radioactive ions and antiprotons with up to 450 keV electron-beam energy, precision mass spectrometer, internal target experiments with atoms and electrons, electron-nucleus scattering facility, deceleration of ions and antiprotons, ramp rate 1 T/s
High-Energy Storage Ring HESR	574	50	14	Stochastic cooling of antiprotons up to 14 GeV, electron cooling of antiprotons up to 9 GeV; internal gas jet or pellet target

The current variant of the BNL-RHIC heavy-ion collider – [11-13] could be attributed to this approach as well – Fig. 9.

At the root of the ion path is a sputter source of  $Au^{-1}$  ions. These ions are pre-accelerated by a tandem Van de Graaff accelerator to 1 MeV/u. The beam pulse consists of  $5.4 \cdot 10^9$  ions and is 530 ms long. Then ions are stripped to  $Au^{32+}$  and injected into the AGS circular injector-booster. In AGS booster a sophisticated multiturn injection with staking the particles in both horizontal and vertical phase planes via coupling of betatron oscillations is used. This allows injecting 40 turns with 65% efficiency. The efficient painting of horizontal and vertical phase planes is possible because of the very small emittance ( $1\pi$  mm·mrad) of the tandem beam. Due to the X-Y coupling the stored intensity is increased by a factor 50%.

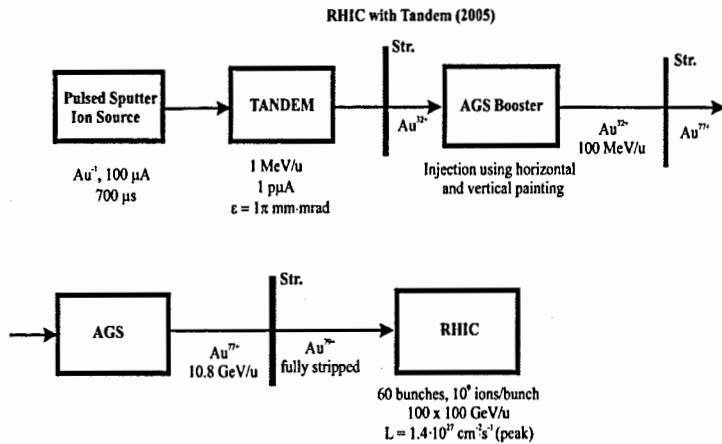


Fig. 9. Acceleration of gold ions in the BNL accelerator complex at Brookhaven

In the booster the  $Au^{32+}$  ions are accelerated to 100 MeV/u, extracted and stripped for a second time to  $Au^{77+}$ . As the circumference of the booster is  $1/4$  of this of the AGS synchrotron, four booster cycles are successively injected in AGS.

In AGS synchrotron the  $Au^{77+}$  ions are pushed up to the RHIC injection energy of 8.6 GeV/u. The intensity of the ion beam after AGS is  $1.1 \times 10^9$  ions/bunch. The energy 8.6 GeV/u is high enough for efficient stripping to bare,  $Au^{79+}$ , ions which is necessary for long-time (typically 10 h) storing in the two collider rings.

Relativistic Heavy Ion Collider or RHIC consists of two independent superconducting rings labeled blue and yellow rings – Fig. 10. RHIC can collide fully stripped gold-gold and copper-copper beams accelerated up to 100 GeV/u, deuteron-gold beams and high intense polarized proton-proton beams, accelerated to 100 GeV.

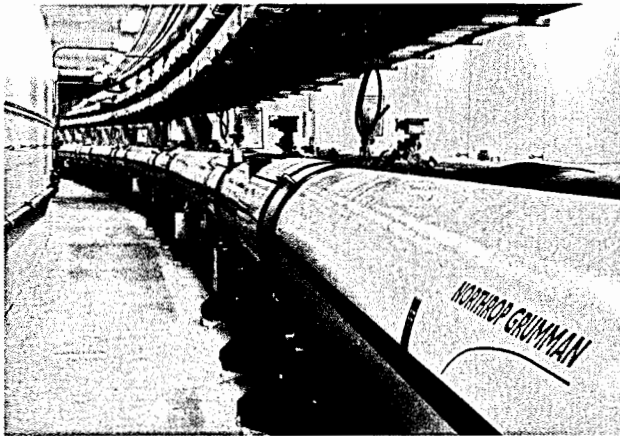


Fig. 10. Relativistic Heavy Ion Collider (RHIC) at BNL, Brookhaven

The two collider rings intersect in six interaction points (IP). The value of the amplitude  $\beta$ -function at IPs is  $\beta^* = 10$  m at injection and  $\beta^* = 1$  m in collision mode. The two rings are filled with 56 AGS bunches. The peak luminosity is  $L = 1.0 \times 10^{27} \text{ cm}^{-2} \cdot \text{s}^{-1}$  while the luminosity averaged over 10h storage time is  $2.0 \times 10^{26} \text{ cm}^{-2} \cdot \text{s}^{-1}$ . As the total  $Au-Au$  cross-section is high the interaction rate for this luminosity is comparable to those for  $p-p$  collisions.

#### 1.1.4. Variant of the High Energy Heavy Ion Accelerator Complex with Injector of Heavy Ions in Medium Charge State, working in dc Mode

The only source of multi-charged ions working in dc mode at the moment is Electron Cyclotron Resonance Ion Source or ECRIS – [14]. The beam current of the state-of-art ion sources of this type is 200 – 400 eμA, depending on the ion species, and could be doubled in the pulse (afterglow) mode with 200 – 300 μs pulses. The much higher charge states of the ions delivered by ECRIS compared with those from vacuum arc ion source allow to drop out the first stripper in Fig. 6 and thus to increase the efficiency almost ten times – Fig. 11.

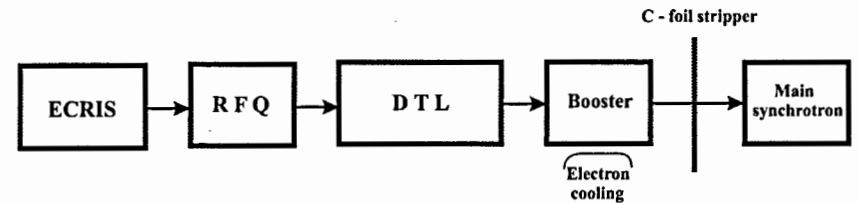


Fig. 11. Variant with source of heavy ions in medium charge states, working in dc mode

On the other hand the dc nature of ECRIS allows applying efficient multiturn injection into the booster synchrotron.

This approach to heavy ion acceleration is realized in the LHC lead acceleration chain – [15,16] – Fig.12. CERN's ECRIS works at 14.5 GHz in afterglow mode and produces beams of  $Pb^{27+}$  ions with 200 eμA beam current.

The CERN Pb program uses "Linac-3" as a linear injector. It pushes the energy of  $Pb^{27+}$  ions up to 4.2 MeV/u. After that the first stripper increases the ion charge to  $Pb^{54+}$ . A key role in the lead accelerator chain plays LEIR which serves as an accumulator ring increasing the beam intensity by means of a sophisticated combined multiturn injection. The injection in LEIR covers 35 turns, with 25 effective ones. It takes place in both transverse and longitudinal phase spaces. This original method increases the stored intensity 3 to 5 times and simultaneously reduces the transverse emittance 3 times. After the multiturn injection is fulfilled the stored beam is cooled down applying the electron cooling method. The cooling time is short – 0.1s. The fast electron cooling reduces the phase space volume of the beam and allows for high brightness bunches to be built by repeating of four stacking – cooling cycles. The ions in LEIR are adiabatically captured in two bunches and accelerated up to 72 MeV/u. The CPS synchrotron follows in the chain. The ions are injected into CPS by means of two pulsed bump magnets, a kicker magnet and a pulsed septum. The two LEIR bunches fill  $1/8$  of the CPS circumference. From these two bunches new four bunches with bunch spacing of 125 ns, which is necessary for LHC operation, are built by change of the RF harmonic number and bunch splitting. CPS accelerates ions up to 5.9 GeV/u. This energy is sufficient for effective stripping of  $Pb^{54+}$  ions to bare lead nuclei,  $Pb^{82+}$ , by 9.8 mm Al foil. Thirteen CPS bunches are injected into SPS synchrotron and accelerated up to 177 GeV/u.

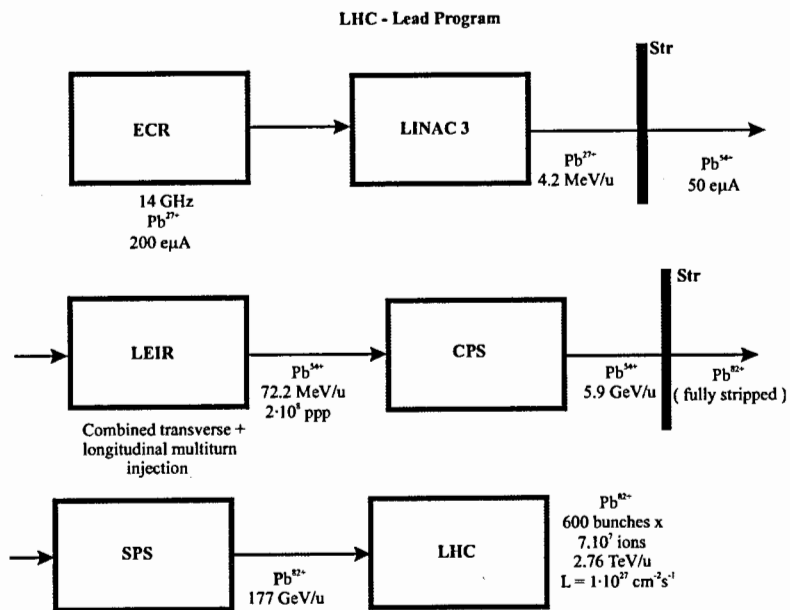


Fig. 12. LHC lead ion program at CERN

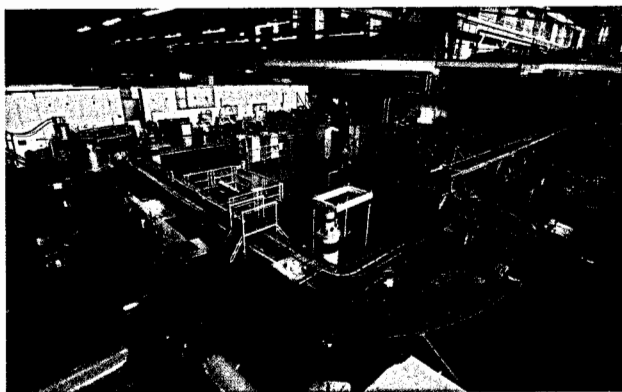


Fig. 13. Low Energy Ion Ring (LEIR) at CERN

The LHC lead ion program envisages in the so-called “nominal ion scheme” realizing of lead-lead collisions at 2.76 TeV/u with peak luminosity  $L = 1 \cdot 10^{27} \text{ cm}^{-2} \cdot \text{s}^{-1}$ . The two collider rings will be filled during 10 minutes with up to 592 bunches. Each bunch will contain  $7 \cdot 10^7$  fully stripped  $\text{Pb}^{82+}$  ions. In the “early ion scheme” the number of bunches is reduced 10 times,  $\beta^* = 1 \text{ m}$ , but the number of particles per bunch is the same.

### 1.1.5. Variant of the High Energy Heavy Ion Accelerator Complex with Injector of Heavy Ions in High Charge States, working in a Short Pulses Mode

The ion source that delivers heavy ions in the highest at the moment charge states is Electron Beam Ion Source or EBIS. EBIS is able to produce highly charged ions of any species. It has the smallest beam emittance.

With ions in high charge states the RFQ and DTL sections of the injector are more compact and efficient.

EBIS is a pulsed ion source. The pulses of extracted ions are short, typically about  $10 \mu\text{s}$ . The pulse length is of the order of the booster revolution time and the single turn injection is the natural choice. The repetition rate of EBIS is 1 – 5 Hz. In principle one could repeat the single turn injection several times stacking the particles in the momentum space.

The accelerator chain is schematically shown on Fig. 14.

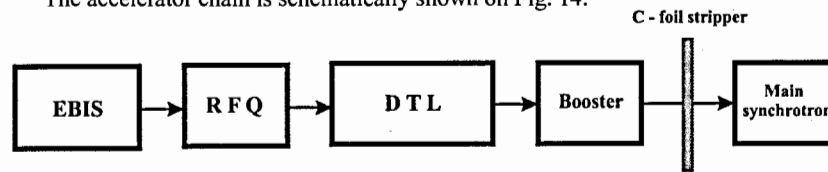


Fig. 14. Variant with injector of heavy ions in high charge states, working in a short pulses mode

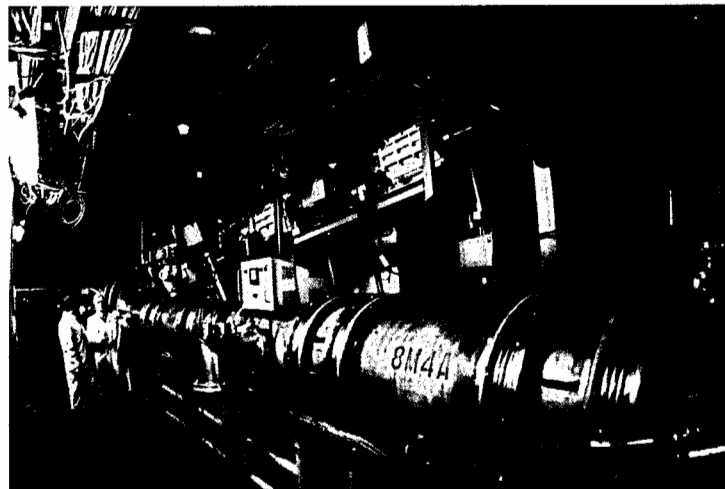


Fig. 15. The superconducting heavy ion synchrotron Nuclotron at JINR, Dubna

This approach has been applied to the JINR Synchrophasotron and after its shutdown to the Synchrophasotron's successor – the superconducting heavy ion synchrotron Nuclotron – [17] – Fig. 15. The developed by E.D. Donets EBIS “Krypton-2” can produce for example  $8 \mu\text{s}$  pulses of  $\text{Ar}^{16+}$  and  $\text{Fe}^{24+}$  ions with beam currents of 200  $\mu\text{A}$  and 150  $\mu\text{A}$  respectively. The repetition rate is 1 Hz.

Nuclotron is a synchrotron dedicated to acceleration of heavy ions that uses the developed at JINR superferromagnetic magnets the magnetic field is

Научно-техническая  
библиотека  
ОИЯИ

formed by an iron yoke while the coils are made of hollow superconducting NbTi cable. The cable is cooled with two-phase helium at 4.5K. The superferric magnets are fast-pulsed (field ramp up to 4 T/s) with maximum inductance of 2 T. The Nuclotron ring has a circumference of 251.5 m and a maximum magnetic rigidity of 45 T·m. It can accelerate protons up to 12.6 GeV and heavy ions up to 4.6 GeV/u.

On the base of Nuclotron a new heavy ion collider is under construction at the Joint Institute for Nuclear Research in Dubna – [18]. The new accelerator complex is named Nuclotron-based Ion Collider Facility or NICA. The main goal of NICA is the investigation of the nuclear matter at extreme conditions of very high temperatures and densities and search for the so-called mixed phase of the strongly interacting matter.

The accelerator complex NICA will include: new 6.2 MeV/u linac, a superconducting booster with maximum magnetic rigidity of 25 T·m and electron cooling, the upgraded superconducting synchrotron Nuclotron and two superconducting colliding rings with maximum magnetic rigidity of 45 T·m and systems for electron and stochastic cooling – Fig. 16. NICA will accelerate for example intense  $(1.7 \cdot 10^{10})_{197}Au^{79+}$  ion beams with energies between 1.0 GeV/u and 4.5 GeV/u. The collider will have two interaction points in which the so-called Multi Purpose Detector (MPD) and Spin Physics Detector (SPD) will be installed. The luminosity is expected to be  $6.7 \times 10^{27} \text{ cm}^{-2} \cdot \text{s}^{-1}$ .

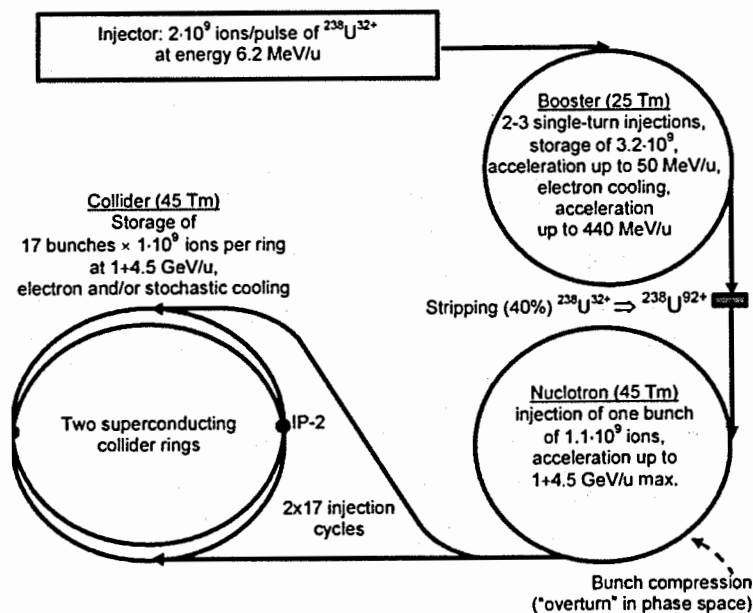


Fig. 16. Nuclotron-based Ion Collider Facility (NICA) at JINR, Dubna

An important step toward higher beam intensity was made recently in BNL. Increasing the electron current in a test EBIS up to 10 A and improving the ion confinement the BNL team succeeded in producing  $Au^{35+}$  beams with  $3 \cdot 10^9$  ions/pulse. This success encouraged the BNL specialists and they have proposed to replace the Tandem injector with a combination of EBIS, RFQ and short linac – [19] – Fig. 17.

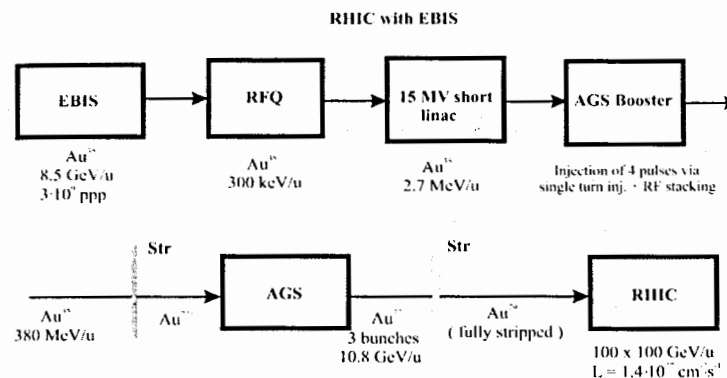


Fig. 17. RHC with EBIS (project)

Meanwhile E. D. Donets developed at JINR a source of heavy ions of new type – the Electron String Ion Source or ESIS – [20]. The hopes are that with a 12 T superconducting solenoid this source will be able to produce beams of ions with mass number A from 130 to 238, in high charge state ( $Z/A$  from 0.42 to 0.38), and with high intensity ( $1 \cdot 10^{10} - 5 \cdot 10^9$  ions/pulse). ESIS will be used in the heavy ion collider NICA.

## 1.2. PHYSICAL PROCESSES TYPICAL FOR HEAVY ION ACCELERATORS

### 1.2.1. Interaction with Residual Gas and Stripping Foils

When the ion beam moves in the accelerator the multielectron ions interact with atoms and molecules of the residual gas or with those in solid or gaseous targets, deliberately introduced in their path. These interactions include elastic and inelastic processes: single and multiple Coulomb scattering, processes of electron loss and capture and processes of excitation and ionization of target atoms and molecules. The loss or capture of electrons by fast moving ions results in the change of ion charge and hence leads to beam loss. The multiple Coulomb scattering has as a consequence an increase of transverse emittance. Spending of ion kinetic energy for excitation and ionization of target atoms increases the relative momentum spread.

In this chapter a brief description of all these processes is given.

#### 1.2.1.1. Electron Loss

This is a process of loss of electrons in ion-atomic collisions – Fig. 18. The figure of merit is the so-called atomic velocity  $v_0 = e^2/\hbar \cdot ac = 2.19 \cdot 10^6 \text{ m/s}$ , where  $a=1/137$  is the fine structure constant. In fact  $v_0$  is the velocity of an electron in the first Bohr's orbit.

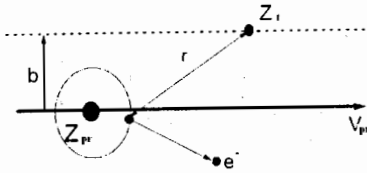


Fig. 18. Process of single electron loss in ion-atomic collisions

According to Bohr's criterion when an ion penetrates through matter it retains only those electrons whose orbital velocity  $u$  is greater than the ion velocity  $v = \beta c$ . For hydrogen-like particles with charge of the nuclei  $eZ_{pr}$ , the mean electron orbital velocity is  $u = Z_{pr}v_0$ . For such a hydrogen-like ion the electron loss cross section has a maximum for  $v = u$ .

When the ionization is due to atoms instead of nuclei the screening of the nuclear charge by the shell electrons leads to smaller ionization cross section.

Let  $\sigma_{i,i+1}$  be the cross section for loss of single electron by a multielectron ion being in charge state  $i$ .

The classical Bohr's formula - [21] predicts:

$$\sigma_{i,i+1} = 4\pi a_0^2 \frac{Z_i^2 + Z_{pr}^2}{Z_{pr}^2} \left(\frac{v_0}{v}\right)^2, \quad (1)$$

where:  $Z_{pr}$  is ion atomic number,  $Z_i$  - target atomic number,  $v_0$  - atomic velocity unit,  $a_0 = \hbar^2 / m_e c^2 = 0.529 \cdot 10^{-10} \text{ m}$  - radius of the first Bohr electron orbit.

This formula is valid for projectile kinetic energy per atomic mass unit  $T_n$ , which satisfies the condition:

$$T_n > 0.05 Z_{pr}^2, \text{ MeV/u} \quad (2)$$

and for  $Z_i$  not much larger than  $Z_{pr}$ . For uranium ions the condition (2) reads:  $T_n > 420 \text{ MeV/u}$ .

V.S. Nikolaev et al. - [22] have introduced the following correction factor to the Bohr's formula:

$$\left[ D - \left( \frac{Z_{pr} v_0}{2v} \right)^2 \right], \quad (3)$$

where:

$$D = \frac{z_{pr}^2}{2z_i^2} \text{ for } \frac{z_{pr}}{z_i} < \frac{3}{4},$$

$$D = \frac{3z_{pr}}{8z_i} \text{ for } \frac{3}{4} \leq \frac{z_{pr}}{z_i} < 4, \quad (4)$$

$$D = 1 + 0.56 \ln \left\{ \min \left[ \left( \frac{1.6v}{z_{pr} v_0} \right), \left( \frac{z_{pr}}{2z_i} \right) \right] \right\} \text{ for } \frac{z_{pr}}{z_i} > 4.$$

This formula is valid for  $T_n > 0.1 Z_{pr}^2, \text{ MeV/u}$  for particles with  $Z_{pr} < Z_i / \sqrt{2}$  and for  $T_n > 0.2 Z_{pr}^2, \text{ MeV/u}$  for ions with  $Z_{pr} > Z_i / \sqrt{2}$ .

There is no satisfactory quantitative theoretical description of the electron loss and capture cross sections. These cross sections depend sharply on the projectile velocity and as well on the atomic numbers of the projectile and target atoms and on ion charge state  $i$ .

Also there is lack of sufficient amount of experimental data on ionization cross sections for high energy highly charged states heavy ions.

Most reliable approach to estimate the cross sections is the direct measurement. However it is difficult to measure cross sections before the accelerator is built because you need ion species at the specified energy range. The available data are for the energies reached in heavy ion cyclotrons and in GSI and BNL accelerator complexes.

Analyzing the experimental data B. Franzke has proposed a semiempirical formula for the electron loss cross section by fast ions - [23], which received big popularity:

$$\sigma_{i,i+1} = 3.5 \cdot 10^{-18} e^{+i(0.7 - 0.1 Z_{pr} v_0^2)} \frac{\bar{q}_i}{\bar{q}_{pr} \gamma^2 - 1} \left( \frac{z_{pr}}{z_i} \right)^{-1}, \quad (5)$$

where  $\bar{q}_{pr}$  and  $\bar{q}_i$  are the equilibrium charge states of the projectile and target ions and  $\gamma$  and  $\beta$  - the relativistic factors. For the equilibrium charge Franzke used the formula:

$$\bar{q} = Z(1 - e^{-\frac{127\beta}{2067}}). \quad (6)$$

A comparison between the experimental data and Franzke's formula are given on Fig. 19 for 4.66 MeV/u  $\text{Pb}^{54+}$  and in Table 3 for 3.5 MeV/u and 6.5 MeV/u  $\text{U}^{28+}$  ions.

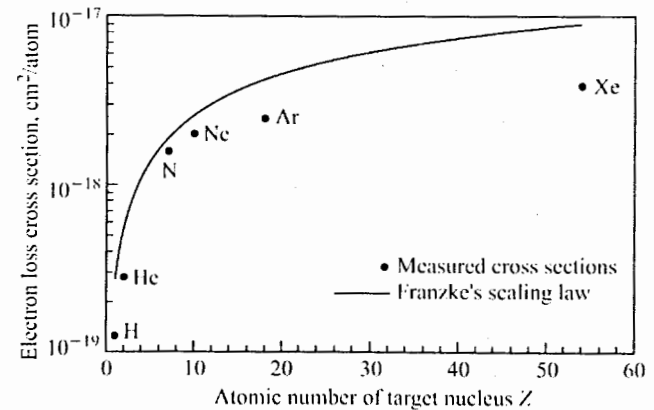


Fig. 19. Electron loss cross section for  $\text{Pb}^{54+}$  ions at 4.66 MeV/u. The dots are the experimental results and the solid line is the result obtained by the Franzke's formula - [24]

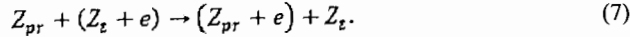
Table 3. Comparison of the experimental cross sections and Franzke's formula. The cross sections are in  $10^{-18} \text{ cm}^2/\text{atom}$  - [25]

$\text{U}^{28+}$	Target	Experiment	Franzke
3.5 MeV/u	$\text{H}_2$	1.62	4.0
	$\text{N}_2$	22.52	26.9
	Ar	45.38	58.9
6.5 MeV/u	$\text{H}_2$	1.14	0.85
	$\text{N}_2$	14.69	5.89
	Ar	33.15	13.80

### 1.2.1.2. Electron Capture

Several processes contribute to the electron capture:

**Direct Electron Capture (DEC).** DEC is relevant for fully stripped and not too heavy ions and target atoms. The process is also known as direct Coulomb capture and can be described as:



The electron capture takes place mainly for projectile velocities  $v = \beta c$  which are close to the orbital velocity of the target electron  $u$ . Due to this velocity matching the capture of K-shell target electrons into the K-shell of the projectile ion prevails. In DEC there is no photon emission. The process is important for low projectile energies. For completely stripped heavy ions in the MeV/u range the cross sections are in the order of  $10^{-27} \text{ cm}^2/\text{atom}$ .

A simple approach to describe the non-radiative electron capture cross section is the Oppenheimer-Brinkmann-Kramer or OBK theory – [26], written for hydrogen-like states. According to OBK the cross section for bound electron capture is given by:

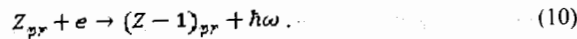
$$\sigma_{cc} = \frac{0.295 \cdot \frac{2^{19}}{5} \pi a_0^2 Z_{pr}^5 Z_t^5 \left(\frac{v}{v_0}\right)^4}{\frac{v^2}{v_0^2} + (Z_{pr} + Z_t)^2 \left[\frac{v^2}{v_0^2} + (Z_{pr} - Z_t)^2\right]^3}. \quad (8)$$

The non-radiative electron capture occurs mainly at the velocity matching condition  $v_{pr} \approx u$ ,  $u$  being the velocity of the captured electron, bound in the target atom. For  $v_{pr} \gg u$ :

$$\sigma_{NRC} \propto \frac{Z_t^5 Z_{pr}^5}{v^{11}}. \quad (9)$$

For high projectile energies electronic velocity matching becomes not probable and radiative electron capture takes place.

**Radiative Electron Capture (REC).** REC dominates at high projectile energies when the electrons bound in the target atoms can be considered as free. The excess of energy is radiated as a photon – Fig. 20 or schematically:



A theoretical estimation of the REC cross section is given by the formula, derived by Oppenheimer – [27]. Speaking qualitatively the REC cross section grows quickly with  $Z_{pr}$  and decreases rapidly with the projectile velocity:

$$\sigma_{REC} \propto \frac{Z_t Z_{pr}^3}{v_{pr}^3}. \quad (11)$$

REC cross sections for fully stripped uranium ions are in the order of  $10^{-22} \text{ cm}^2/\text{atom}$ .

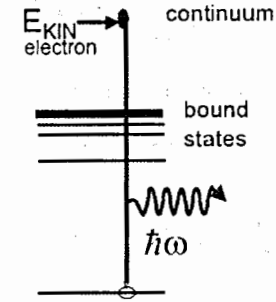


Fig. 20. Radiative Electron capture (REC)

Similar to REC is the Radiative Recombination (RR), which is the process of radiative transfer of bound electron from the target atom to the projectile.

**Dielectronic Recombination (DER).** DER is a resonant process in which the excess of energy is used to excite an electron in the projectile ion – Fig. 21. DER takes place in beams of not fully stripped ions. At resonant energies cross sections of DER can be compatible to those of REC at low velocity.

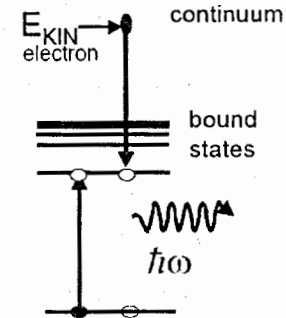


Fig. 21. Dielectronic Recombination (DER)

Between empirical formulas for single electron capture cross sections the best approximation gives the Schlachter's scaling rule – [28]. The accuracy of this empirical rule for ions from He to U and energies from 100 keV/u up to 10 MeV/u is higher than one order of magnitude. This is the reason why the Schlachter's rule has gained a big popularity. This rule is expressed by the equation:

$$\tilde{\sigma}_{cap} = \frac{1.1 \cdot 10^{-8}}{\tilde{E}^{4.8}} (1 - e^{-0.037 \tilde{E}^{2.2}}) (1 - e^{-2.44 \cdot 10^{-5} \tilde{E}^{2.6}}), \quad (12)$$

where the reduced energy  $\tilde{E}$  is given by:

$$\tilde{E} = \frac{E}{Z_t^{1.25} v_{pr}^{0.7}} \quad (13)$$

and the reduced capture cross section  $\tilde{\sigma}_{cap}$  is given by:

$$\sigma_{cap} = \frac{\sigma_{cap} Z_t^{1.8}}{\sqrt{i}}, \quad (14)$$

$i$  being the projectile charge state.

A comparison between the experimental data and Schlachter's empirical scaling rule for  $Pb^{54+}$  ions at 4.66 MeV is shown on Fig. 22.

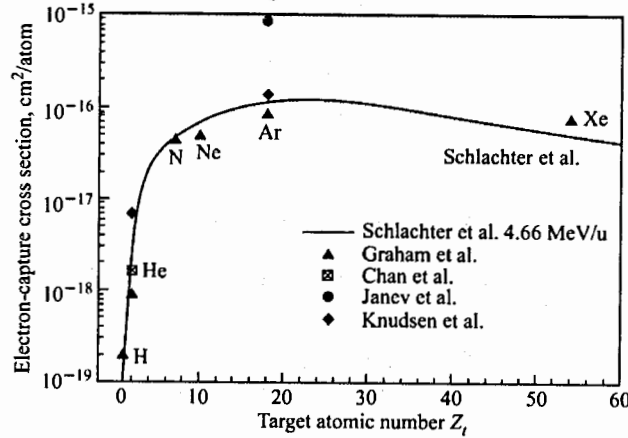


Fig. 22. Single electron capture cross section as a function of the atomic number of the target gas for 4.66 MeV  $Pb^{54+}$  ions. The solid line represents the Schlachter's empirical scaling law and the points – experimental and theoretical results – [24]

### 1.2.1.3. Interaction with the Residual Gas and Beam Lifetime

When ions collide with the residual gas atoms and molecules in the vacuum chamber of the accelerator, abrupt changes of the ion charge state lead to beam loss.

In synchrotrons the energy gain per turn  $\Delta T_{turn}$  is proportional to the ratio  $i/A_{pr}$ ,  $i$  being the projectile ion charge state and  $A_{pr}$  – the projectile mass number. The heavier ion and the lower its charge state the slower goes acceleration. Thus for  $U_{238}^{10+}$  ions (GSI)  $i/A_{pr} = 0.042$ ; for  $Au_{197}^{33+}$  ions (BNL)  $i/A_{pr} = 0.167$ ; for  $Pb_{207}^{54+}$  ions (CERN)  $i/A_{pr} = 0.26$ ; for  $U_{238}^{73+}$  ions (GSI)  $i/A_{pr} = 0.30$ , while for protons this ratio is equal to unit.

As a rule the heavy ions need much more time to reach the maximum energy of the machine.

While for protons the interaction with the residual gas consists in Coulomb scattering and in excitement and ionization of atoms for heavy ion beams the major process is the process of charge exchange.

Above 20 MeV/u the loss of electrons (stripping) prevails over the electron capture.

For synchrotrons accelerating heavy ions the injection energy is usually much lower than the injection energy in proton machines. For low energy of the ions however the cross sections for charge exchange are high. Thus for 10 MeV/u U or Pb ions the charge exchange cross section is of the order of  $10^{-16} \text{ cm}^2$ .

The standard multiturn injection with stacking in horizontal phase space takes relatively small time. For example SIS 40-turn injection of  $U_{238}^{73+}$  at 11.4 MeV/u lasts about 200  $\mu\text{s}$ . On the contrary RF stacking in longitudinal phase space takes much more time. Thus

the RF injection into TSR storage ring in Heidelberg, which covers 25 cycles, lasts about 250 ms. In the BNL-EBIS project the injection of 4 EBIS pulses in the longitudinal phase space of the AGS booster is supposed to take about 450 ms. Hence in the case of RF stacking the vacuum related beam loss will be much higher.

The beam lifetime is given by:

$$\frac{1}{\tau} = v_{pr} \sigma_{tot} n, \quad (15)$$

where  $\sigma_{tot}$  is the total charge changing cross section in  $\text{cm}^2/\text{atom}$  and  $n$  is the gas density in  $\text{atoms}/\text{cm}^3$ .

$$n = 9.656 \cdot 10^{18} \frac{p}{T}, \quad (16)$$

where  $p$  is the residual gas pressure in Torr and  $T$  – absolute temperature in Kelvin.

It follows from (15,16) that the one revolution transparency of the accelerator at 20°C is given by:

$$D = \exp(-3.293 \cdot 10^{16} p \sigma_{tot} L), \quad (17)$$

where  $L$  is the accelerator circumference in cm.

We should take into account that the total charge exchange cross section  $\sigma_{tot}$  in (17) is a function of projectile nuclear charge  $Z_{pr}$ , target (i. e. residual gas) nuclear charge  $Z_t$  and projectile velocity  $v_{pr}$  at the specified point of the accelerator cycle,  $\sigma_{tot} = \sigma_{tot}(Z_{pr}, Z_t, v_{pr})$ .

In a mixture of gases, which is the case of residual gas in accelerators, the beam lifetime and the accelerator transparency are sums of the partial beam lifetimes and transparencies:

$$\frac{1}{\tau_{tot}} = \frac{1}{\tau_{H_2}} + \frac{1}{\tau_{CO_2}} + \frac{1}{\tau_{N_2}} + \dots \quad (18)$$

$$D = D_{H_2} + D_{CO_2} + D_{N_2} + \dots$$

The lifetime of  $Pb^{53+}$  ion beam in CERN PSB is shown on Fig. 23 as a function of ion energy – [29].

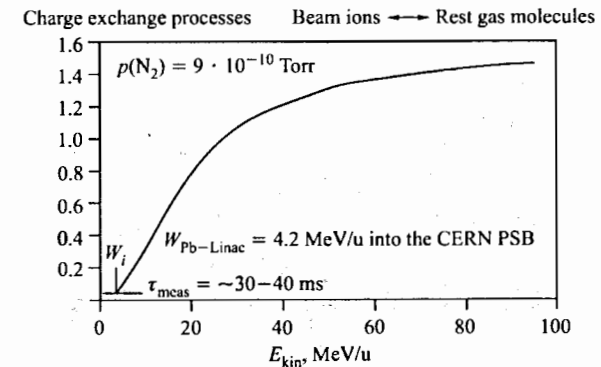


Fig. 23. Lifetime of  $Pb^{53+}$  ions in PSB – [29]

Vacuum induced beam loss has been measured in all the existing heavy ion machines. As an example we will give here the results obtained in the BNL Booster – [30]. In this accelerator the vacuum related beam loss has been measured at two different vacuum conditions: the normal operating pressure of  $3 \cdot 10^{-11}$  Torr with over 70% H<sub>2</sub> and for pure vacuum of  $1 \cdot 10^{-9}$  Torr with 50% Ar and 35% CH<sub>4</sub> – Fig. 24. The beam consists of Au<sup>33+</sup> ions and the acceleration cycle lasts 500 ms.

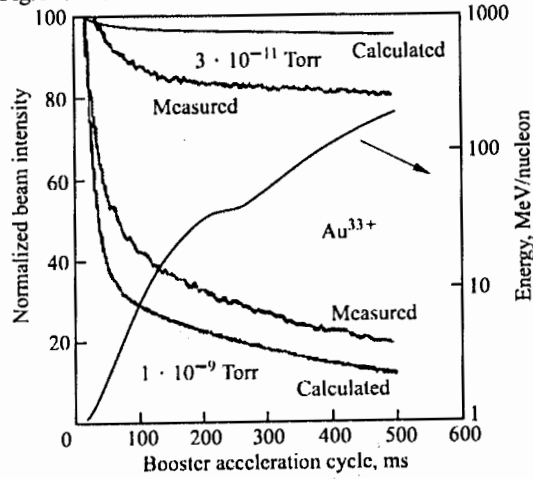


Fig. 24. The fraction of survival Au<sup>33+</sup> beam during the BNL Booster cycle at vacuum levels of  $1 \cdot 10^{-9}$  Torr and  $3 \cdot 10^{-11}$  Torr – [30]

#### 1.2.1.4. Evolution of the Ion Charge State; Equilibrium Charge State Spectrum

As the cross sections for loss and capture of one electron is much larger than the cross sections for loss and capture of two and more electrons the process of change of the initial ion charge  $i_0$  to the final spectrum of charges  $i_1, i_2, \dots$ , is a process of gradual change of the ion charge – Fig. 25.

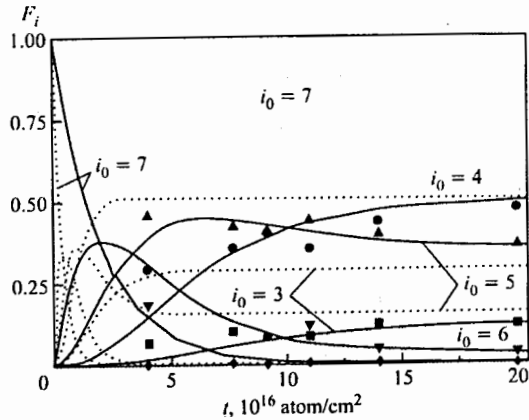


Fig. 25. Evolution of charge state spectrum with the target thickness. Data are for nitrogen ions with initial velocity  $v=3.6v_0$ . Solid lines are for celluloid foil, dashed lines – for gaseous nitrogen targets – [31]

One must take into account that the electron capture cross sections are much less than the electron loss cross sections. For  $Z_{pr} \geq 7$  and  $E_{pr} \geq 0.1Z_{pr}^2$ , MeV/u we can find that:

$$\sigma_{ZZ-1} \leq \frac{1}{8} \sigma_{Z-1,Z} \quad (19)$$

Going deeper and deeper in the target the mean charge of the ion beam is approaching fluently its equilibrium value – Fig. 26.

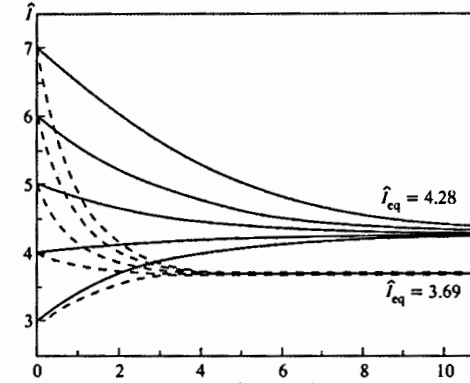


Fig. 26. Evolution of mean charge with the target thickness. The data are for nitrogen ions with initial velocity  $v=3.6v_0$ . Solid lines are for celluloid foils, dashed lines – for gaseous nitrogen targets – [31]

Let  $\Phi_i(t)$  be the yield of ions in charge state  $i$ , after traversing a target with thickness  $t$ , atoms/cm<sup>2</sup>, so that  $\Phi_i(0)$  represents the initial distribution of ions on charge states.

For a monochromatic beam penetrating through matter the change in the charge state distribution is described by the following set of ordinary differential equations – [32]:

$$\frac{d\Phi_i}{dt} = \sum_k \Phi_k \sigma_{ki} - \Phi_i \sum_k \sigma_{ik}, \quad i = 1, 2, \dots, N, \quad (20)$$

where  $\sigma_{ik}$ , with  $i \neq k$ , is the total cross section for changing of the ion charge from the initial value  $i$  to the final value  $k$ , due to the processes of electron capture and loss.

As the target thickness  $t$  increases the charge state spectrum  $\Phi_i(t)$  changes quickly toward an equilibrium charge state distribution  $F_i$ , which does not depend on the target thickness  $t$  and on the initial distribution of ions on charge states  $\Phi_i(0)$ . The equilibrium thickness  $t_{eq}$  depends only on the projectile velocity  $v_{pr}$  and on the nuclear charge  $Z_{pr}$  of the projectile ions and on the target species  $Z_t$ .

The equilibrium charge state spectrum  $F_i$  is a solution of the following system of algebraic equations:

$$\sum_k F_k \sigma_{ki} - F_i \sum_k \sigma_{ik} = 0, \quad i = 1, 2, \dots, N. \quad (21)$$

The equilibrium charge state spectrum is determined by the relations between the electron loss and capture cross sections at the specified beam energy. For the applications it is important that it does not depend on the initial ion beam charge  $i_0$ .

The equilibrium thickness  $t_{eq}$  increases slowly with  $v_{pr}$ .

Along with the charge state distribution the mean charge  $\bar{i}$  and the width of the distribution or standard deviation  $d$  tend to equilibrium.

If  $\bar{i}$  is not too close to 0 or  $Z_{pr}$  the equilibrium charge state distribution  $F_i$  can be approximated by a Gaussian:

$$F_i = \frac{1}{\sqrt{2\pi d^2}} e^{-\frac{(i-\bar{i})^2}{2d^2}}. \quad (22)$$

This distribution has two parameters: equilibrium mean charge  $\bar{i}$  and equilibrium standard deviation  $d$ .

H.H. Beckman and H.D. Betz - [33] have proposed a semiempirical formula for  $\bar{i}$ , which gives good results for gaseous strippers and for  $\bar{i}/Z_{pr} > 0.3$ , i.e. for high projectile energies:

$$\bar{i} = Z_{pr} (1 - \exp(-\frac{v}{v_0 Z_{pr}^{2/3}})) \quad (23)$$

In solids the atomic density is much higher than in gases. Hence in solids the time between two successive collisions of the projectile becomes shorter than the excited level lifetime and the excited ion fails to decay to its ground state before the next collision to occur. Moreover, due to the small interatomic distance in solids the excited states of the ion with high principal quantum number  $n$  are not allowed. These circumstances lead to an increase of the mean charge and of the equilibrium thickness in solid foils compared with gaseous targets - Fig. 27.

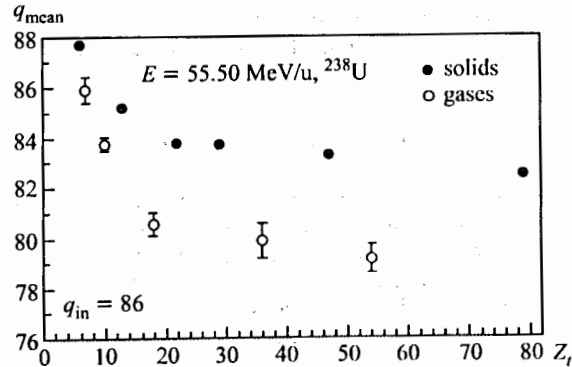


Fig. 27. Mean charge states of  $U^{86+}$  ions at 55.5 MeV/u passing through gaseous and solids as a function of the target atomic number  $Z_t$  - [34]

According to measurements - [35] the projectile energies, necessary to reach 80% yield of bare ions in passing through Al foils are: 570 MeV/u for Au and 1.1 GeV/u for

U species - Fig. 28. The equilibrium thicknesses of the Al foil are 210 mg/cm<sup>2</sup> and 360 mg/cm<sup>2</sup> respectively. Half of these thicknesses will still provide 65-70% bare ions.

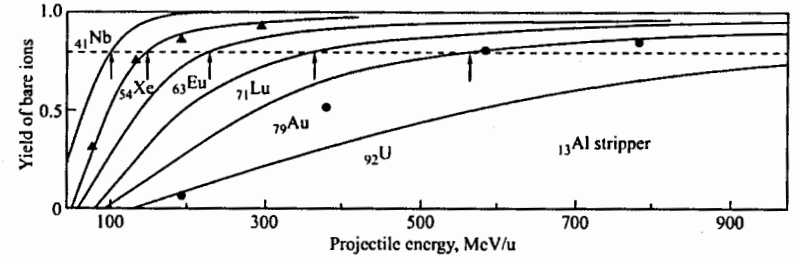


Fig. 28. Fractional yields of bare ions in Al foil as a function of projectile energy (the dashed line indicates 80% yield level) - [35]

V.S. Nikolaev and I.S. Dmitriev - [36] have proposed a semiempirical formula for mean charge in solid strippers:

$$\bar{i} = Z_{pr} [1 + (\frac{v}{v' Z_{pr}^{2/3}})^{-1.67}]^{-0.6}, \quad (24)$$

where  $v' = 3.6 \cdot 10^8$  cm/s.

For standard deviation V.S. Nikolaev and I.S. Dmitriev - [36] have proposed the expression:

$$d = 0.5 \sqrt{\bar{i} (1 - (\frac{\bar{i}}{Z_{pr}})^{1.67})}. \quad (25)$$

For sufficiently high ion energies only two charge state fractions  $\Phi_{z-1}$  and  $\Phi_z$  prevail and should be taken into account. Experiments show that for projectile energies greater than  $T_n \geq 0.17 Z_{pr}^2$  the contribution of all the charge state fractions other than  $Z$  and  $(Z-1)$  is less than 3%. For this particular case the solution of (20) is:

$$\Phi_i(t) = F_i + \Delta\Phi_i e^{-\kappa t}, \quad (26)$$

where  $\Delta\Phi_i = \Phi_i(0) - F_i$  and  $\kappa = \sigma_{z-1,z} + \sigma_{z,z-1}$ .

It can be found from (26) that the equilibrium thickness (with 99% accuracy) is given by the formula:

$$t_{99} = \frac{4.6}{\sigma_{z-1,z} + \sigma_{z,z-1}}, \frac{at}{cm^2}. \quad (27)$$

Stripping of fast moving heavy ions is widely used in accelerator practice both for charge exchange injection or to increase the charge of the ions for their further acceleration - [37]. The latter option is traditional for the heavy ion accelerator complexes.

In BNL accelerator complex the Au<sup>33+</sup> ion beam accelerated in the Booster to kinetic energy of 192 MeV/u passes later through a 56 mg/cm<sup>2</sup> thick carbon stripping foil to be stripped to Au<sup>77+</sup>. The thickness of the carbon foil was chosen to give the maximum yield of Au<sup>77+</sup> ions. The space charge spectrum after the stripping is shown on Fig. 29. The maximum Au<sup>77+</sup> ion yield is 65%.

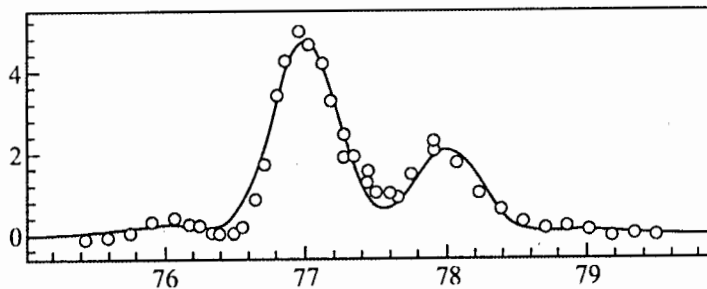


Fig. 29. Charge state spectrum of Au<sup>33+</sup> ions at 192 MeV/u stripped by a 56 mg/cm<sup>2</sup> carbon foil – [37]

For producing of fully stripped uranium an energy of at least 500 MeV/u is required.

The equilibrium charge state spectra of uranium projectiles behind Ta and Cu foils at two energies: 437 MeV/u and 962 MeV/u are represented in Table 4.

Table 4. The equilibrium charge state spectra of uranium projectiles behind Ta and Cu foils at 437 MeV/u and 962 MeV/u

Stripping foil	Charge state spectrum at 437 MeV/u			Charge state spectrum at 962 MeV/u	
	90+	91+	92+	91+	92+
Ta, 85 mg/cm <sup>2</sup>	25	50	30	10	90
Cu, 150 mg/cm <sup>2</sup>	15	40	45	15	85

Equilibrium charge state spectra of U ions penetrating C-foils, as they have been measured in the GSI accelerator complex, are shown on Fig. 30. The left spectrum was measured at the UNILAC behind a 40 μg/cm<sup>2</sup> thick target for energy of 1.4 MeV/u. The distribution depicted in the middle of Fig. 29 was obtained behind a 490 μg/cm<sup>2</sup> target and at energy of 11.4 MeV/u. The spectrum displayed on the right was measured at SIS-18 synchrotron behind a 400 mg/cm<sup>2</sup> target at 940 MeV/u.

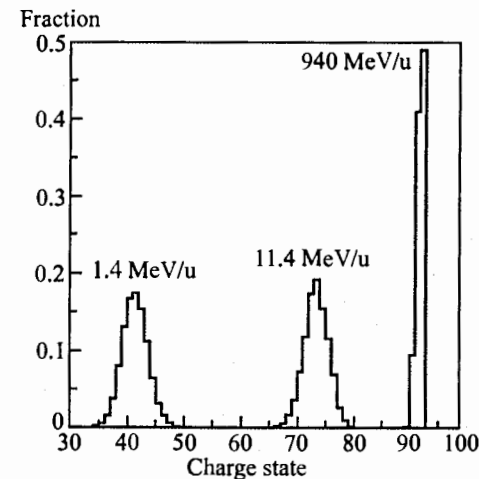


Fig. 30. Equilibrium charge state spectra of U projectiles behind C-foils

#### 1.2.1.5. Energy Loss

The mean energy loss due to excitation and ionization of the target atoms is well described by the Bethe – Bloch equation – [38]:

$$\frac{dE}{dt} = -\frac{0.3070Z_t}{A_t} \left(\frac{Z_{pr}}{\beta_{pr}}\right)^2 \ln\left(\frac{2m_e c^2 \beta_{pr}^2 \gamma_{pr}^2}{\bar{I}}\right), \frac{MeV}{g/cm^2}, \quad (28)$$

where  $t$  is the target thickness in g/cm<sup>2</sup>,  $m_e$  – the electron mass,  $\beta_{pr}$ ,  $\gamma_{pr}$  – the projectile reduced velocity and energy (relativistic factors) and  $\bar{I} \approx 13.6Z_t, eV$  is the mean ionization potential of the target atoms.

The energy loss straggling is small and could be neglected in most cases. But it must be taken into account in some specific circumstances. One such case is when the energy loss in single internal/stripping target crossing is comparable with the momentum acceptance of the machine.

The statistical distribution of ionization losses is governed by Landau's, Vavilov's or Gaussian distribution functions depending on the projectile charge and velocity. There exist standard computer subroutines that calculate these functions, for example in the CERN computer code library.

The ionization loss of energy plays an important role in the charge exchange injection as it increases the relative momentum spread. The value of momentum spread is determined by the spread in the number of stripping foil traversals and by the velocity and species of the injected ions.

Measured energy loss of U<sup>86+</sup> ions at 60.23 MeV/u behind Al foil are shown on Fig. 31 – [34].

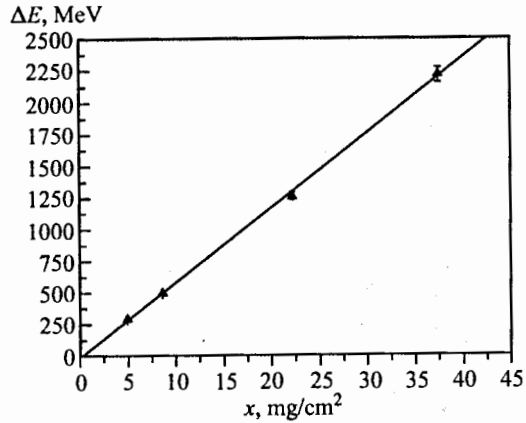


Fig. 31. Measured energy loss vs. target thickness of an incident  $U^{86+}$  beam at 60.24 MeV/u penetrating aluminum foils of various thicknesses. The data are fitted with a straight line – [34].

The real phenomenon is more complicated as starting from the initial charge state the charge content of the beam evolves gradually to equilibrium charge distribution as the particles penetrate in the foil. More precise theoretical results about the stripping force can be obtained by the simulating computer codes GLOBAL – [34] and ETACHA – [39]. For a comparison between theoretical predictions and measurements we will present here the data obtained for  $U^{86+}$  ions at 58.74 MeV/u behind a C – foil. While the theoretical stopping force is:  $-\frac{dE}{dx} = 65.69, \frac{MeV}{mg/cm^2}$ , the measurements point out the value:  $-\frac{dE}{dx} = 66.50, \frac{MeV}{mg/cm^2}$ .

### 1.2.1.6. Elastic Scattering

The multiple Coulomb scattering of the projectile ions in the stripping foil or in the molecules of the residual gas in the accelerator vacuum chamber causes changes of the trajectory slope and hence transverse emittance growth. The transverse emittance growth when a beam of relativistic ions crosses a solid foil many times is one of the major limiting factors for the charge exchange injection of protons and heavy ions. Multiple Coulomb scattering in residual gas molecules also must be taken into account especially in heavy ion storage rings and colliders.

The following empirical formula can be used for mean square scattering angle of heavy ions passing through solid foils – [40]:

$$\langle \theta^2 \rangle = 0.250 \frac{Z_t(Z_t+1) Z_p^2 t}{A_r E_{pr}^2}, \quad (29)$$

where  $\theta$  is in mrad, the stripper thickness  $t$  is in  $\mu g/cm^2$  and the projectile energy  $E_{pr}$  is in MeV.

A useful expression for the speed of increase of the scattering angle when ions interact with the molecules of the residual gas is given by B. Franzke – [41]:

$$\frac{d\langle \theta^2 \rangle}{dt} = 4.8 \cdot 10^{-4} P [m_t Z_t^2 \ln \left( \frac{204}{Z_t^2} \right)] \left( \frac{Z_{pr}}{A_{pr}} \right)^2 \frac{1}{\beta_{pr}^2 \gamma_{pr}^2}, \quad (30)$$

where  $m_t$  is the number of atoms per molecule and  $P$  is the residual gas pressure in mbar. The formula is valid for room temperature. The speed of scattering angle increase is in rad/s. The values of the “target factor”, given in the square brackets are presented in Table 5 for molecules that are typical for a UHV system.

Table 5. Values of “target factor” in Franzke’s formula for the speed of scattering angle increase in ion interactions with the residual gas

Molecule	$m_t Z_t^2 \ln \left( \frac{204}{Z_t^2} \right)$
H <sub>2</sub>	10.6
He	20.3
Ne	455
N <sub>2</sub>	485
CO	466
O <sub>2</sub>	592
CO <sub>2</sub>	762
Ar	1411

From the above table it becomes obvious that the fraction of heavy atoms in the residual gas must be as small as possible.

The change of the transverse RMS emittance which is caused by the elastic scattering is given by – [42]:

$$\epsilon_N = \epsilon_0 + 2N\beta^* \langle \theta^2 \rangle, \quad (31)$$

where  $\epsilon_0$  is the initial emittance,  $\beta^*$  is the value of the amplitude function at the foil and  $N$  is the number of foil passages.

If the dispersion at the stripper is nonzero the ionization loss of energy, described in the previous point, also will cause transverse emittance growth. This kind of emittance growth could be evaluated by the formula:

$$\sqrt{\beta^* \epsilon} = \sqrt{\beta^* \epsilon_0} + N \sqrt{(D^* \Delta \delta)^2 + (D'^* \Delta \delta)^2} \quad (32)$$

or when  $D'^* = 0, \Delta \delta \ll 1$ :

$$\epsilon \approx \epsilon_0 + \frac{2D^* x_{\beta}^* N \Delta \delta}{\beta^*}, \quad (33)$$

where  $D^*$  and  $D'$  are the linear and angular dispersion at the stripper,  $\delta = \Delta p / p = (1/\beta^2)\Delta E/E$  is the relative momentum spread and  $x_\beta^* = \sqrt{\beta^* \epsilon_0}$ .

The transverse beam emittance growth is of big importance for the realization of the charge exchange injection in synchrotrons.

### 1.2.2. Dynamic Vacuum Problems

The intensity related vacuum instability was first observed in ISR by O. Gröbner and R. Calder – [43]. The initial vacuum pressure in the proton-proton collider was  $1 \cdot 10^{-10}$  Torr. It was noticed that when the beam current had increased 4 A the vacuum pressure started to rise reaching  $10^{-7} - 10^{-6}$  Torr level and the beam was destroyed – Fig. 32.

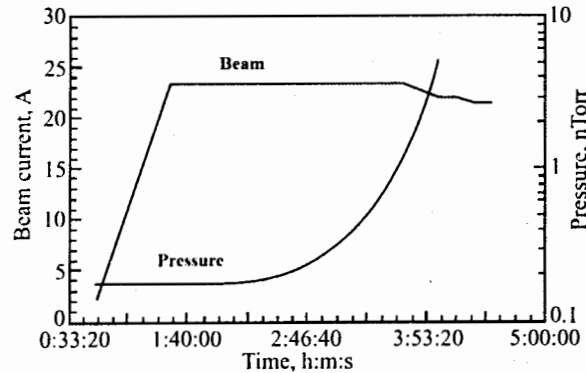


Fig. 32. Pressure instability during beam accumulation in the ISR – [43]

Another case of runaway type pressure rise in ISR is shown on Fig. 33.

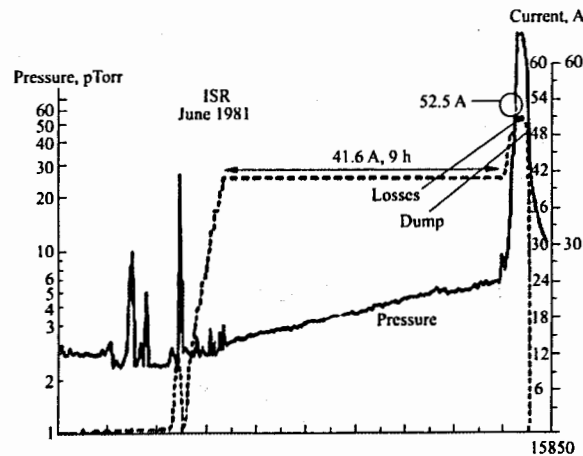


Fig. 33. ISR runaway type pressure rise

The mechanism of this kind of pressure instability is believed to be the following – [44, 45]. Accelerated proton beam ionizes the molecules of the residual gas. A large number of electrons and positive ions are created. The ionization cross section  $\sigma_{ion}$  in  $m^2$  for particles with charge  $eZ_{pr}$ , moving with velocity  $\beta = vc$  and hitting a residual gas molecules could be estimated by the formula:

$$\sigma_{ion} = 1.874 \cdot 10^{-24} \frac{Z_{pr}^2}{\beta^2} (Ax + B), \quad (34)$$

where:  $A, B$  are coefficients, specific for the hit molecule and  $x = 2 \ln(\beta\gamma) - \beta^2$ .

The positive ions are repelled by the positive space charge of the beam towards the vacuum chamber walls. For protons a typical beam potential is 100 V per 1 A. Hence for high current machines the energy of the bombarding ions can reach several hundred eVs. This causes desorption of tightly bound surface gas. The outgassing increases the pressure in the vacuum chamber of the accelerator, which in turn leads to more intensive ionization. A positive feedback could be created. The phenomenon is schematically depicted on Fig. 34.

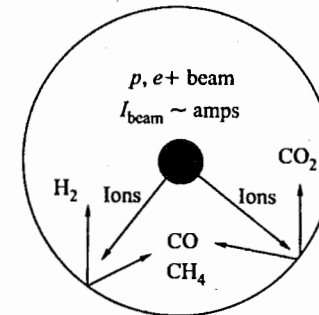


Fig. 34. Principle of ion induced pressure instability – [45]

The ion induced pressure instability was one of the major factors limiting the stored proton beam intensity.

For room temperature vacuum systems CO is the most dangerous component of the residual gas due to its large ionization cross section and to its high ion induced desorption yield.

Let's look at the ion induced pressure instability in a more quantitative way. The outgassing flux  $Q$  in  $\text{Torr} \cdot m^3 \cdot s^{-1}$  for a slice  $dx$  of the vacuum chamber is:

$$Q = \eta \sigma \frac{I}{e} P dx + q_0 dx, \quad (35)$$

where:  $\eta$  is the molecular desorption coefficient, i.e. the number of molecules released for an ion hitting the walls;  $\sigma$  is the residual gas ionization cross section;  $I$  – the total beam current;  $e$  – proton charge;  $P$  – vacuum pressure;  $q_0$  – the specific thermal outgassing rate from the walls in  $\text{Torr} \cdot m^2 \cdot s^{-1}$ .

For the simplest linear vacuum system which consists of vacuum pumps with pumping speed  $S$  in  $m^3 \cdot s^{-1}$  and which are spread through a distance  $L$  the critical beam current at which a pressure runaway starts is – [45]:

$$(\eta I)_{crit} = \frac{\pi^2 \epsilon c_0}{\sigma l^2}, \quad (36)$$

where:  $c_0$  is the specific conductance of the vacuum chamber in  $\text{m}^4 \cdot \text{s}^{-1}$ .

The formula (36) is valid for conductance limited vacuum system, i.e. when the pumping speed  $S$  is large and the conductance  $c_0$  is small.

The ion induced desorption yield  $\eta$  is  $\eta = 1 - 8$  for non-bakable stainless steel vacuum system and strongly depend on the ion energy. For bakable vacuum system  $\eta = 0.1 - 1.2$  – Fig. 35.

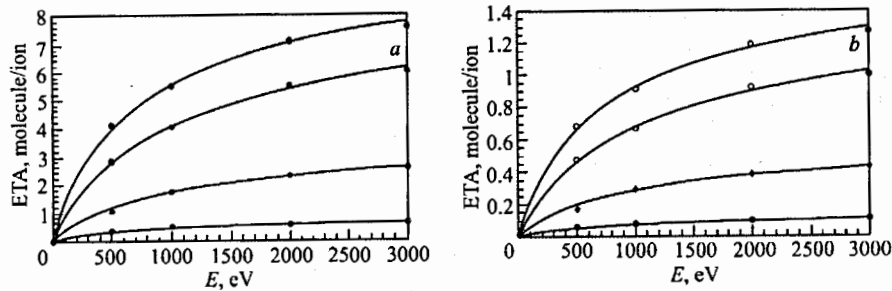


Fig. 35. Desorption yield for baked and unbaked stainless steel vacuum chamber – [51]

The case of heavy ion machines is quite different. In proton storage rings like ISR the stored current is very high and the beam potential can reach up to 2 kV. On the contrary in heavy ion accelerators the beam potential is rather low. In LEIR it is about 10 V. In SIS-18 the space charge potential for  $\text{U}^{28+}$  at injection energy is about 50 eV. In such a weak electric field the residual gas ions are not accelerated enough to produce high desorption rate.

In spite of this pressure bumps up to  $10^{-9}$  Torr have been observed in LEAR during continuous injection of  $10^8$  ions/s (the initial static pressure in the machine was  $5 \cdot 10^{-12}$  Torr) – [46]. It was found that the outgassing of the vacuum equipment is due to the impact of lost  $\text{Pb}^{54+}$  ions – the so-called beam loss induced pressure rise.

Vacuum pressure instabilities were also observed in AGS – Booster – [47] and in SIS-18 – [48].

In the ion collider RHIC during 2001 high-intensity Au run, when the intensity was raised beyond  $8 \cdot 10^8$  ions/bunch, pressure rises of several decades were measured – [49, 50]. The rapid pressure rises sometimes exceeded the control electronics threshold and the beam was aborted – Fig. 36. The pressure rise was especially prominent during 110-bunch gold injection. The pressure instability was recorded in the warm sections of the ion collider. The designed vacuum in these room temperature regions with overall length 1.4 km is less than  $5 \cdot 10^{-10}$  Torr. Even 5% beam loss per 10 m gives rise to serious experimental background problems in the interaction regions.

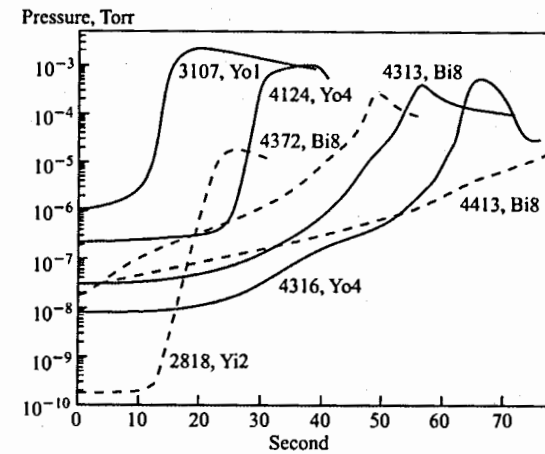


Fig. 36. RHIC pressure bumps during run 2003 and run 2004. All cases are for gold beams and unbaked vacuum chamber – [51]

There are several potential mechanisms that could cause the pressure instability in ion accelerators:

- Ion induced desorption caused by the primary beam loss. In synchrotrons the largest beam loss occurs during injection and RF-capture. The lost primary ions hit the vacuum chamber walls at grazing angles of mrad or less. In such hits more than  $10^5$  molecules can be released per lost ion. Indeed measurements in AGS Booster, LEAR, SIS-18 and RHIC show desorption rates as large as  $10^5$  and even  $10^7$  – Fig. 37;

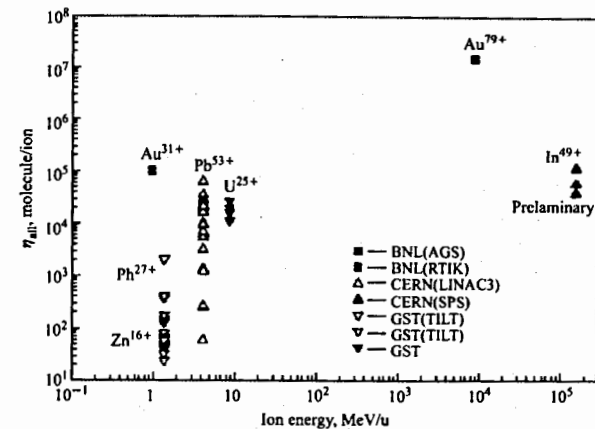


Fig. 37. Overview of ion induced desorption data obtained at BNL, CERN and GSI

- The charge exchange of beam ions with residual gas atoms and molecules is another potential source of large amount of lost ions. The beam ions that had lost or captured electrons leave the beam and hit the walls of the vacuum chamber at grazing angles. Such

grazing angle ion hits can desorb large amount of gas molecules and cause direct beam loss induced pressure instability;

- The pressure rise could be caused also by an electron cloud. The electrons in a cloud bombard the walls and could desorb gas molecules. The phenomenon is known as electron multipacking. This kind of pressure instability is sensitive to bunch intensity and to bunch spacing.

In the cryogenic vacuum systems molecules are cryopumped with high efficiency directly on the cold walls.

The estimations made for LHC – [52], pointed out that the critical beam current is:

$$(\eta I)_{crit} = \frac{\pi}{2} \bar{v} s \tau_p \frac{\sigma}{\sigma}, \quad (37)$$

where:  $\bar{v}$  is the mean molecular velocity,  $s$  is the sticking probability of molecules on the walls,  $\sigma$  – the ionization cross section,  $r_p$  – radius of the cold beam pipe.

For  $s = 1$  the critical current becomes very large, in the order of kA. However this optimistic value can be reduced to a great extent by condensed gas, especially  $H_2$ , accumulated on the cold bore, which can produce molecular desorption yield up to  $10^4$  molecules per ion.

The following measures could help to cope with vacuum pressure instability:

- Very strict choice of materials and vacuum pumps; use of distributed pumping; negligible amount of leaks in the vacuum chamber,
- Surface cleaning of the vacuum chamber walls by means of argon glow discharge,
- Provision for bakeout in place up to 200° C for 24 h,
- Beam scrubbing,
- Use at strategic locations of low outgassing materials as noble metal coatings or thin evaporated films of titanium,
- Distributed pumping by ribbons of Non-Evaporable Getters (NEG) for increase the local pumping speed,
- Cooling of vacuum chamber walls.

### 1.2.3. Intrabeam Scattering

The intrabeam scattering (IBS) phenomenon consists in multiple small-angle Coulomb scattering of particles within relativistic beams. The random addition of a large number of small angle scatterings causes the beam size to grow. This sets strong limitations on the luminosity lifetime in hadron and ion colliders.

The emittance growth due to the multiple Coulomb scattering in electron beams was first considered by H. Bruck and J. Le Duff – [53].

For proton beams IBS was first analyzed by A. Piwinski in a more general treatment – [54].

It is the coupling between the longitudinal and the transverse motions via the dispersion in what a beam of particles in a circular accelerator differs from a gas of molecules. Because of the dispersion an energy change leads to a change in the betatron amplitudes. A coupling of the longitudinal and the transverse motions exists.

The border line between the regions where the effect of coupling is important or it could be neglected is studied in – [55]. It is determined by the condition that the contribution to the beam width due to betatron oscillations equals the contribution which is due to the

coupling via dispersion,  $(\epsilon_x \beta_x)^{1/2} = D \frac{\Delta p}{p}$ . For high energies (above transition) the coupling

may be neglected and IBS can in good approximation be described by the gas-relaxation formulae independently of the ring lattice – [56].

In early theoretical works averaged lattice functions have been used for simplicity. In a smooth lattice approximation the Hamiltonian in a frame, moving along with the synchronous particle (the so-called particle frame, PF), is independent on time, i.e. the dynamical system is conservative. In smooth approximation the total beam temperature in PF is conserved.

The smooth lattice approximation is rough and has been later abandoned in favour of more realistic models that take into account the variation of the lattice functions around the ring – [57, 58].

In Martini's paper an improved Piwinski's model has been introduced. The paper of Bjorken and Mtingwa uses the S-matrix approach. This latter formalism is included in the MAD code.

The two approaches assume that the particle distribution remains Gaussian in the six-dimensional phase space. The IBS growth rates are expressed with complicated integrals. They are calculated locally and after that averaged over the ring. The price you must pay is that the calculations are computationally intensive.

Both Bjorken and Mtingwa's and Martini's models are in good agreement with one another. It is also commonly accepted that for high energies, i.e. above transition, Martini's and Bjorken and Mtingwa's models are able to describe IBS effect with accuracy better than 50%.

The IBS has different behavior below and above the transition energy.

Below the transition energy,  $\gamma < \gamma_t$ , when the beam is in the positive mass regime, the behavior of the beam particles is similar to that of a gas in a closed box. Each degree of freedom exchanges energy with the others according to their relative temperatures. Because in typical situations the transverse temperature is higher than the longitudinal a cooling in transverse planes could take place. Below the transition energy the beam can reach equilibrium between the transverse and longitudinal temperatures. The sum of horizontal, vertical and longitudinal oscillation amplitudes remains limited. Such a behavior has not yet been observed in high energy storage rings.

The transverse temperature is:

$$kT_{\perp} = m_i c^2 \beta^2 \gamma^2 Q \frac{\epsilon_{\perp}}{R}, \quad (38)$$

where  $m_i$  is the ion mass,  $Q$  – the betatron tune,  $\epsilon_{\perp}$  – transverse emittance,  $R$  – mean radius,  $\beta$ ,  $\gamma$  – the relativistic factors. The transverse beam temperature is proportional to the transverse emittance.

The longitudinal temperature is determined by:

$$kT_{\parallel} = m_i \beta^2 c^2 \left(\frac{\Delta p}{p}\right)^2, \quad (39)$$

i.e. is proportional to the square of relative momentum spread.

Above the transition energy,  $\gamma > \gamma_t$ , due to the fact that the beam is in negative mass regime, inter-particle collisions cause an exchange of energy from the directed motion of the relativistic beam into energy in all three directions. The beam grows in all three dimensions

and no equilibrium exists. This can happen even in the case of uniform machine lattice. For energies that are much higher than the transition energy ( $\gamma \gg \gamma_t$ ) the IBS is dominated by longitudinal diffusion.

The coupling between the horizontal and the vertical motions (if exists) averages the growth rates in both transverse directions.

Accurate computation of IBS effects can be performed only with computer simulations. Two widespread computer codes that could simulate IBS effects are: BETACOOOL developed by I. Meshkov, A. Sidorin et al. – [59] and SIMCOOL developed by V. Parkhomchuk and I. Ben-Zvi – [60].

BETACOOOL code calculates IBS taking into account the real lattice of the accelerator. It incorporates the Martini's model. SIMCOOL code is based on a treatment of the IBS based on the plasma approach.

Several approximate approaches that simplify the calculation of IBS effects have been devised. Very promising is the approach of J. Wei, who has succeeded in improving the accuracy and the speed of calculations – [61].

For the case of nearly constant ratio  $D/\sqrt{\beta_x}$ , where  $D$  is the dispersion and  $\beta_x$  – the Twiss amplitude function, as is in a FODO lattice, J. Wei has simplified the formula for emittance growth rates to:

$$\begin{bmatrix} \frac{1}{\sigma_p} \frac{d\sigma_p}{dt} \\ \frac{1}{\sigma_x} \frac{d\sigma_x}{dt} \\ \frac{1}{\sigma_y} \frac{d\sigma_y}{dt} \end{bmatrix} = \frac{Z^4 N}{A^2} \frac{r_0^2 L_c c}{8 \pi \gamma \varepsilon_x^* \varepsilon_y^* \varepsilon_l^*} F(\chi) \begin{bmatrix} n_b (1-d^2) \\ -\frac{a^2}{2} + d^2 \\ -\frac{b^2}{2} \end{bmatrix}, \quad (40)$$

where:  $\sigma_x$  is horizontal rms betatron amplitude,  $\sigma_y$  – the vertical rms betatron amplitude,  $\sigma_p$  – the rms fractional momentum deviation,  $Z$  – ion charge state,  $A$  – ion mass number,  $N$  – for bunched beams is equal to the number of particles per bunch while for unbunched beams it is equal to the total number of particles,  $r_0$  is the classical proton radius,  $L_c$  is the Coulomb logarithm,  $L_c = \ln \frac{b_{max}}{b_{min}} = \ln \frac{2}{\theta_{min}}$ ,  $b_{min}$  and  $b_{max}$  being the minimum and maximum impact parameters,  $\theta_{min}$  being the minimum scattering angle; approximately  $L_c \approx 20$ . In (40)  $\varepsilon_x^*$ ,  $\varepsilon_y^*$  are the normalized transverse rms emittances and  $\varepsilon_l^*$  is the normalized longitudinal rms emittance.

$$\varepsilon_{x,y}^* = \beta \gamma \frac{\sigma_{x,y}^2}{\beta_{x,y}}, \quad (41)$$

$$\varepsilon_l^* = \beta \gamma \sigma_p \sigma_S, \quad (42)$$

where  $\sigma_S$  for bunched beams is equal to the bunch rms length, while for unbunched beams it equals  $\sqrt{\pi R}$ .

$$n_b = \begin{cases} 1, & \text{for bunched beam} \\ 0, & \text{otherwise} \end{cases}, \quad (43)$$

$$d = \frac{D \sigma_p}{\sqrt{\sigma_x^2 + D^2 \sigma_p^2}} < 1, \quad (44)$$

$$a = \frac{\beta_x d}{D \gamma}, \quad (45)$$

$$b = \frac{\beta_y \sigma_x}{\beta_x \sigma_y} a. \quad (46)$$

In (40)  $F(\chi)$  is an defined analytic function.  $F(\chi)$  is a smooth function of  $\chi$ . It is positive when  $\chi < 1$ , zero when  $\chi = 1$  and negative when  $\chi > 1$  – Fig. 38.

$$\chi = \frac{a^2 + b^2}{2}. \quad (47)$$

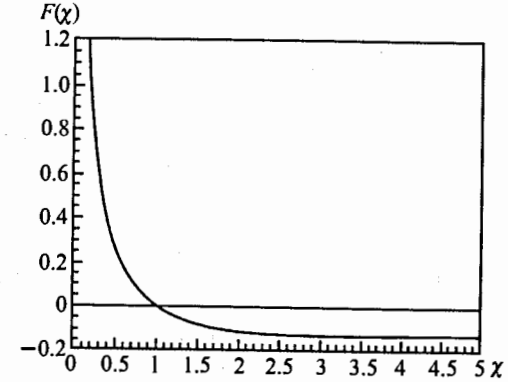


Fig. 38. Function  $F(\chi)$

The emittance growth rates are proportional to the particle density in the 6-D phase space  $\frac{N_b}{\varepsilon_x^* \varepsilon_y^* \varepsilon_l^*}$  and are inversely proportional to the particle energy. For heavy ions the factor

$\frac{Z^4}{A^2}$  is of big importance.

The J. Wei's simplified description has been tested with Au ions at RHIC – [62]. At store energy, i.e. above transition, the measurements and the calculations agree rather well both for the bunch length and for the transverse emittances growth rates. At injection energy, i.e. below transition, the agreement between the theory and the experiment is a bit worse for the bunch length growth rate. But whereas the theory gives a slight decrease of the transverse emittances, the measurements have always shown a growth. This growth has been linear in

time. For that reason the authors have considered that a diffusion process due to strong noise source has been observed.

It is the IBS that is the most severe drawback which restricts the average luminosity in RHIC – [62]. This is due to the high charge state of the gold ions. At injection into RHIC the IBS growth time for the momentum spread is about 3 minutes. Emittances in both the longitudinal and transverse dimensions grow up. IBS limits beam and luminosity lifetimes and leads to particle loss out of the RF buckets.

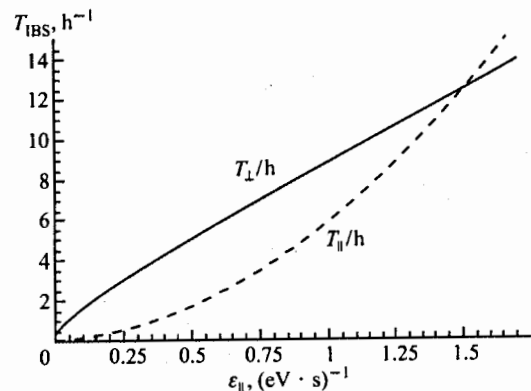


Fig. 39. Emittance growth times due to IBS as a function of the longitudinal emittance.  $^{208}Pb^{82+}$  ions at injection from the SPS. The solid line represents the growth time for the horizontal emittance while the dashed line – for the longitudinal emittance – [64]

Beam cooling must be applied to cope with luminosity reduction. In RHIC R&D works are under way for bunched beam electron cooling at collision energy – [63]. The electron cooling system is based on an energy recovering linac. The electron beam will be with energy of 54 MeV and current 100 - 200 mA. Ten times increase of the average luminosity is anticipated.

The calculated IBS growth times for LHC lead ion beams of nominal intensity at injection from the SPS are shown on Fig. 39.

Recently electron cooling of 8 GeV antiprotons at Fermilab's Recycler Storage Ring was successfully realized – [65]. The cooler utilizes a DC electron beam generated by an Pelletron-type electrostatic accelerator that operates in energy recovering mode – Fig. 40.

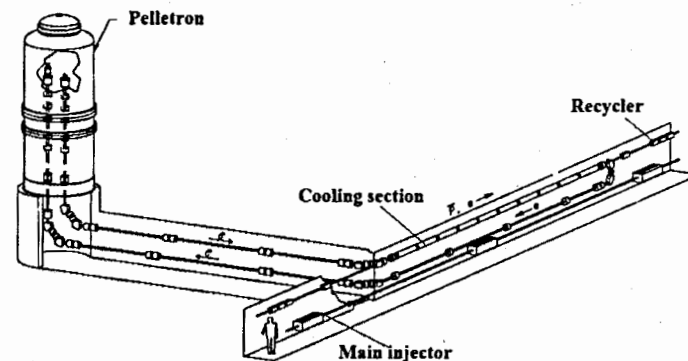


Fig. 40. High energy electron cooling system in Fermilab's Recycler Ring – [65]

The kinetic energy of electrons is 4.3 MeV and the electron current is 0.5 A.

Increasing the longitudinal phase-space density of the antiproton beam the electron cooling system results in significant luminosity increase in Tevatron proton-antiproton collider.

#### 1.2.4. Electron Cloud Effects

Electron cloud effect consists in formation of a cloud of low energy background electrons that accompany the beam. Building-up of an electron cloud has been observed in both accelerators of light positively charged particles (positrons) and in proton and heavy ion accelerators. Some review papers devoted especially to the electron cloud phenomena are – [66-68].

There are several processes that result in production of electrons in an accelerator. These processes are:

- Ionization of residual gas molecules by the beam. The ionization cross-section for relativistic particles and CO residual gas molecules is 1-2 Mbarn;
- Generating of electrons in crossing stripping foils;
- Generating of electrons as a result of chamber walls bombardment by lost particles. In high intensity proton accelerators the fractional loss of particles per turn  $r_{loss}$  must be very small. Thus for Los Alamos proton storage ring PSR  $r_{loss} = 4 \cdot 10^{-6}$  while for the Oak Ridge spallation source SNS  $r_{loss} = 1 \cdot 10^{-7}$ . The number of electrons generated per incident proton in these machines is about 100;
- Photoelectron production when the chamber walls are irradiated by synchrotron radiation emitted by the beam particles. The photoelectron yield per absorbed photon  $Y^*$  has typical values about 0.1.

Photoelectron emission dominates over the other processes in lepton accelerators and in proton machines for very high energy. For LHC the rate of photoelectron production is 9 orders of magnitude higher than the rate of electron production by residual gas ionization. The residual gas ionization and the beam losses are the main source of electrons in low and intermediate energy proton and heavy ion accelerators.

In cases of positively charged beams (positrons, protons or heavy ions) the primary electrons are accelerated toward the beam.

For a coasting beam the beam potential is:

$$V(r) = \frac{eZ\lambda}{2\pi\epsilon_0} \begin{cases} -\frac{r^2}{2a^2} + \frac{1}{2} + \ln\left(\frac{b}{a}\right), & r < a \\ \ln\left(\frac{b}{r}\right), & b > r > a \end{cases} \quad (48)$$

where:  $b$  – vacuum chamber radius,  $a$  – beam radius,  $\lambda$  – beam linear density.

Electrons are trapped by this potential and start to oscillate – Fig. 41.

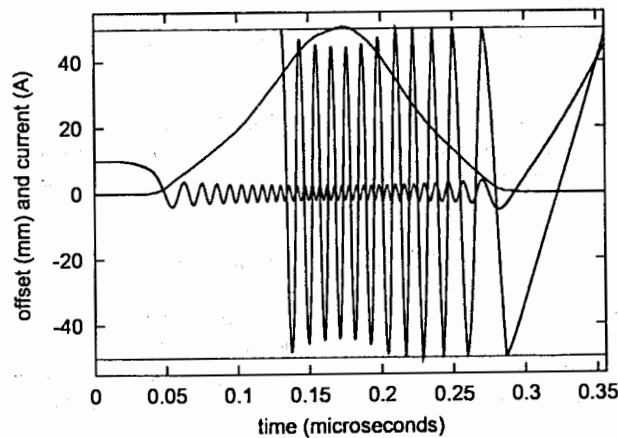


Fig. 41. Proton beam current and trajectories of an electron captured by the bunch and of an electron that undergo large amplitude oscillations. The values in the figure are typical for the PSR proton ring – [68]

If the electrons gain enough energy they become a source of secondary electrons in heating the chamber walls – Fig. 42.

Generally speaking when an electron strikes the chamber walls it may be reflected rediffused or stopped. If the secondary electron emission yield (SEY) is greater than unity ( $SEY > 1$ ) an electron cloud (EC) around the beam is build-up and grows exponentially. SEY depends on the incident electron energy, the incident angle, the material of the walls and on the surface conditioning. Whether or not the EC density will increase depends on many factors as: beam current, bunch length and spacing, secondary electron emission yield (SEY) and photoelectron emission yield ( $Y^*$ ), vacuum chamber geometry and the chamber walls conditioning. If the EC density becomes too large the beam-EC interaction can degrade the accelerator performance.

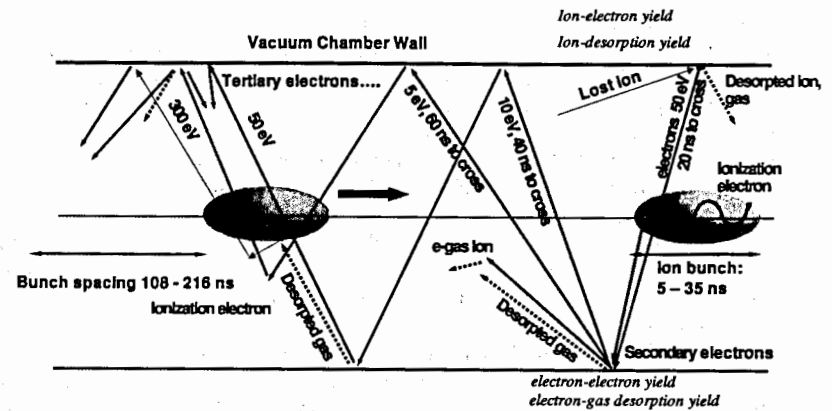


Fig. 42. Electron cloud effects at RHIC. Primary electrons are produced by ionization of the residual gas or by beam lost particles striking the walls. Electrons close to the walls change only their moments (kick); electrons close to the beam are trapped inside the bunch potential and start to oscillate – [69]

The EC density increases until saturation is reached when the electron space charge field becomes equal to the beam field. This process is known as beam induced multipacting (BIM).

The EC effects were first discovered at Novosibirsk in 1967 – [70]. The specialists from BINP have tried to increase the space charge limit neutralizing proton beams by electrons when an unusual transverse instability occurred. This instability has been explained by G.I. Budker as coupled oscillations of electrons and protons.

In 1971 electron cloud build-up was observed in ISR proton storage ring working with a high intensity coasting beam – [71,72]. The phenomenon expresses in coupled oscillations of protons and trapped electrons that hinder the high current operation. In the ISR case the electrons were produced by residual gas ionization. This pointed the way to cope the problem – increasing the pumping power and the use of cleaning electrodes.

From a simplified model O. Grobner – [73] has deduced that the beam intensity just on the onset of EC is:

$$N_{th} = \frac{b^2}{r_e L_{hh}} \quad (49)$$

where:  $L_{hh}$  – the distance between the successive bunches,  $r_e$  – the classical electron radius.

For the case of LHC this rough estimation gives  $N_{th} = 2.3 \cdot 10^{10}$  p/bunch.

For bunched beams the EC build-up depends on the ratio of the electron oscillation period to the bunch length and bunch spacing and naturally on the beam current. The ratio of the time for which electrons cross the vacuum chamber to the bunch spacing is also of great importance. One can easily show – [74] that electrons produced at the walls will gain significant energy when they are produced on the trailing edge of the bunch i.e. when the bunch density is decreasing. In this case the primary electrons gain enough energy to produce secondaries if SEY exceeds unity. This process is known as trailing edge multipacting. Electrons produced at low radii or before the bunch passage are captured by the beam

potential. These electrons don't produce secondaries but they are responsible for different kind EC instabilities. The trailing edge multipacting occurs when the electrons emitted from the walls are accelerated by the e.m. field of the passing bunch to such extent that this primary electrons strike the opposite vacuum chamber wall just before the next bunch to arrive. Then the e.m. field of this second bunch accelerates the secondary electrons.

The electron cloud build-up in an accelerator operating in bunched beam mode was first observed in ISR in 1977 – [75]. After installing of aluminum alloy vacuum chamber instead of a stainless steel one a very fast pressure rise was indicated due to desorption of deeply absorbed in the chamber walls gas molecules under intensive electron bombardment. The effect strongly depends on the bunch current. Latter the molecular desorption induced by electron bombardment has been observed in KEKB and PEP-II positron (LER) rings and in SPS working with LHC-type beam.

The process of EC build-up is quite different in presence of external e.m. fields. Thus in a vertical dipole magnetic field the electron motion is restricted only to the vertical direction. In such field electrons don't experience any horizontal kick by the nearby moving bunch. The computer simulations show that in these conditions the electrons are concentrated in two stripes situated symmetrically with respect to the beam. This conclusion was later confirmed experimentally in SPS working with LHC-type beam.

In 1989 in KEK photon factory working with positrons a kind of multi-bunch instability was observed. This instability was explained in 1995 by K. Ohmi – [76] as a result of bunch coupling via EC and called "Ohmi effect". This was a significant step in understanding the nature of EC phenomena.

In 1998 when experimenting in SPS with LHC-type test beam emittance growth and coupled bunch instability were observed both attributed to EC influence – [77]. The beam losses have been explained by exciting of couple-bunch motion in the horizontal plane and of single-bunch instabilities in the vertical plane.

Indirect information about EC properties can be deduced from BPMs and vacuum pressure valves measurements. Much more precise are the direct measurements by means of dedicated electron flux detectors.

Several computer codes that simulate the EC build-up and various EC effects have been written. The first EC simulation program PEI was written by K. Ohmi – [76]. The code POSINST was written by M. Furman at LBNL – [78]. The code CSEC was created at BNL by M. Blackiewicz – [79]. At CERN the EC simulation code ELOUD was created by many authors – [80].

Generally speaking EC has a negative influence on the beam quality. Whether or not EC degrades the beam depends on a great number of factors. The main EC-induced effects are:

- The electrons striking the vacuum chamber walls desorb gas molecules and cause a pressure rise. This effect reduces the beam lifetime. It could lead to vacuum pressure instability. Runaway vacuum pressure has been reported in ISR, KEKB, PEP-II, SPS working with LHC-type beam and RHIC;
- The electron cloud produces a focusing force for the ions and cause a betatron tune shift and emittance blow-up;
- EC could produce a majority of collective effects as a couple bunch instability due to EC wake fields, fast "head-tail"-type single bunch instability etc. EC-induced beam instabilities were observed in KEK photon factory, KEKB positron (LER) ring, CESR, PEP-II positron (LER) ring, APS working with positron beams and SPS working with LHC-type beam;
- EC can enhance the beam-beam effects in colliders and reduce the collider luminosity;

- Electron bombardment of the chamber walls is a source of heat deposition. This is of great concern in the high energy superconducting accelerators like LHC;
- EC is a source of noise affecting the proper work of the beam diagnostic devices: pickups, wire scanners, profile monitors etc.

In 2001-2003, during the gold-gold operation of RHIC, a vacuum pressure rise in the warm strait sections was indicated – [81, 82]. This type of pressure rise happens at injection. It is very sensitive to bunch intensity and to bunch spacing. In 55 bunch operation mode the maximum intensity that could be reached was  $8 \cdot 10^8$  ions per bunch. The pressure rise at injection doesn't allow RHIC to work in 110 bunch mode. It is EC that cause the injection pressure rise. This has been proved by simultaneous measurement of EC density and vacuum pressure. There is clear correlation between the signals from electron detectors and vacuum pressure gauges. Also both signals are significantly reduced when a solenoidal magnetic field is applied.

A second type of pressure rise was indicated at transition energy during RHIC deuteron-gold operation. This pressure rise is not sensitive to bunch intensity and spacing. It takes more than ten hours to recover from this pressure instability which indicates that a great amount of gas molecules is desorbed. It has been suggested that the transition pressure rise is due to beam halo scraping of the chamber walls.

The following cures against EC effect could be applied:

- Applying weak solenoidal magnetic fields keeps the secondary electrons near the vacuum chamber walls and thus suppresses the EC build-up. This works in field-free regions and was applied successfully in KEKB and PEP-II positron rings;
- Reducing of secondary electron yield (SEY) by means of electron irradiation of chamber walls. This is due to the removing of oxide layers. A  $N_2$  glow discharge treatment can be used also for this purpose;
- SEY can be reduced also by covering the chamber walls by TiN films or by non evaporating getters (TiZrV). This is used in PEP-II were TiN coating of AL vacuum chamber is applied and also in PSR and LHC;
- The value of the photoelectron yield can be reduced by use of antechambers, which absorbs most of the SR photons (PEP-II). In LHC a saw tooth chamber walls are used to minimize the photon reflection;
- The threshold of EC-induced instabilities can be increased by applying a large chromaticity (BEPC, SPS working with LHC-type beam, KEKB), by the use of Landau damping quadrupoles (KEK photon factory) and by optimizing the bunch length.

### 1.2.5. Processes in Nuclear Interactions of Ultra-Relativistic Heavy Ions

The Large Hadron Collider (LHC) in CERN works either as proton or ion collider. In the so-called lead program LHC will collide  $^{208}\text{Pb}^{82+}$  beams at maximum energy 2.75 TeV/u with peak luminosity  $I = 1 \cdot 10^{27} \text{ cm}^{-2} \cdot \text{s}^{-1}$ .

During the design works on LHC as a led ion collider it was realized that the collisions of high energy ions are source of secondary beams of ions with charge states and mass numbers that differ from reference values – [64]. These secondary ion beams are originated in the interaction points and further they are bent by the magnetic structure in a wrong way and finally hit one of the downstream superconducting magnets – Fig. 43. This concentrated source of hit may lead to a quench.

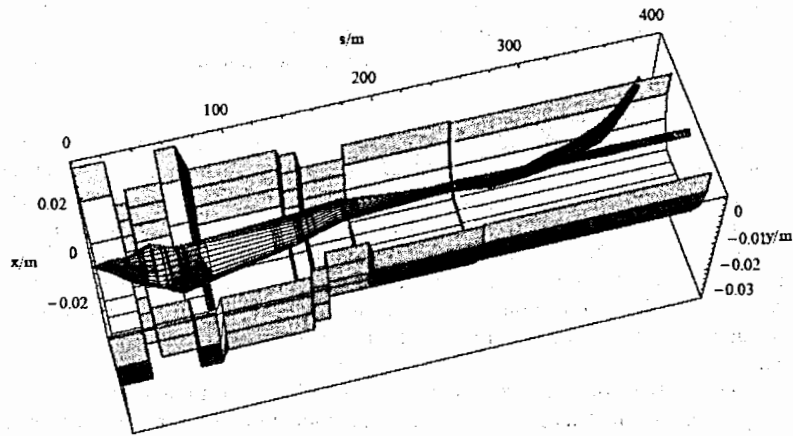
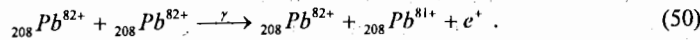


Fig. 43. Main beam of  ${}_{208}\text{Pb}^{82+}$  ions and the secondary beam of  ${}_{208}\text{Pb}^{81+}$  ions emerging from IP2 of the LHC as a lead ion collider – [64]

The strong chromatic effect caused by the low- $\beta$  quadrupoles makes the secondary beam dynamics complicated. Detailed tracking calculations with 3-D codes are necessary – [83].

For heavy ions with  $Z_{pr} \geq 30$  two electromagnetic interactions are considered as very dangerous because they change the charge state or mass of the colliding ions.

A. **Electron capture from pair production (ECPP).** This process consists in production of  $e^+e^-$  pair and a subsequent capture of the electron by one of the colliding nuclei:

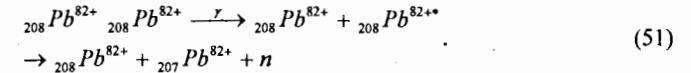


The detailed theoretical estimations give for the cross section the value:  $\sigma_{ECPP} \approx 281$  barn – [84].

The quench limit for heavy ions with energy per nucleon  $T_n$  is equal to that for protons with kinetic energy  $T = T_n$  divided by the mass number  $A$ . In LHC this quench limit for Pb ions is  $8 \cdot 10^4$  Pb/m/s. On the other hand the flux of secondary  ${}_{208}\text{Pb}^{81+}$  ions can be derived from the collider luminosity. For  $L = 1 \cdot 10^{27} \text{ cm}^{-2} \cdot \text{s}^{-1}$  the flux of  ${}_{208}\text{Pb}^{81+}$  ions is  $2 \cdot 10^5$  Pb/m/s, i.e. twice the quench limit – the ECPP effect could be very dangerous. It is considered as one of the main luminosity limiting factors in LHC lead ion collider.

The heavy ion collider RHIC in BNL seems luckier. RHIC collides fully stripped gold nuclei at 100 GeV/u energy. When the main beam consists of  ${}_{179}\text{Au}^{79+}$  ions the secondary beam created in ECPP effect will consist of  ${}_{179}\text{Au}^{78+}$  ions. Fortunately  ${}_{179}\text{Au}^{78+}$  ions still lie within the RHIC momentum aperture. Therefore  ${}_{179}\text{Au}^{78+}$  ions are lost gradually and don't hit the accelerator at a localized spot. For that reason in RHIC the deposited by the secondary beam energy don't cause any problems.

B. **Electromagnetic dissociation (EMD).** This is a two stages process. In the first stage the lead nucleus is excited. In the second stage it decays via neutron emission:



Computer simulations estimate the EMD cross section at LHC lead beam energy as:  $\sigma_{EMD} \approx 104$  barn – [85].

To cope with these adverse effects special collimators must be placed in points where the main and the secondary beams are well separated.

## Part II. ACCELERATOR SYSTEMS

### II.1. MAGNETIC LATTICE

The magnetic lattice of a circular accelerator has two important functions – [86]. On one hand it must bend the particles to follow the closed reference orbit. On the other hand it must focus the accelerated particles toward the reference orbit, forcing them to move in close vicinity of the orbit and thus preventing particle losses.

The magnetic configuration of an accelerator has to be as simple as possible. For this reason it usually is a concatenation of some number of identical cells. This makes the structure less sensitive to construction errors, facilitates the machine operation and significantly reduces the price. The optical properties of the beam repeat in each cell, which facilitates the accelerator design. The cell optics must satisfy the closure condition – the values of the amplitude (Twiss) functions  $\beta_{h/v}(s)$  and its derivative  $\beta'_{h/v}(s)$  and the values of dispersions  $D_{h/v}(s)$  and its derivative  $D'_{h/v}(s)$  at the two ends of each cell must be equal. When this matching condition is fulfilled, we can link the cells together not changing the focusing properties.

Nowadays the separated function lattice design is a preferred choice. Each cell consists of dipole magnets with uniform field (zero field gradient) and of focusing quadrupole lenses. This makes the optical elements easy to manufacture and allow increasing the bending fields and the repetition rates. The separate function lattice is also more flexible in operation.

The lattice design of high energy heavy ion accelerators follows in general that of hadron accelerators. The fact that the accelerated particles are heavy ions however imposes some constraints and demands for some specific solutions.

The main challenge comes from the intrabeam scattering. The IBS cross-section is proportional to  $\frac{Z^4}{A^2}$  and as for heavy ions the ratio  $\frac{Z^4}{A^2}$  is large a lattice with shorter and strongly focusing cells will be necessary. A solution with many cells and large phase shift per cell will minimize the IBS diffusion rate, see (40).

The FODO lattice structure is most frequently used. This simplest arrangement consists of an alternation of focusing and defocusing quadrupoles, with equal strength, and bending magnets between them.

An example of FODO lattice is the RHIC arc structure – Fig. 44. The heavy ion collider RHIC represents an accelerator, a storage ring and a collider – [87]. It works with a variety of ion species from  $A/Z=1$  (protons) to  $A/Z=2.5$  (gold ions). Ion  $\text{Au}^{79+}$  is chosen to be the design ion. The maximum energy is in the range of 30-100 GeV/u.

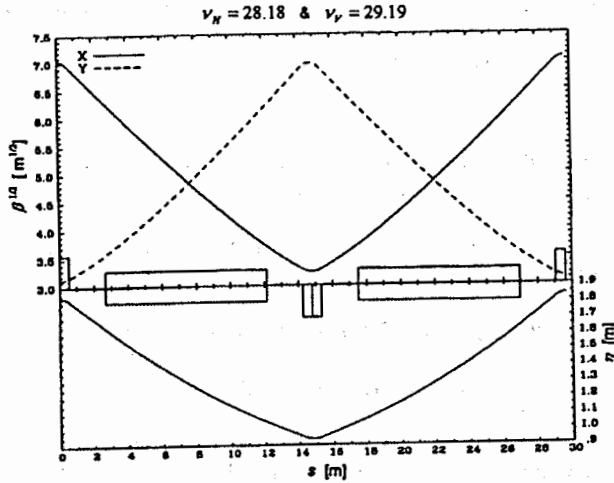


Fig. 44. The amplitude  $\beta$ -functions and dispersion in a RHIC arc cell – [87]

Each of the two RHIC rings consists of six arcs and six insertions. Every arc comprises 12 FODO cells.

The optical properties of a FODO cell are parameterized by the phase advance  $\mu$  per cell – Fig. 45. For  $\mu$  in the range from  $60^\circ$  to  $90^\circ$  the maximum value of amplitude function  $\beta_0$  depends only on the cell length  $L$ . The optimum phase advance per cell is  $76.35^\circ$ .

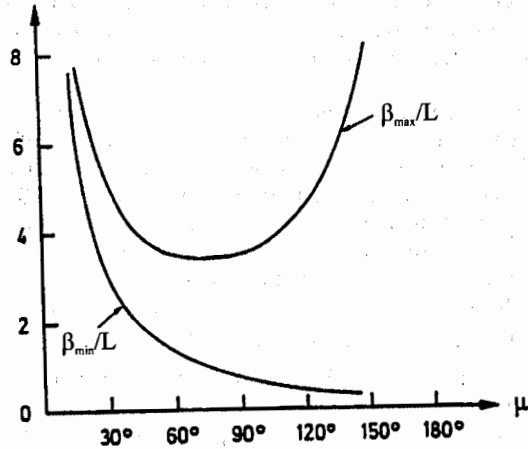


Fig. 45. Dependence of maximum and minimum values of Twiss  $\beta$ -function on the phase advance per cell  $\mu$  for a FODO lattice

In thin approximation:

$$\beta_{max/min} = \frac{(1 \pm \sin \frac{\mu}{2})L}{\sin \mu} \quad (52)$$

It follows from (52) that the minimum of the sum ( $\beta_{max} + \beta_{min}$ ) is reached for  $\mu=90^\circ$ . For Au ions at 30 GeV/u after ten hours of storage in RHIC the normalized transverse emittance and the momentum spread grow due to IBS to  $34\pi$  mm.mrad and  $\pm 5 \cdot 10^{-3}$  respectively.

To minimize the effect of IBS the FODO cells in RHIC are shorter and stronger. The phase advance per cell is close to  $\pi/2$  ( $\mu_h=82.42^\circ$  and  $\mu_v=87.25^\circ$  for  $\beta^*=1$  m). The horizontal  $6\sigma$  beam size taking into account the IBS is estimated to be  $\pm 27$  mm. The RHIC cold bore beam tube aperture is chosen to be 69 mm.

In RHIC lattice design the IBS phenomenon is of main concern. In an attempt to cope with it the specialists from BNL have developed the concept of transverse IBS suppression. This concept is valid for energies that are much higher than the transition energy. In high energy approximation the following relation between the transverse and longitudinal diffusion exists:

$$\frac{d\epsilon_x}{ds} = H(s) \frac{d\delta_x^2}{ds}, \quad (53)$$

where  $H(s)$  is the so-called dispersion H-function:

$$H(s) = \gamma_x D_x^2 + 2\alpha_x D_x D'_x + \beta_x D_x'^2. \quad (54)$$

It follows from (53) that minimizing the H-function will reduce the transverse IBS growth rate.  $H(s)$  could be reduced increasing the horizontal tune advance per FODO cell. For example in smooth lattice approximation  $H \sim 1/Q_x^3$ .

For RHIC if the horizontal phase advance per FODO cell is increased from  $82^\circ$  to  $107^\circ$  the value of H-function and therefore the transverse growth rate will be reduced by a factor of 2. This was verified by both computer simulations and accelerator experiments.

Another specific for heavy ions phenomenon that could influence the lattice design is the dynamic vacuum effect. It is of importance when the accelerated ions are not fully stripped. Ions with intermediate charge have large cross sections for losing an electron in interactions with the molecules of the residual gas. The cross sections for electron capture are much smaller.

Accelerating ions with intermediate charge instead of bare nuclei will relieve the space charge problems and will allow for higher intensity to be achieved.

As it was described in Chapter 2.2 of Part 1 when the circulating ion loses an electron it jumps to a new charge state and to a new trajectory. Such ions will hit the inner side of the beam pipe. This happens usually behind dipoles – Fig. 46. Hitting the pipe the heavy ion will release the absorbed in it gases. The desorption rate could be very high ( $\sim 10^4$ ) and pressure bumps of several orders of magnitude in a few  $\mu$ s have been observed.

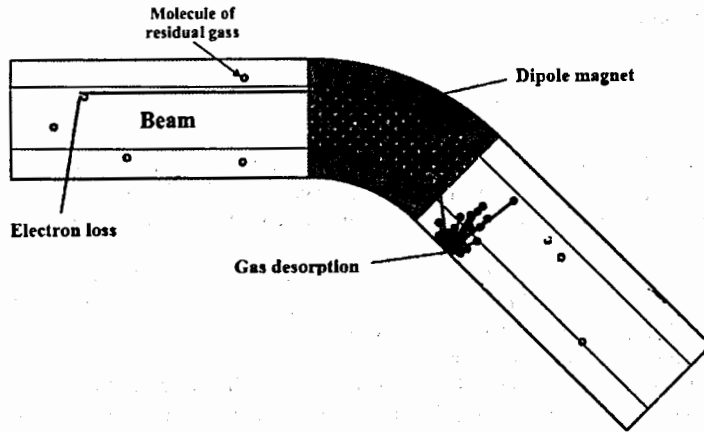


Fig. 46. Gas desorption due to the charge exchange beam losses

The minimization of dynamic vacuum effect requires lattice that acts as a charge separator. Such lattice will separate the ions that have lost an electron from the circulating beam. A special collimation system will localize the beam losses at dedicated catchers with low desorption rate and the released gases will be confined in a secondary vacuum chamber with high pumping power. It is important to prevent the desorbed gases from reaching the circulating particles.

Catcher system for charge exchange beam losses will be installed in the SIS-100 synchrotron and in the upgraded SIS-18 synchrotron of the FAIR complex at GSI – [88]. The upgraded SIS-18 synchrotron is also known as SIS 12/18 because as a booster synchrotron for the SIS-100 synchrotron it will work at maximum beam rigidity of 12 T·m. The design ion in both machines is  $U^{28+}$ .

In SIS-100 the catcher modules will be installed inside the quadrupole cryostat. The secondary vacuum chamber is at temperature of 5 K and is used as a cryopump for the desorbed gases.

It was shown that only doublet type lattice with order (BM, BM, D, F) will be able to provide about 100% collimation efficiency – Fig.47 – [89]. The lattice has large horizontal and vertical acceptances. It leaves enough free space for installing additional equipment.

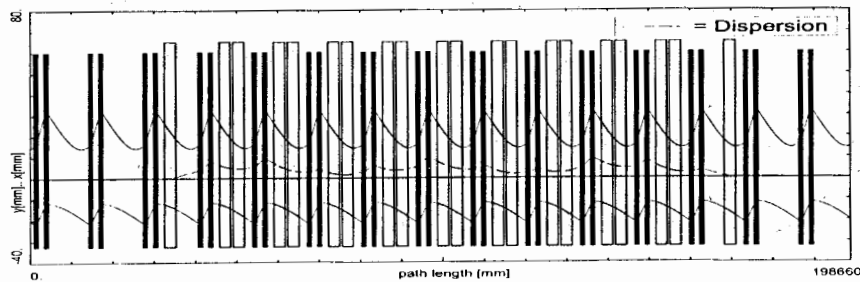


Fig. 47. The doublet lattice structure of SIS-100 synchrotron with missing dipoles at both sides of the arcs and minimized dispersion – [89]

A very small dispersion in the straight sections will be achieved by the missing magnet approach. For this the first and the last cells of arcs will use not two but one dipole.

In SIS-100 the catchers will consist of two copper wedges coated with a thin gold layer. For gold surfaces a desorption rate as low as 25-80 molecules/ion could be achieved.

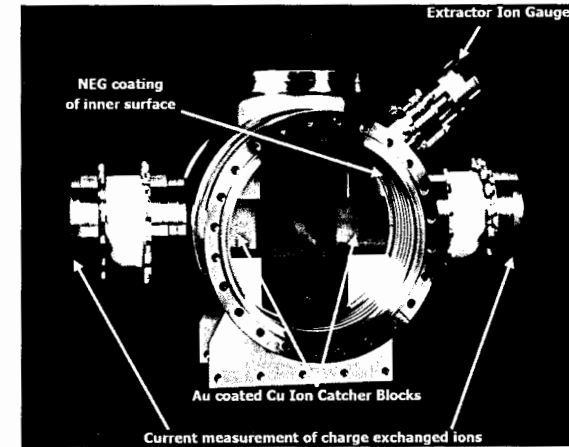


Fig. 48. SIS-18 collimator system

In the upgraded SIS-18 synchrotron each section of the accelerator will be equipped with a catcher module – Fig. 48. The SIS-18 collimator system controls and confines desorption gases where they are produced. The absorbers are from Cu, coated by Au. The secondary chamber provides for as much pumping speed as possible. Simulations and experiments show that only 7% of the desorbed gases will leave the secondary chamber.

The design of the SIS-18 lattice is unique – [90, 91]. This synchrotron utilizes multiturn injection of ions with stacking in the horizontal phase space. To increase the number of the injected turns one needs small emittance of the injected beam and large horizontal acceptance of the circular accelerator. In SIS-18 the horizontal acceptance is  $A_h = 200 \pi \text{ mm} \cdot \text{mrad}$ . This large acceptance is obtained applying triplet focusing. For fixed aperture of the magnets the triplet lattice has largest transverse acceptances.

On the other hand during acceleration the beam shrinks transversely due to the adiabatic damping of the betatron oscillations. At the end of the ramp the large acceptance is no more needed.

The beam extraction is more efficient if the accelerator has large  $\beta$ -functions and if they differ significantly in both transverse planes. Such behavior of the amplitude functions is typical for doublet focusing. In addition zero dispersion at the extraction septum will allow to eject short bunches with large momentum spread (1%).

In order to have optimum lattice both at injection and at maximum energy in SIS-18 the focusing changes during the acceleration from triplet to doublet structure – Fig. 49.

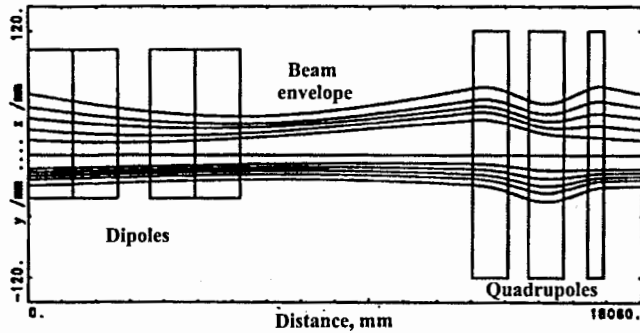


Fig. 49. Transition from triplet to doublet magnetic lattice in SIS-18 – [91]

The dynamic change of the lattice type during the ramp makes SIS-18 unique machine. The transition from triplet to doublet focusing is done by keeping one of the quadrupoles of the triplet fixed at injection level. The other two quadrupoles are programmed in a way to keep the betatron tune constant.

The SIS-18 optics has also the feature of changing the accelerator symmetry from  $S=12$  identical cells to  $S=6$ . The change of machine symmetry raises the transition energy beyond the maximum proton energy.

The injection energy into synchrotrons must be as high as possible. The rule accepted in the accelerator practice states that the ratio of the injection energy to the maximum energy must be  $T_{inj} : T_{max} \leq 1 : 100$ . This rule is valid not only for proton machines but for heavy ion synchrotrons as well.

In synchrotrons big acceptance is needed at injection when the beam size is large. This large beam size determines magnet aperture and the volume in which magnetic field must be excited. On the other hand at maximum energy the beam size is much smaller due to the adiabatic damping of the betatron oscillations but one cannot squeeze the accelerator aperture following the beam size. The magnetic field still must be excited in the same large volume.

What are the advantages of having high injection energy?

Increasing the injection energy will alleviate the adverse space charge effects. The incoherent betatron tune shift  $\Delta Q$  due to the space charge forces is proportional to  $\beta^2 \gamma^3$ ,  $\beta$  and  $\gamma$  being the relativistic factors. A boundary value of  $\Delta Q=0.1$  or even  $\Delta Q=0.05$  is usually adopted. Although this limit could be increased to  $\Delta Q=0.3$  on the expense of very precise correction of the crossed resonances as a rule in synchrotrons to get higher intensity you must use higher injection energy. According to the Lasslett formula the space charge limit is given by:

$$N = \frac{\pi(\epsilon_V + \sqrt{\epsilon_H \epsilon_V})\beta^2 \gamma^3 B_f \Delta Q}{r_i}, \quad (55)$$

where  $B_f$  is bunching factor (usually taken as 0.5) and  $r_i$  is the classical ion radius:

$$r_i = \frac{Z^2}{A} r_p, \quad (56)$$

$r_p = 1.54 \cdot 10^{-18}$  m being the classical radius of the proton.

As a linear injector for relatively high energy is expensive the choice usually falls on a small circular injector, the so-called booster.

According to (55) the space charge limit does not depend on the machine circumference. This allows to raise the linear charge density in the booster, to fill the main machine with several booster cycles and thus to increase the main machine intensity.

In the booster much larger acceptance could be used and an efficient multiturn injection scheme could be adopted.

Other advantages of boosters are:

- The booster can have high repetition rate;
- It is easier to maintain a high vacuum in the booster than in the main machine due to its small size;
- When the accelerated particles are heavy ions you could apply ion stripping at the booster exit. Due to the higher injection energy the stripping will be efficient. Thus you will raise the energy of the main machine.

The lattice design of the circular injectors-boosters is influenced by the nature of heavy ion projectiles as well.

For example in the CERN accelerator complex for acceleration of heavy ions and for realizing of ion collisions at LHC collider the upgraded ring LEAR is used as a booster – [92,93]. This is the so-called LHC led program as the reference ion was chosen to be  $^{208}\text{Pb}^{82+}$ .

In the past LEAR was used as antiproton storage ring. Because now this ring will accumulate and accelerate ions it received a new name – LEIR (Low Energy Ion Ring). LEIR inherits a square shape from LEAR. For ion accumulation LEIR applies a new combined multiturn injection method with stacking in both horizontal and vertical phase spaces and in the longitudinal phase space. This new injection method requires that the normalized dispersion  $D/\sqrt{\beta}$  at the injection septum is large. LEIR uses fast electron cooling of the ion beam at injection energy. In the cooler the electron beam must overlap the ion beam. To realize this zero dispersion at the cooler section is needed. The electron cooling is used both for improving the beam quality and for raising the beam intensity through repeating injection-cooling cycles. To meet all these requirements quadrupole triplets at the cooling section and quadrupole doublets at the injection section are used.

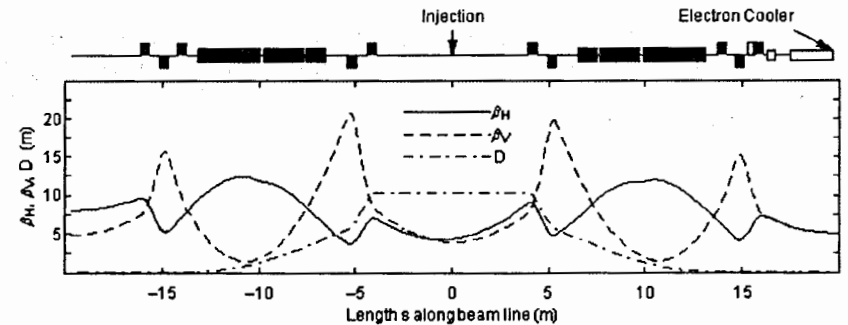


Fig. 50. LEIR lattice functions – [92]

This arrangement provides the necessary large normalized dispersion  $D^* = 5$  m at the injection septum and zero dispersion at the cooler. The LEIR lattice functions are shown on Fig. 50.

The vacuum level in LEIR is very high ( $5 \cdot 10^{-12}$  Torr). Hence the cross sections for electron loss or capture by accelerated Pb ions are small. Nevertheless the charge exchange reactions with the residual gas molecules still could produce enough number of lost ions and lead to dangerous outgazing from the vacuum pipe walls. As in SIS-18 and SIS-100 to cope with beam induced vacuum degradation in LEIR a dedicated collimation system is used to intercept the lost ions. The collimators are made of stainless steel coated with  $30 \mu\text{m}$  gold layers. It was shown that gold have low outgazing yield. Other measures against dynamic vacuum effect applied in LEIR is baking to  $300^\circ\text{C}$  of the vacuum chamber and scribbling of it by ion beam to remove the absorbed gases.

Besides guiding particles you have to inject them into the machine from an external linear accelerator or booster, to eject them towards the experimental setup and to accelerate them by means of RF cavities. In colliders you make the counter rotating beams meet each other head on in several points around the ring. All these manipulations need additional equipment and you have to find a free space for this equipment in the lattice. This is not easy task and often a compromise is needed. Usually one simply takes off some of the bending magnets converting the corresponding curvilinear structural periods to straight sections.

The straight sections could be either symmetric or anti-symmetric. In symmetric straight sections  $\alpha_x = \alpha_y = D_x' = 0$  at the center of the section,  $\beta_x, \beta_y$  have a minimum at this point and the phase advances  $\mu_x, \mu_y$  are different. In anti-symmetric sections at the section center  $\beta_x = \beta_y$  and  $\mu_x = \mu_y$ . There are many reasons to make at least some of the special sections dispersion free – [94]. In order not to influence the chromaticity the sextupole lenses that excite a third order resonance in the slow extraction method must be placed in dispersion free regions. RF cavities also should be placed at dispersion free regions otherwise the longitudinal and transverse motions become coupled.

Here are two examples.

The new synchrotron SIS-100 at GSI will have six large straight sections for installing the equipment for beam injection, acceleration and extraction. The optics of the accelerator could be tuned in a way to generate either zero or sufficient dispersion in the straight sections. The zero dispersion is necessary for the fast extraction of bunches with large momentum spread (up to 1%). A large dispersion will allow fulfilling the Hardt condition of the slow extraction.

In colliders zero dispersion must be provided at the interaction point. In RHIC the dispersion suppressor consists of five half-cells with reduced bendings (Q10 to Q5 in Fig. 94). Matching of dispersion between the arcs and the insertions is done by means of four quadrupoles (Q6-Q9 in Fig. 94).

## II.2. INJECTION

The goal of any injection systems is to accumulate high current beams with minimum particle losses. The accelerator acceptance has to be filled with particles as dense as possible.

Many methods developed for injection of protons after a proper modification could be applied for accumulation of heavy ions. As the intensity of the heavy ion beams produced by the existing ion sources, especially of those in high charge states, are limited and as a rule several orders of magnitude lower than the intensity of proton beams, the methods for multiturn injection are of big importance for ion storage. Methods for particle stacking in either betatron phase space or synchrotron phase space or simultaneously in both have been developed.

The significant progress made by beam cooling technics has provided the possibility to combine the multiturn injection with beam cooling. Repeating several stacking-cooling cycles one could increase the intensity of accumulated ions to great extent.

Recently new type of broadband RF systems, the so-called Barrier Bucket (BB) RF systems, have found applications for beam manipulation in the longitudinal phase space. With the simultaneous use of BB system and beam cooling a large number of bunches could be injected and accumulated into a storage rings.

### II.2.1. Single-Turn Injection

In single-turn injection the beam is put on the reference orbit by means of a septum unit (septum magnet or electrostatic wire septum) and a fast kicker magnet – [95].

The single-turn injection is most frequently used for bunch-to-bucket transfer from a booster synchrotron to the main ring.

For example at the BNL accelerator complex six bunches with  $\text{Au}^{32+}$  ions from the Booster are striped to  $\text{Au}^{77+}$  and then injected into the AGS synchrotron via a box-car stacking. Four Booster cycles are needed to fill the whole AGS circumference. The two rings of the superconducting heavy ion collider RHIC are filled by means of bunch-to-bucket transfer as well. Fourteen repeated AGS cycles are used to populate sixty RF buckets in RHIC (four of them remaining empty).

The superconducting heavy ion synchrotron Nuclotron at JINR-Dubna uses electron beam ion source. As the EBIS pulse duration is short and compared with the revolution time in the Nuclotron ring the single-turn injection is a natural choice – [96]. The Nuclotron injection is realized with the help of a superconducting septum magnet (SM) and kick electric plates (EP) – Fig. 51.

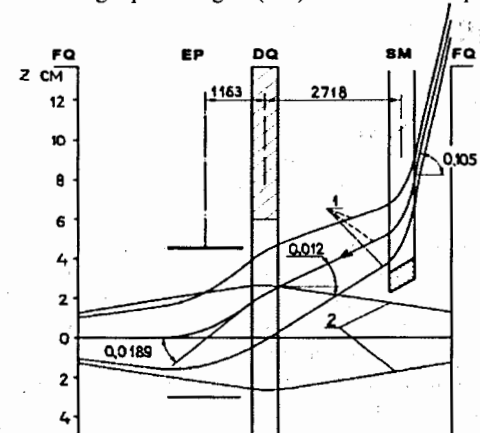


Fig. 51. Single-turn injection into Nuclotron: 1 – injected beam, 2 – circulating beam – [96]

The septum deflects the injected beam into the closed orbit at the center of the kicker. After that the kicker bends the ions and directs them along the orbit.

### II.2.2. Multiturn Injection with Betatron Stacking

The classical method of multiturn injection with accumulation of particles in the transverse (horizontal) phase plane is widely used in heavy ion synchrotrons and storage rings – [97,98].

The principle of the method consists in a local distortion of the closed orbit by means of four bump magnets – Fig. 52. From the very beginning the bump is as large as to pass close to the septum and then it is gradually reduced to zero following a linear, exponential or other law – [99].

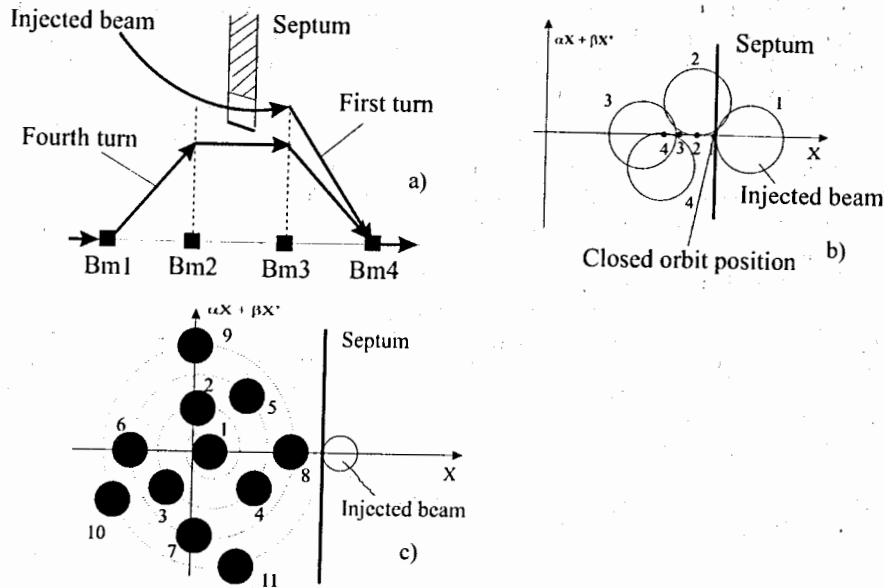


Fig. 52. Principle of the multiturn injection with betatron stacking. a) Four magnets closed orbit bump, b) Successive positions of the one of the injected slices in the horizontal phase space; the fractional part of the betatron tune  $Q$  is equal to 0.25, c) All the injected beam slices lie on a spiral

On the second turn the particles will avoid (partially) the septum due to the betatron oscillations around the instantaneous closed orbit. Meanwhile a new portion of particles is injected. These particles will have larger amplitudes of the betatron oscillations as the orbit bump is reduced. It could be shown that the successive slices of the injected beam lie on a spiral in the horizontal phase space. The origin of the spiral is on the simultaneous orbit. This is well seen in the normalized phase plane  $(x, x^*)$ ,  $x^* = \beta x' + \alpha x$ , where  $\alpha$  and  $\beta$  are the Twiss structural functions. In the normalized phase space  $(x, x^*)$  the particle trajectories are circles.

Computer simulations can describe the stacking process step by step – [100, 101]. An example is shown on Fig. 53. These are computer simulations of multiturn injection into one of the projects of Nuclotron booster – [101]. This was a fast cycling synchrotron with a circumference equal to one third of the Nuclotron circumference and capable to accelerate ions with  $Z/A=0.5$  up to 250 MeV/u.

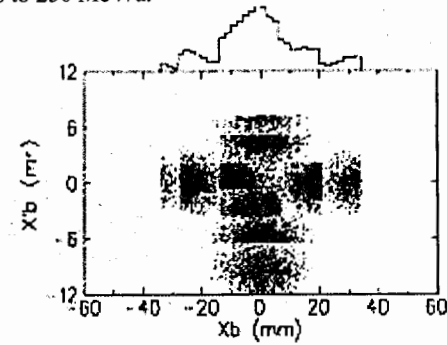


Fig. 53. Phase portrait of fifteen-turns injection (computer code ACCSIM) – [101]

Two definitions of the injection efficiency are used.

The first is:

$$\epsilon_1 = \frac{N_{st}}{n_{\Sigma} N_{inj}} = \frac{n_{eff}}{n_{\Sigma}}, \quad (57)$$

where  $N_{st}$  is the full number of stored particles,  $N_{inj}$  – the number of particles injected per turn,  $n_{\Sigma}$  – the total number of injected turns and  $n_{eff}$  – the number of effective turns.

The second definition of the injection efficiency is especially suited for the stacking in the transverse phase plane.

It is related with the definition of the accumulation factor (AF):

$$AF = \frac{I_{accelerator}}{I_{injector}}. \quad (58)$$

Now we will define the efficiency of the multiturn injection as:

$$\epsilon_2 = \frac{AF}{A_x/\epsilon_x}, \quad (59)$$

where  $A_x$  is the horizontal acceptance of the accelerator and  $\epsilon_x$  – the horizontal emittance.

The stacking efficiency depends on large number of parameters: the distance injected beam centre - septum, the slope of the injection beam, the number of injection periods (injection time), the number of betatron oscillations per turn, the injector emittance, the momentum spread in the injected beam, etc.

An example of multiturn injection with stacking in horizontal phase space is the injection in SIS-18 – [102,103].

The linear injector is UNILAC which delivers ion currents of several mA in a macropulses with length from 500  $\mu$ s to 5 ms. SIS-18 uses four bump magnets for local closed orbit distortion and an electrostatic wire septum. The injected emittances are  $5\pi$  mm.mrad both in horizontal and vertical phase spaces. The SIS-18 horizontal acceptance is 200  $\pi$  mm.mrad. The ratio  $A_x/\epsilon_x$  is equal to 40. The UNILAC with the high intensity Chordis ion source can provide for example 2.2 mA  $Ne^{10+}$  ion beam. A total beam current of 35 mA or  $N_i=1 \times 10^{11}$  neon ions is accumulated during 22 turns multiturn injection – [103]. This means efficiency  $\epsilon_1=0.7$  or about 16 effective turns. The multiturn

injection process is shown on Fig. 54. From Fig. 54 one could see that about 20% beam losses were measured.

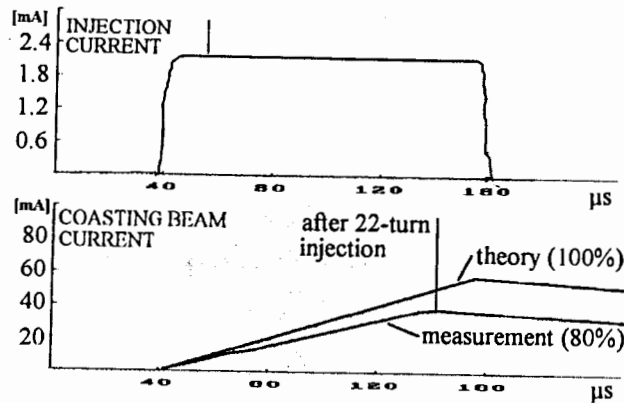


Fig. 54. Multiturn injection of  $1 \times 10^{11} \text{ Ne}^{10+}$  ions into SIS-18 – [103]

### II.2.3. Multiturn Injection with Stacking in both Horizontal and Vertical Phase Spaces

If both the horizontal and the vertical emittances of the injected beam are sufficiently smaller than the acceptance of the ring, one can realize multiturn injection with stacking in both horizontal and vertical phase spaces applying linear coupling of the betatron oscillations [104, 105].

The linear coupling occurs in the presence of skew quadrupole or solenoidal magnetic fields. The strength of the coupling if excited by skew quadrupole is determined by [106]:

$$C_q = \frac{R}{2\pi Q} \frac{1}{B\rho} \oint \left( \frac{dB_x}{dx} \right)_{z=0} ds, \quad (60)$$

where  $R$  is the mean radius of the accelerator,  $B\rho$  is the beam rigidity and  $Q$ -betatron tune.

The linear coupling leads to beating of the horizontal and the vertical betatron oscillations. The amplitudes of the oscillations in smooth approximation are:

$$\begin{aligned} |X|^2 &= |A|^2 + |B|^2 \chi^2 - 2|AB^*| \chi \cos(Q_c \theta), \\ |Z|^2 &= |B|^2 + |A|^2 \chi^2 + 2|AB^*| \chi \cos(Q_c \theta), \end{aligned} \quad (61)$$

where:

$$\chi = \sqrt{1 + \zeta^2} - \zeta, \quad (62)$$

$$\zeta = \frac{B\rho Q \Delta}{R^2 \left( \frac{dB_x}{dx} \right)}, \quad (63)$$

$$\Delta = Q_x - Q_z, \quad (64)$$

$$Q = \frac{Q_x + Q_z}{2}. \quad (65)$$

In (61)  $A$  and  $B$  are two complex constants of the motion whose values are determined by the initial conditions and  $Q_c$  is the beating wave number.

It can be shown that:

$$Q_c = \sqrt{\Delta^2 + C_q^2}. \quad (66)$$

According to (61) there exists a sinusoidal exchange of energy from the horizontal to the vertical betatron oscillations and vice versa while the whole energy, i.e.  $|X|^2 + |Z|^2$  keeps constant.

Thus a beam injected in the medium plane close to the vacuum chamber wall will undergo horizontal betatron oscillations with decreasing amplitude. The energy of the horizontal oscillations goes to excite vertical betatron oscillations with increasing amplitude. After a half of beating period the beam will be dismissed towards the machine center and vertically off the median plane to the highest degree.

The depth of the amplitude modulation during beating is given by:

$$S = \frac{C_q}{\Delta^2 + C_q^2}. \quad (67)$$

After that the process will go back to small vertical and maximum horizontal amplitudes of oscillations that is why the injection process must be stopped. As a result we will have phase space painting in both horizontal and vertical planes.

The multiturn injection of heavy ions with linear coupling is realized for instance in the AGS booster – [107]. The injection is from 1 MeV/u tandem Van de Graaff which delivers ion beams with very small transverse emittance ( $1\pi \text{ mm-mrad}$ ). This allows very efficient multiturn injection – Fig. 55. The unperturbed tunes are  $Q_x = 4.833$  and  $Q_z = 4.780$ . A skew quadrupole induces significant X-Z coupling during the injection. Typically about 40 turns can be injected with an efficiency of 65%. Applying this scheme the beam intensity has been increased with more than 50%.

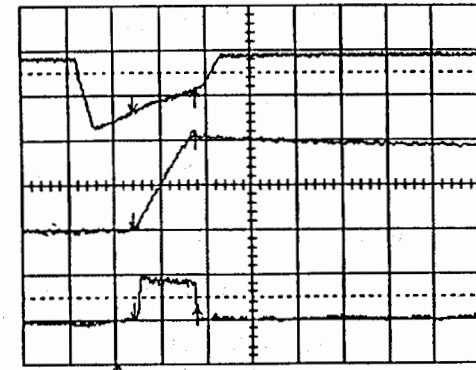


Fig. 55. Multiturn injection in the AGS booster. Oscilloscope traces of the injection kicker (top), circulating beam current (middle) and beam pulse from the Tandem (bottom) are shown. One horizontal box corresponds to 500  $\mu\text{s}$  – [107]

### II.2.4. Beam Stacking with RF Acceleration

#### II.2.4.1. Principle of RF Stacking

Storage of the injected particles in the longitudinal phase space was first suggested by Symon and Sessler in MURA [108]. Later this method was experimentally investigated in the model electron storage ring CESAR in CERN [109]. The RF stacking was used successfully for many years in the proton storage ring ISR in CERN [110].

The principle of the RF stacking [108 – 112] can be understood from Fig. 56, where a transverse cross section of the accelerator is shown. The beam is injected by means of an kicker magnet at position  $X_{inj}$ . By means of an movable eddy current shield (shutter) which is

raised during injection the open gap of the kicker is closed and the magnetic field is restricted only to its aperture. Another approach for reducing of the stray field at the stack region is the use of C-chapped ferrite yoke opposite to the kicker magnet, which absorbs the major part of the stray field. This approach is applied in ESR ion ring at GSI. After the injection of the first portion of particles is completed, the stacking RF cavity is switched on and the particles are accelerated (or more usually decelerated) to an outer (inner) orbit following the relation

$$\frac{E}{R} \frac{dR}{dE} = \frac{\alpha}{\beta^2}, \quad (68)$$

where  $\beta$  is the relativistic factor and  $\alpha$  is the momentum compaction factor [113, 114]:

$$\alpha = \frac{p}{R} \frac{dR}{dp} = \frac{\langle D_x \rangle_m}{R}. \quad (69)$$

In (69)  $\langle \rangle_m$  denotes averaging over the dipoles only and  $D_x$  is the dispersion.

When the top of the stack is reached, the RF voltage is abruptly switched off and the particles are released from the RF buckets.

The RF cycle then is repeated and the next injected portion is trapped in buckets and accelerated (decelerated).

There are two modes of operation.

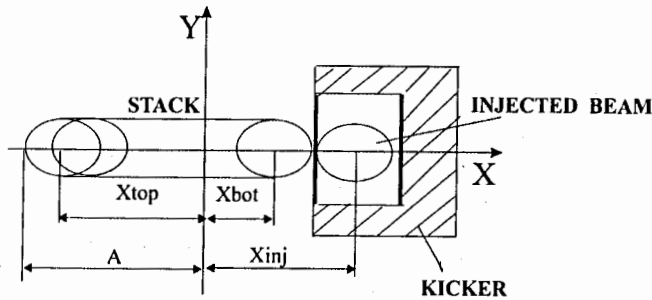


Fig. 56. Location of the injected and stacked beams in the accelerator aperture

In the so-called "repetitive stacking" mode or "stacking at the top" the new portion is moved again to the same position, i.e., to the top of the stack. According to Liouville's theorem the particle density in the longitudinal phase space must be conserved [114]. Hence the particles already accumulated in the stack will be displaced toward lower (higher) energies. Due to the very small value of the momentum compaction factor (69) in the strong focusing rings the portions of particles with different energies largely overlap in the physical and transverse phase spaces – Fig. 57. The stacking takes place in the longitudinal phase space while the density in the 6-dimensional  $\mu$ -phase space is conserved in agreement with Liouville's theorem. A beam stack with large intensity is built up.

In the "non-repetitive stacking" mode or "stacking at the bottom" each successive portion of particles is moved to a slightly different energy than the previous one. The energy difference is equal to the final bucket area  $A_b$  divided by  $2\pi$ . Thus the new particles will be added to the bottom of the stack.

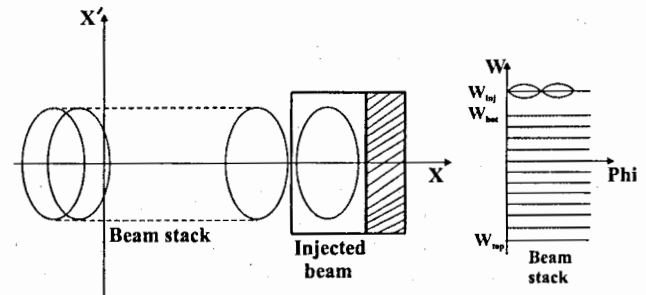


Fig. 57. Principle of RF stacking

#### II.2.4.2. Longitudinal Phase Space Topology

As this has been shown first by Symon and Sessler [108], the equations of the longitudinal motion in an accelerator can be put in Hamilton's form with canonically conjugated variables:

$$W = 2\pi \int_{E_0}^E \frac{dE}{\omega(E)} \quad (70)$$

and the RF phase  $\varphi$ . In (70)  $\omega(E)$  is the revolution frequency of a particle with energy  $E$  and  $E_0$  is an arbitrary energy.

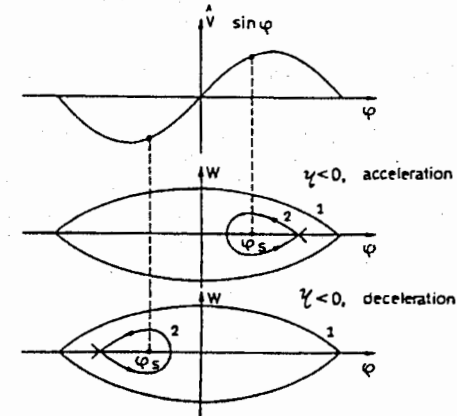


Fig. 58. Stationary and moving RF buckets

The area of stable oscillations around the synchronous particle, the so-called RF bucket is shown on Fig. 58 for the stationary case (no acceleration (deceleration)) and for the moving buckets when the particles are accelerated (decelerated).

Let  $h$  be the harmonic number of the RF, so as we will have  $h$  buckets simultaneously on the accelerator circumference. The area of these  $h$  buckets is:

$$A_{B_s} = \frac{8\beta}{\omega_s} \sqrt{\frac{8\pi e V E_s}{h|\eta|}}, \quad (71)$$

b) for moving buckets

$$A_b = A_{b_s} \alpha^*(\Gamma) . \quad (72)$$

Here:

$$\eta = \frac{p}{\omega} \frac{d\omega}{dp} = \frac{1}{\gamma^2} - \alpha = \frac{1}{\gamma^2} - \frac{1}{\gamma_{tr}^2} , \quad (73)$$

$\gamma$  – the relativistic factor and  $\gamma_{tr}$  – its value at the transition point. In (72)  $\alpha^*(\Gamma)$  is a tabulated function of the synchronous phase  $\Gamma = \sin \varphi_s$ . In the RF stacking an important role is played by the adiabatic theorem of Boltzman-Ehrenfest [114], which states that if the parameters (such as  $V$ ,  $\varphi_s$ ,  $E_s$ , etc.) in the Hamiltonian,  $H$ , are varied sufficiently slowly the particles lying on a closed curve  $H(t_1) = \text{const}$  surrounding an area of stable oscillations  $A_1$  at a time  $t_1$  will remain on a closed curve  $H(t_2) = \text{const}$  surrounding an area  $A_2 = A_1$  at a time  $t_2 > t_1$ . Thus the action integral,  $I = \oint W d\phi$ , is an invariant.

### II.2.4.3. Stacking Cycle

It is the phase displacement phenomenon that underlie the Rf stacking process. The phase displacement is a phenomenon related with the crossing of a coasting beam by RF bucket (no matter filled with particles or empty). The trajectories outside the separatrix are such that the particles will move to the opposite to the bucket direction (for an accelerating bucket to lower energy and for an decelerating bucket to higher energy). According to Liouville's theorem the area of the displacement of the coasting beam must be equal to the bucket area  $A_b$ . Hence the change in the mean energy of the coasting beam is:

$$\Delta W = \frac{A_b}{2\pi} . \quad (74)$$

A detailed calculation of the change of the energy of a particle lying outside a moving bucket when this bucket crosses the particle is made in [115, 116]. It shows that the mean energy change follows (74) while the energy spread in the coasting beam is increased. Let's now look at the RF stacking cycle in more details. The stacking is performed at a constant magnetic field. After the first portion of particles is injected, it immediately debunches due to the spread in the revolution frequency of particles having different energies.

The RF voltage is now switched on adiabatically while the RF frequency is kept constant ( $\varphi_s = 0$ ). The particles are trapped with big efficiency (more than 90%) in stationary buckets. After the capture finishes, the RF buckets are decelerated toward to the top of the stack.

As:

$$\frac{E}{\omega} \frac{d\omega}{dE} = \frac{\eta}{\beta^2} \quad (75)$$

and

$$\frac{dE}{dt} = \frac{\omega}{2\pi} e\hat{V} \sin \varphi_s . \quad (76)$$

the RF frequency must be increased according to:

$$\frac{d\omega_{rf}}{dt} = \frac{\eta \omega_{rf}^2}{2\pi h \beta^2 E} e\hat{V} \sin \varphi_s . \quad (77)$$

When  $\omega_s$  reaches the final frequency, the RF voltage is switched off, the bunches debunch and a whole strip in the stack is populated with particles.

In the repetitive stacking mode each of the successive pulses crosses the whole stack and the particles are released at the top of the stack.

In each crossing the already stored particles are moved to higher energy according to the phase displacement mechanism.

If the stack is built by  $n$  pulses, the ideal stack width will be:

$$2\pi \frac{\Delta E_{ideal}}{\omega} = n \frac{A_b}{2\pi} . \quad (78)$$

In fact the particles will be distributed over wider energy range  $\Delta E_s > \Delta E_{ideal}$ .

In the non-repetitive stacking mode the crossing of the whole stack by the buckets is avoided by successive reducing of the final RF frequency by:

$$\Delta \omega_{rf} = \frac{\omega_{rf}^2 \eta}{\beta^2 E h (2\pi)^2} \frac{A_b}{2\pi} . \quad (79)$$

Thus the particles will be deposited at the stack bottom.

It is natural to define the stacking efficiency as the ratio of the average phase space density in the stack to that in the injected beam [117].

The total stacking efficiency depends on two kinds of parameters:

$$\epsilon_{tot} = \epsilon' \epsilon . \quad (80)$$

Here  $\epsilon'$  describes the dependence of the stacking efficiency on the RF manipulation – mainly on the trapping efficiency in the buckets.

In (80)  $\epsilon$  is the accumulation efficiency itself:

$$\epsilon = \frac{N_{lim}}{N_{tot}} , \quad (81)$$

where  $N_{lim}$  is the number of particles in the ideal stack width and  $N_{tot}$  is the total number of particles in the stack.

Function  $\epsilon$  represents the reduction of the phase space density due to the dilution of the stack by the moving RF buckets during the subsequent stacking cycles.

Experiments and computer simulations [117] show that  $\epsilon$  is a function of the synchronous phase  $\Gamma = \sin \varphi_s$  and of the number of stacking cycles  $n$ . There is an empirical formula:

$$\epsilon = \frac{1}{1 + \frac{2\Gamma}{3\sqrt{\pi} \alpha^*(\Gamma)}} , \quad (82)$$

which agrees quite well with the experimental results over a wide range of  $\Gamma$  and for not too small  $n$ . As  $\alpha^*(\Gamma)$  is a decreasing function of  $\varphi_s$ , the stacking efficiency  $\epsilon \rightarrow 1$  when  $\varphi_s \rightarrow 0$ . However small values of  $\varphi_s$  will require very long stacking times according to (77), i.e., a compromise must be made.

### II.2.4.4. Combination of Multiturn Injection and RF Stacking

Both the multiturn injection and the RF stacking have their limits in the intensity of the accumulated beams. These limits have been already discussed above.

If we combine both accumulation mechanisms, much larger intensity multiplication factors can be realized. The stacking will take place in the 4-dimensional ( $x$ ,  $x'$ ,  $W$ ,  $\varphi$ ) phase space. The physical aperture of the accelerator however must be shared by both the methods. Let  $\epsilon_0$  be the area of the transverse phase plane ( $x$ ,  $x'$ ) devoted to the multiturn

injection. In order to estimate this area a pure geometrical analysis can be carried out [118]. From Fig. 59 one can easily deduce that:

$$E_{inj} - E_{top} \leq 2E\beta^2 \left( \frac{a - \sqrt{\epsilon_0 \beta(s)}}{D(s)} \right) \quad (83)$$

must be satisfied for any point  $s$  along the circumference,  $\beta(s)$  being the Twiss amplitude function; and  $D(s)$ , the dispersion.

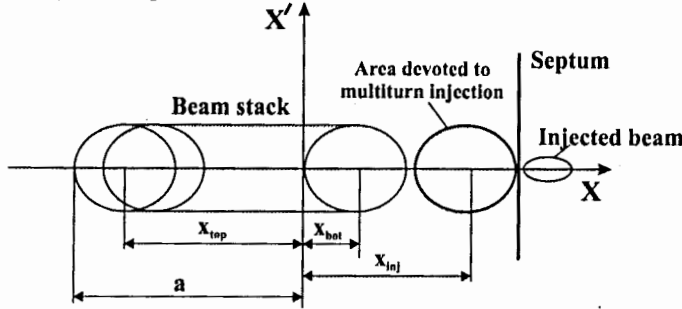


Fig. 59. Combination of multiturn injection with RF stacking

On the other hand, in the injection point:

$$E_{inj} - E_{bot} = E\beta^2 \left( \frac{\sqrt{\epsilon_0 \beta_{inj}} + d}{D_{inj}} \right), \quad (84)$$

where  $d$  is the distance between the stack edge and the center of the injected by multiturn stacking area.

Let  $s^*$  be the azimuth at which the right-hand side of (84) has a minimum and the corresponding values of  $\beta(s)$  and  $D(s)$  be  $\beta^*$  and  $D^*$ .

The number of RF cycles is:

$$n_{rf} = E_{rf} \frac{E_{bot} - E_{top}}{\Delta E}, \quad (85)$$

where  $\Delta E$  is the phase displacement of the stack during a single crossing by the buckets (74) and  $\epsilon_{rf}$  is the stacking efficiency here defined as the ratio of the ideal stack width to the width of the real stack [109].

The number of the effective turns in the multiturn stage of the combined process is:

$$n_m = \epsilon_m \frac{\epsilon_0}{\epsilon_{inj}}, \quad (86)$$

where  $\epsilon_{inj}$  is the emittance of the injected beam,  $\epsilon_m$  is the multiturn injection efficiency.

Thus the total number of effective turns will be:

$$n_{rf} = n_m n_{rf} = \epsilon_m \epsilon_{rf} \frac{E\beta^2 \epsilon_a}{\Delta E \epsilon_{inj}} \left[ \frac{2(a - \sqrt{\epsilon_0 \beta^*})}{D^*} - \frac{\sqrt{\epsilon_0 \beta_{inj}} + d}{D_{inj}} \right]. \quad (87)$$

From (87) the optimum value of the phase area devoted especially to the multiturn injection can be calculated.

#### II.2.4.5. RF Stacking Example

An example of RF stacking is the injection of accelerated in SIS-18 ions into the Experimental Storage Ring (ESR) at GSI-Darmstadt - [119]. The single-turn injection stage of the process is realized by means of septum magnet and fast kicker magnet. The kicker is

used both for injection and fast extraction. After the single-turn injection is fulfilled emittance and momentum spread of the injected beam are reduced via stochastic pre-cooling. Then the RF stacking cycle is started. It lasts 20 ms. This time is too short for a movable shutter to be applied for scrinning of the circulating stack from the magnetic field of the kicker magnet. Instead in ESR kicker a C-shaped ferrite yoke is placed opposite to the kicker magnet and absorbs the major part of the stray field. The maximum field of the ESR-kicker is  $B_{max} = 390$  Gs and the maximum deflection angle is 1.9 mrad. The rise/fall time is 110 ns and the flat-top duration is 0.3  $\mu$ s.

#### II.2.5. Combined Longitudinal and Transverse Multiturn Injection

In this injection method proposed by S. Maury and D. Mohl the stacking is in both horizontal and vertical phase spaces and in momentum space - [120]. A local closed orbit bump is created as in standard transverse multiturn injection but simultaneously with the decrease of the bump amplitude the linac energy is ramped. This is done in a way that at the injection septum the closed orbit bump corresponding to the instantaneous linac energy  $D_{septum} \frac{\delta p}{p}(t) + x_{CO bump}(t) = x_0 = const$  remains fixed - Fig. 60. Under this condition the injected ions have the same betatron amplitudes.

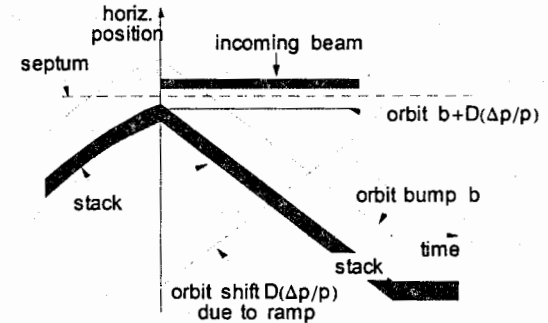


Fig. 60. Combined longitudinal and transverse multiturn injection in LEIR

In conventional transverse multiturn injection the final transverse emittance of the circulating beam is large. The momentum spread of the circulating particles is equal to that of the incoming beam. On the contrary in the combined multiturn injection the transverse emittance of the stack is much lower - Fig. 61. This is done at the expense of the increased momentum spread.

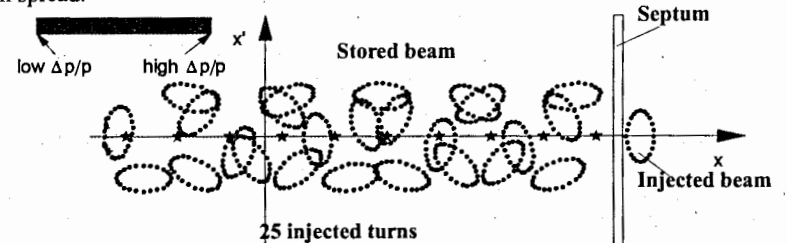


Fig. 61. Schematic picture of the combined multiturn injection

The combined multiturn injection method is applied in the heavy ion accumulator LEIR, a part of the LHC led ion chain. The injection process covers 70 turns (200  $\mu$ s) with more than 50% efficiency (35 effective turns). The mean momentum of the linac beam is increased from  $2 \cdot 10^{-4}$  to  $6 \cdot 10^{-3}$ . In order to include also the vertical phase space in the injection process an inclined electrostatic septum is used.

The LEIR injection hardware consists of a magnetic septum followed by an inclined at  $30^\circ$  electrostatic septum. The magnetic septum is 7.7 mm thick and deflects the beam by 175 mrad while the electrostatic septum has 0.1 mm foil and deflects the beam by 28.9 mrad.

In LEIR fast electron cooling at injection energy is applied. The combined multiturn injection results in small transverse emittance and large momentum spread. This is optimal for electron cooling as it leads to small cooling times which in LEIR are from 200 ms to 400 ms.

To increase the intensity in LEIR a combination of multiturn injection followed by cooling of the stored particles is used. Up to four injection-cooling stacking cycles are realized which allows to store  $9 \cdot 10^8$   $\text{Pb}^{54+}$  ions.

### II.2.6. Ion Accumulation by Stacking with Electron Cooling

An effective way of particle accumulation that is applied in the heavy ion synchrotrons SIS-18 – [121] and HIMAC – [122] and in the ion storage rings TSR – [123], CELSIUS – [124] and CRYRING – [125] is stacking by means of electron cooling of the circulating beam. This approach has several variants. One may cool the phase space area filled by multiturn injection (SIS-18) or the particle stack created by RF storage (TSR). Another approach, realized in the storage ring CELSIUS, consists in cooling the particles stored by ion stripping. In all three methods the cooling shrinks the phase space area occupied by the stored particles thus releasing space for injection of new portion of particles. If the beam lifetime is longer than the cooling time it will be possible to combine electron cooling at injection energy with the stacking. The injection consists in repetitive cycles of injection of fresh particles followed by electron cooling of the already stored beam. The electron velocity in the cooler is matched to the mean ion velocity.

The cooling time in transverse direction is given by – [126]:

$$\tau_{\perp} = 2 \cdot 10^7 \frac{\beta^4 \gamma^5 \theta^2 A}{\eta j_e Z^2}, \quad (88)$$

where:  $\beta$ ,  $\gamma$  are the relativistic factors,  $\theta_{\perp} = \sqrt{\frac{\epsilon}{\beta_x}}$  is the ion beam divergence in the cooling section,  $\eta$  is the ratio of the cooler length to the accelerator circumference,  $j_e$  is the density of the electron beam in [ $\text{A}/\text{cm}^2$ ],  $A$ ,  $Z$  are the ion mass and charge numbers.

The cooling time in longitudinal direction is – [126]:

$$\tau_{\parallel} = 2 \cdot 10^7 \frac{\beta^4 \gamma^5 \left(\frac{\Delta p}{p}\right)^2 A}{\eta j_e Z^2} \quad (89)$$

As was already described the SIS-18 synchrotron uses horizontal multiturn injection. It results in a horizontal emittance of  $150 \pi$  mm-mrad. This large emittance is reduced to  $30 \pi$  mm-mrad by means of electron cooling of the circulating beam – [121]. Now more than 80% of the horizontal acceptance is empty and multiturn injection of new batch of particles could be realized in the free of particles area. As a whole 10 to 15 cycles of repeated multiturn injection and phase space compression by cooling have been performed and the intensity increased by an order of magnitude. Further increase of the stored intensity is limited by recombination of the circulating ions with the electrons in the cooling section. In order to have large repetition rate of the cooling-stacking process we should make the transverse

cooling time as short as possible. In SIS-18 this time is about 100 ms. As the SIS-18 acceleration cycle lasts 1-3 s this cooling time is acceptable. Repetition rate of 10 Hz is achieved using electron current 1.5 A at 6.3 keV electron energy and relative cooler length  $\eta=0.014$ . By now  $4.5 \cdot 10^9$   $\text{U}^{73+}$  ions/cycle and  $3 \cdot 10^9$   $\text{U}^{28+}$  ions/cycle have been stored, while the goal values of the upgraded SIS 12/18 synchrotron are:  $4 \cdot 10^{10}$   $\text{U}^{73+}$  ions/cycle and  $2.7 \cdot 10^{11}$   $\text{U}^{28+}$  ions/cycle.

Another example of stacking by means of electron cooling is the injection in LEIR accumulator ring – [92].

The LHC heavy ion program has as a goal a luminosity  $L=10^{27}$   $\text{cm}^{-2}\text{s}^{-1}$  at 2.7 TeV/u. To achieve this luminosity 592 bunches with  $7 \cdot 10^7$  fully stripped lead ions per bunch with transverse emittance  $\epsilon=1.5 \pi$  mm-mrad and  $\beta^*=0.5$  m at interaction points is needed. Going back to the origin of the accelerator chain 200  $\mu$ A of  $\text{Pb}^{54+}$  ions at 4.2 MeV/u have to be injected into LEIR by means of combined longitudinal-transverse injection method. The purpose of the accumulator ring is to transform four 200  $\mu$ s Linac-3 pulses into two short dense LEIR bunches – Fig. 62.

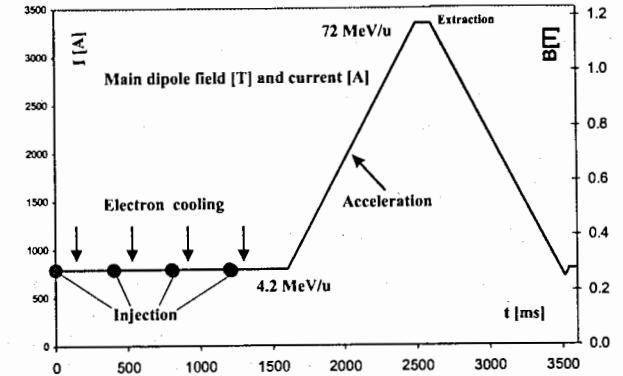


Fig. 62. Ion accumulation in LEIR by stacking with electron cooling

After stacking of 70 turns with 50% efficiency in LEIR the fast electron cooling system is switched on and the stored ions are cooled down for less than 200 ms. This short cooling time is achieved by electron cooling system with interaction length of 3 m, electron beam radius of 30 mm and electron current of 300 mA. The applied in LEIR combined multiturn injection method results in relatively small transverse emittances of the stacked beam. This is especially suitable for electron cooling as this cooling method is faster in the longitudinal plane than in the transverse one. Just after multiturn injection  $\Delta p/p=4 \cdot 10^{-3}$ ,  $\epsilon_h=70 \pi$  mm-mrad,  $\epsilon_v=30 \pi$  m-rad. As a whole  $9 \cdot 10^8$   $\text{Pb}^{54+}$  ions are accumulated after four injection/cooling cycles.

In the storage ring ESR the beam accumulation is done by combining the RF-stacking with electron cooling – [127]. First of all the injected ions are compressed by the cooling system which reduces the particle losses during deceleration to the stack. In the time between the subsequent stacking processes the coasting stack is also cooled. Thus the phase space occupied by particles is shrunk and most of the acceptance is cleaned for injection of new portion of particles. This is shown on Fig. 63 in which longitudinal Schottky scans at different times after injection are represented. Fig. 63a refers to 2000 ms after bunch injection. The cooled bunches are still on injection orbit – right peak. The coasting stack is on the left. Fig. 63b refers to 2050 ms after bunch injection. Now bunches are decelerated to the stack.

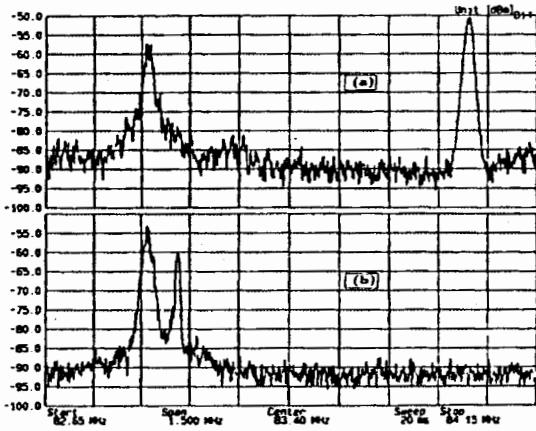


Fig. 63. Combined RF-stacking-cooling injection in ESR - [127]

The maximum intensity is determined by the equilibrium between REC process in the electron cooler and accumulation rate. With vacuum level in the chamber less than  $10^{-10}$  mbar the losses due to charge exchange with the molecules of the residual gas are negligible compared to the REC losses in the cooler.

### II.2.7. Barrier Bucket (BB) Accumulation

Recently a new method of ion accumulation which relies on a kind of wideband RF system, known as barrier RF system and stochastic or electron cooling has been developed. Ideally the barrier RF system should generate isolated rectangular voltage pulses, positive and/or negative. Analysis however shows that the longitudinal dynamics is not too sensitive to the pulse shape. Voltage pulses with arbitrary shape could be generated as a superposition of Fourier harmonics of the revolution frequency,  $f_0$ . For example isolated sinusoidal waveform can be generated by taking only first ten harmonics of the Fourier expansion. Barrier RF system needs a broadband RF cavity and a broadband power amplifiers and low level RF electronics.

The particle motion in longitudinal phase space in the general case of arbitrary voltage shape is given by:

$$\begin{aligned} \frac{d\tau}{dt} &= -\eta \frac{2\pi\Delta E}{T_0\beta^2 E_0} \\ \frac{d(\Delta E)}{dt} &= \frac{eqV(\tau)}{T_0} \end{aligned} \quad (90)$$

The canonical variables in (90) are:  $\tau$  - the time difference between the arrival of the ion and that of the synchronous particle and  $\Delta E$  - particle energy relative to the energy of the synchronous particle. The other notations in (90) mean:  $\eta$  - the slip factor,  $\beta=v/c$ ,  $q$ -ion charge state,  $E_0$  - the energy of synchronous particle,  $V(\tau)$  - the amplitude of the applied RF voltage waveform and  $T_0$  - the revolution period.

The cases of stable and unstable particle motion in barrier RF system are shown on Fig. 64.

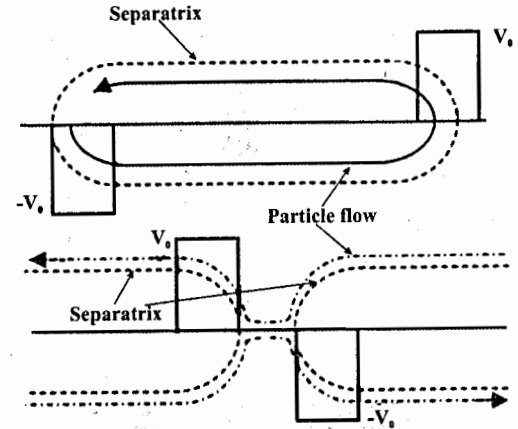


Fig. 64. Particle motion in barrier RF waves

It could be shown - [128] that the half bucket height  $\Delta E_b$  is given by:

$$\Delta E_b = \sqrt{\frac{2\beta^2 E_0}{|\eta|} \frac{\int_{T_2/2}^{T_2/2+T_1} eqV(\tau) d\tau}{T_0}}, \quad (91)$$

where  $T_1$  is the barrier pulse duration and  $T_2$  is the gap between the two RF pulses.

The longitudinal emittance in an barrier RF system is:

$$\epsilon_l = T_2 \Delta E_b + \frac{8\pi|\eta|}{3\omega_0\beta^2 E_0 eqV_{rf}} \Delta E_b^3. \quad (92)$$

The most important application of barrier RF systems is for beam injection and accumulation into storage rings with simultaneous use of beam cooling. There are two schemes of barrier bucket accumulation-with fixed and with moving barriers.

In the fixed barrier accumulation two half-wave barrier voltages of opposite sign are produced in one revolution period - Fig. 65. The resulting RF potential separates the longitudinal phase space to areas of stable and unstable synchrotron motion. The particle injection takes place in the unstable region. After that injected particles slip in phase to the stable region and they are simultaneously cooled by stochastic or/and electron cooling methods. The well cooled particles are captured by barrier voltage to the stable area. Now the unstable region is empty for injection of a new portion of particles.

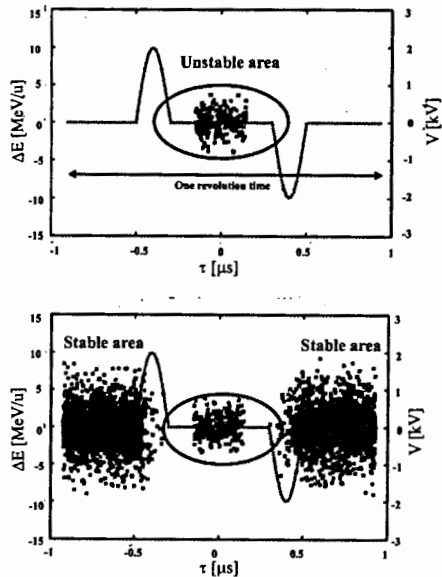


Fig. 65. Particle accumulation with fixed barrier voltage pulses

The ion accumulation by means of stationary barriers was experimented in 2007 at GSI ESR. In this proof-of-principle experiment  ${}_{40}\text{Ar}^{18+}$  beam with energy of 400 MeV/u was injected into ESR from SIS-18. The accumulation process is shown on Fig. 66.

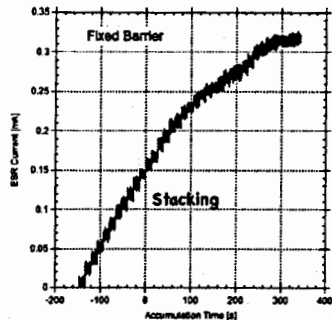


Fig. 66. Experimental results of ion accumulation in ESR with fixed barriers method

The ion accumulation by means of moving barriers method was also experimented at GSI ESR. The stacking was assisted by both stochastic and electron cooling. Cooling was in all three phase space directions and it merged the stack with the newly injected particles. The barrier pulses were sine-shaped with amplitude of 120 V and a period of 200 ns.

One of the two SIS-18 bunches was fast extracted to ESR. The ESR injection kicker pulse has 500 ns long flat top and 100 ns rise/fall time.

The process of ion accumulation by means of moving barriers is as follows – [129], Fig. 67. Two BB pulses are adiabatically introduced into the cooled coasting beam. One pulse

stays stationary while the other is moved in phase during 0.9 s to compress the beam. At  $t=1.7$  s a new portion of particles is injected into the gap between the barriers. They start debunching as the barrier height is not sufficient to capture the ions. After that the BB pulses are switched off adiabatically while the beam is being simultaneously cooled. For 120 V barrier pulses the bucket height is  $2\delta_B=5\times 10^{-4}$ .

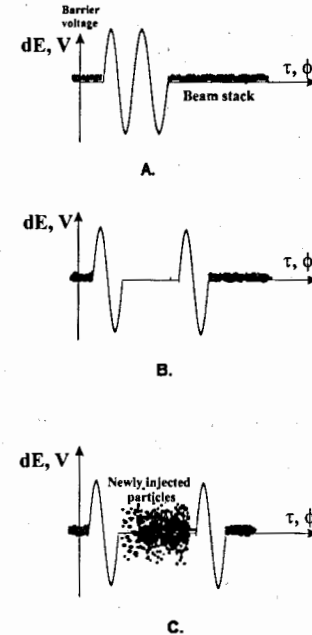


Fig. 67. Particle accumulation with moving barrier voltage pulses

The simultaneous use of stochastic and electron cooling results in a relative momentum spread of  $dp/p=2\times 10^{-5}$  which is enough to capture the stack by barriers. The ESR electron cooler has a 2.5 long interaction region. The diameter of the electron beam is 5 cm and the electron current is 0.5A.

The experimental results of ion accumulation are shown on Fig. 68.

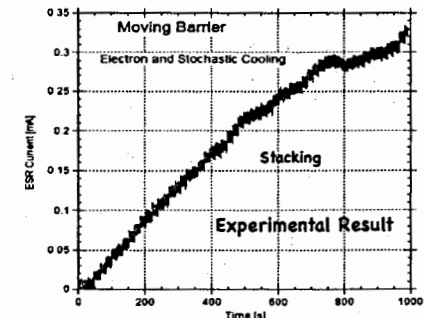


Fig. 68. Experimental results of ion accumulation in ESR with moving barriers method

### II.3. EXTRACTION

Extraction is a mechanism to get the beam out of a circular accelerator. The methods for particle ejection from ion synchrotrons are the same as those used in hadron machines.

The fast (single turn) extraction is based on the use of a fast kicker magnet which deflects the beam toward a septum magnet. The kicker is switched on between the bunches and the kicker pulse lasts during one revolution period. The septum magnet has a very low level of the stray field out of the septum aperture. Therefore it does not disturb the circulating beam. On the other hand the field in the septum aperture is uniform and strong enough to kick the ions out of the ring.

In the resonant (slow) extraction the extraction process lasts from milliseconds to hours. The ejected particles are spread over a smooth spill. The slow extraction is realized by controlled excitation of a nonlinear resonance, often a third-order integer resonance. The nonlinear resonance divides the betatron phase space to stable and unstable areas. The particles falling into the unstable area have increasing amplitude of the betatron oscillations. In the end they reach the aperture of the first extraction device—the electrostatic septum and are deflected toward the extraction channel.

In the classical (quadrupole driven) resonant extraction the area of the stable motion is reduced by slowly approaching the machine tune to the resonance tune adjusting some quadrupole magnets.

A better solution is to move the beam into a stationary resonance by accelerating/decelerating the circulating particles. Via the chromaticity the change in momentum is transformed into a change of the tune. This is the so-called accelerator-driven resonant extraction.

At CERN-LEAR a low-ripple extraction was realized applying RF white noise that causes the particles to diffuse slowly toward the resonance. By this method a variable spill length up to 1 h could be obtained.

In the RF knock-out extraction the particle betatron amplitude is increased under the influence of transverse random noise until the critical amplitude is reached. At this point the particle enters the resonance stopband, its motion becomes unstable and in the end of its cruise the particle falls into the septum gap.

#### II.3.1. Fast Extraction

The fast extraction or extraction that lasts one turn or less is used to transfer the entire beam or several bunches from one circular accelerator to another. It is also known as single turn extraction. The most frequent application is the box-car stacking from a booster injector into the main ring. Another use of the fast extraction is for secondary particle production, for example for neutrino production or for neutron production by spallation reaction.

In fast extraction the first step is to divert the beam by a kicker magnet into the gap of a septum magnet. The rise time of the kicker field must be very short, less than the beam-free gap.

The septum magnet which, usually consists of several sections, diverts the particles into the extraction channel.

While for single turn extraction the pulse duration of the kicker's pulse must be equal to the revolution period and the rise time must be less than the bunch-to-bunch spacing in bunch-by-bunch extraction the pulse duration must be equal to the bunch repetition period and the fall time must be as rapid as the rise time.

In fast extraction the kicker must deflect the beam by – [130]:

$$\theta = \frac{x}{\sqrt{\beta_k \beta_s} \sin \mu_x}, \quad (93)$$

where:  $\beta_k$  is the amplitude Twiss function at the kicker magnet;  
 $\beta_s$  is the amplitude Twiss function at the septum magnet;  
 $\mu_x$  is the betatron phase shift between the kicker and septum;  
 $x$  is the displacement of the beam at the septum.

To reduce the value of  $x$  a local orbit bump could be used.

An example of fast extraction from high energy heavy ion accelerator is the project of the fast extraction from SIS-100 synchrotron at FAIR accelerator complex – [131]. Fast extraction will be performed with a series of kicker magnets and a three stage magnetic septum – Fig. 69.

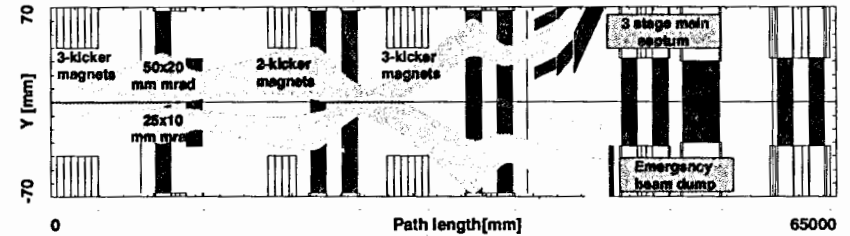


Fig. 69. Fast and emergency extraction from SIS-100 synchrotron at FAIR accelerator complex – [131]

#### II.3.2. Resonant Extraction

In high energy heavy ion synchrotrons a third-order resonance is usually used to eject the particles from the accelerator as this is in the case of hadron machines – [132]. The resonance is driven by so-called resonance sextupoles. This kind of extraction process lasts for many thousands of turns and is known as slow extraction.

In order to suppress the contribution of the resonance sextupoles to the chromaticity of the accelerator they are placed at positions with zero dispersion.

For the case of third-order resonance  $Q=m/3$ ,  $m$  being an integer, the transverse Hamiltonian  $H$  in action-angle variables  $(J, \phi)$  is given by – [133]:

$$H(J, \phi, \Theta) = \delta J + \epsilon J^{3/2} \cos 3\phi, \quad (94)$$

where:  $\theta$  is the machine azimuth

$\delta = Q - m/3$  – the distance to the resonance;

$\epsilon$  – the resonance force that is determined by the strength and location of the resonance sextupoles.

Let's remind the relation of the action-angle variables to the standard conjugate variables  $(x, p_x)$ :

$$\begin{aligned} x &= \sqrt{2J\beta_x} \cos(\phi), \\ p_x &= -\sqrt{\frac{2J}{\beta_x}} [\sin(\phi) + \alpha \cos(\phi)]. \end{aligned} \quad (95)$$

For small amplitudes:

$$H \approx \delta J, \quad (96)$$

i.e. the phase space trajectories in  $(J, \phi)$  phase space are circles – Fig. 70.

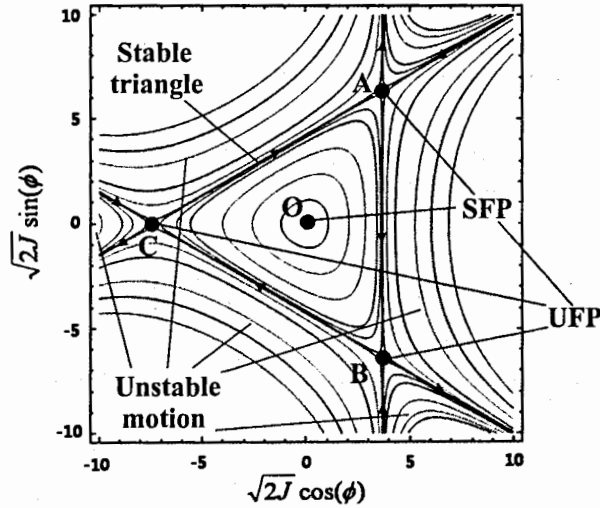


Fig. 70. Topology of the phase space under third-order resonance

For larger amplitudes the circular trajectories are distorted and obtain a typical triangular shape with rounded corners. There are four fixed points that represent the stationary trajectories. The origin of the phase space is a stable fixed point (SFP) that corresponds to the equilibrium closed orbit. The phase trajectories surrounded the origin are ellipses, i.e. bounded curves. Other three fixed points A,B,C are unstable (UFP). The phase trajectories in vicinity of UFPs are hyperbolic, i.e. they are unbounded. In the case of third-order resonance the phase trajectories passing through the unstable fixed points, known as separatrices, are straight lines. The separatrices enclose a triangular area in which the particle motion is stable. If a particle dwells at one of the UFP, say A, after one revolution period it will be at the next UFP, B, clockwise. Then after one more period it will be at the third UFP, C, and finally three turns after the beginning of its cruise this particle will come back to the initial UFP, A. The picture is similar if the particle at  $t=0$  is on one of the outgoing separatrices. Then after one revolution it will be on the next outgoing separatrix – Fig. 71 and after two turns on the third one. Thus every third revolution period the particle under consideration will return on the initial outgoing separatrix but one step outward. In the end such a particle will fall inside the aperture of the first ejecting device, the electrostatic septum (ES), and will be kicked out of the accelerator.

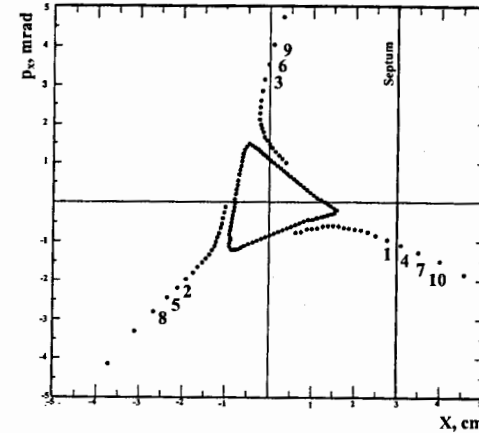


Fig. 71. Simulation of the third-order resonant extraction from Nuclotron.  $3Q_x=20$  resonance is excited by means of four sextupole lenses with field gradients  $\frac{\partial^2 B_y}{\partial x^2} = 233 \text{ T/m}^2$  in  $LS_1, LS_3$  and  $110 \text{ T/m}^2$  in  $LS_2, LS_4$ ,  $Q_x=6.658$ .

Let:

$$S \cos(m\theta - \psi) = m^{\text{th}} \text{ harmonic of } \left( -\frac{Q\beta_x}{8} \frac{\beta_x^{3/2}}{2} \frac{d^2 B_y / dx^2}{B_p} \right), \quad (97)$$

where  $d^2 B_y / dx^2$  determines the strength of the resonance sextupoles in a way that the kick received by a particle passing through the sextupole will be given by:  $\frac{1}{2} \frac{d^2 B_y}{dx^2} \frac{l_s}{B_p} x^2$ ,  $l_s$  being the length of the sextupole,  $B_p$  – the magnetic rigidity and  $x$  – the horizontal displacement from the reference orbit.

The area of the stable triangle is given by:

$$A_{\text{stable triangle}} = \frac{3\sqrt{3}}{4} \frac{(Q - m/3)^2}{S^2}. \quad (98)$$

It follows from (98) that the area of the stable region in the case of third-order resonance can be reduced either by increasing the sextupole strength  $S$  or by approaching the betatron tune  $Q$  to the resonance tune  $Q_{res}=m/3$ .

The conventional slow extraction uses the latter method. When the betatron tune approaches the resonance the separatrix shrinks and finally collapse in the centre of the phase space. The change of the betatron tune is realized controlling the excitation of several dedicated quadrupole magnets. This extraction scheme is known as quadrupole-driven slow extraction.

The spiral step along the extraction separatrix is given by:

$$\Delta x_s = \frac{6\pi S}{\sqrt{\beta_x}} (x^2 - x_{UFP}^2), \quad (99)$$

where:  $x_{UFP}$  is the coordinate of the UFP.

Due to the chromaticity the particles at different momenta are brought successively onto resonance – Fig. 72.

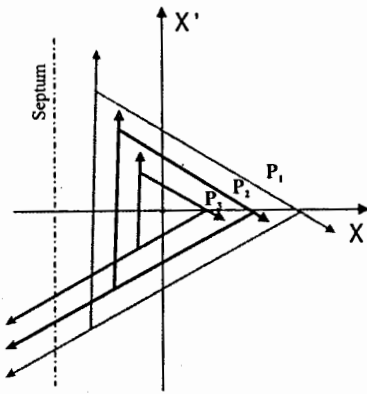


Fig. 72. Separatrices and stable triangles for particles with different momenta

In the presence of nonlinear magnetic fields the betatron tune varies with the betatron amplitude. Also the betatron tune depends on the particle momentum. According to the definition of chromaticity  $\xi$ :

$$Q = Q_0 + \xi Q_0 \frac{\Delta p}{p_0} + \Delta Q(J), \quad (100)$$

where:  $Q_0$  is the lattice tune i.e. the tune of a particle with reference momentum,  $p_0$ , and small amplitude,

$\Delta p = p - p_0$  is the momentum deviation from the reference particle,

$\xi$  is the chromaticity,

$\Delta Q(J)$  is the amplitude dependent detuning.

A convenient way to represent a third-order resonant extraction is by the so-called Steinbach diagram – [134]. This diagram shows both the beam and the resonance in amplitude-momentum space.

Let  $(u, p_u)$  be the normalized coordinates:

$$\begin{pmatrix} u \\ p_u \end{pmatrix} = \frac{1}{\sqrt{\beta_x}} \begin{pmatrix} 1 & 0 \\ \alpha_x & \beta_x \end{pmatrix} \begin{pmatrix} x \\ x' \end{pmatrix}. \quad (101)$$

In normalized coordinates the unperturbed linear motion is smoothed to harmonic oscillations with circular phase trajectories. A particle rotates along such a circular trajectory  $Q$  times per revolution.

Let  $A = \sqrt{\frac{\epsilon}{\pi}}$  be the normalized amplitude of the betatron oscillations,  $\epsilon$  being the single particle emittance. The resonant extraction starts when the area of the shrinking stable triangle equals the emittance. According to this condition and to (98) the amplitude-

momentum space is divided to areas with stable and unstable motions. The unstable region has 'V' shape and is centered on the resonance tune – Fig. 73.

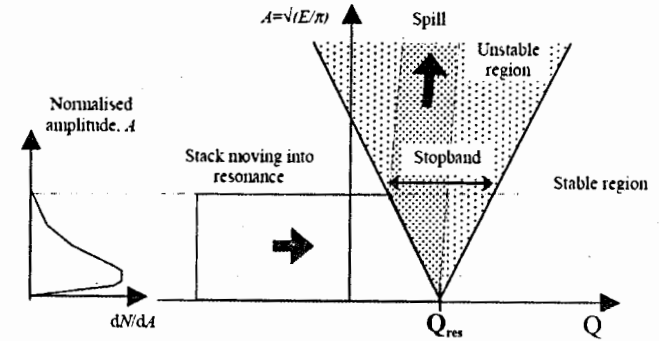


Fig. 73. Steinbach diagram – [134]

The conventional third-order resonance extraction process could be represented on the Steinbach diagram as this is shown on Fig. 74. The abscissa on Fig. 74 is the relative momentum deviation from the momentum of the reference particle which is related to the betatron tune via the chromaticity and the ordinate is the normalized betatron amplitude. The slope of the V-shaped region is proportional to  $\frac{\xi Q_0}{s} = \frac{Q'}{s}$ .

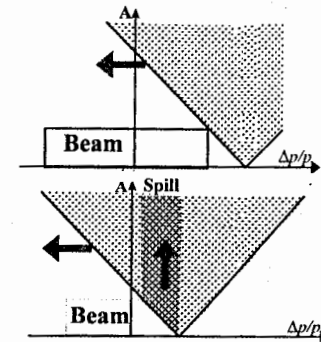


Fig. 74. Conventional (quadrupole-driven) third-order resonant extraction

In the quadrupole driven resonant extraction the extraction separatrix and the spiral step toward the electrostatic septum vary during extraction.

It could be proved that at third-order resonant extraction the following relation is fulfilled:

$$\left(u - D_n \frac{\Delta p}{p}\right) \cos(\alpha - \Delta\mu) + \left(p_u - D'_n \frac{\Delta p}{p}\right) \sin(\alpha - \Delta\mu) = h, \quad (102)$$

where:  $\alpha$  is the angle that determines the orientation of the outgoing separatrix at the equivalent (virtual) resonance sextupole. The virtual sextupole is a single sextupole lens that affects the beam in a way which is equivalent to the combined effect of the system of

resonance sextupoles,  $\Delta\mu$  is the phase advance from the equivalent resonance sextupole to the electrostatic septum,  $h$  is the distance from the side of the stable triangle to its centre,

$$h = \frac{4\pi}{s} \delta Q = \frac{4\pi}{s} Q' \frac{\delta p}{p},$$

$Q' = \xi Q_0$  being the chromaticity,

$D_n$  is the normalized dispersion,  $D_n = \frac{D}{\sqrt{\beta_x}}$ .

If:

$$D_n \cos(\alpha - \Delta\mu) + D'_n \sin(\alpha - \Delta\mu) = -\frac{4\pi}{s} Q' \quad (103)$$

the extraction separatrices will not depend on the particle momentum. Condition (103) is known as Hardt condition under the W. Hardt, who discovered it in 1981 – [134,139].

Transverse phase space with fulfilled Hardt condition is shown on Fig. 75.

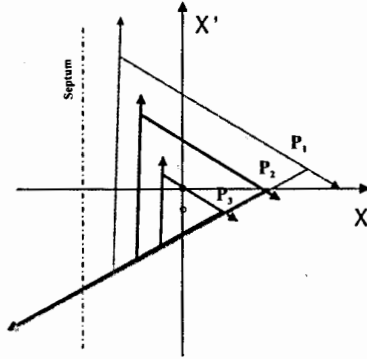


Fig. 75. Separatrices and stable triangles when the Hardt condition is fulfilled

As this was described above if the tune is close to the resonance tune the nonlinear field of the resonance sextupoles guides the particles slowly across the first ejecting device – the electrostatic septum. The ES separates the extracted particles from the circulating beam and directs them to the second ejecting device – the magnetic septum. The magnetic septum has much larger deflecting angle than the electrostatic one. It directs the ejected particles toward the extraction channel.

Each septum device defines two spaces. Inside the septum aperture the field (electric or magnetic) is homogeneous and strong enough to deflect the particles out of the accelerator. Outside the septum aperture the fringe field must be almost zero in order not to affect the circulating beam. The septum itself is the partition separating these two spaces.

The loss of particles during the resonant extraction (extraction efficiency) is determined by the ratio of the septum thickness to the spiral step toward the resonance. To reach high efficiency the separation between the zero field and high field regions in the septum device must be very thin (0.1 mm or less). This could be realized only with some kind of a DC electrostatic device – the electrostatic septum.

The main requirements that the resonant extraction should meet are:

- High efficiency i.e. small particle loss;
- The extracted beam must have small transverse emittances. This will facilitate the particle transport through the extraction channel with small loss;

- The spill envelope must be almost flat. The main source of the intermittent time structure of the extracted beam current is the current ripple of the magnet power supply. The parameter of merit is the duty factor:

$$F = \frac{\langle \phi \rangle^2}{\langle \phi^2 \rangle}, \quad (104)$$

where:  $\phi = \frac{dN}{dt}$  is the particle flux in the spill. The averaging in (104) is over the spill time.

For the simplified case of a sinusoidal modulation of the spill:

$$\phi = \phi_0 + \phi_r \cos(\omega t), \quad (105)$$

$$F = \frac{1}{1 + \frac{1}{2} \frac{\phi_r^2}{\phi_0^2}}. \quad (106)$$

As an example of conventional slow extraction we will describe the third-order resonant extraction from the Nuclotron synchrotron at JINR, Dubna – [135]. Two pairs of sextupole lenses are used to excite  $3Q_x=20$  resonance. Four extraction quadrupole lenses with linearly changed excitation current are used to approach the resonance frequency and to control the particle spill. The electrostatic septum has a length of 3 m – Fig. 76. The septum is made of tungsten-rhenium wires 0.1 mm thick. The gap between the septum and the high voltage electrode could be changed from 10 to 30 mm. The maximum applied voltage is 250 kV which provides for a deflection angle of 2 mrad.

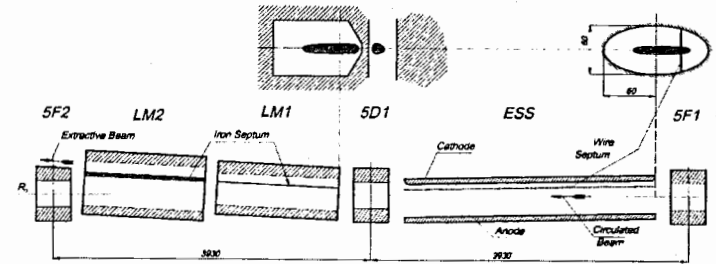


Fig. 76. Slow extraction system from Nuclotron – [135]

The second, magnetic septum, is Lambertson magnet, which deflects the beam in vertical direction. In Nuclotron it consists of two 1.5 m sections and deflects the particles vertically by 96 mrad.

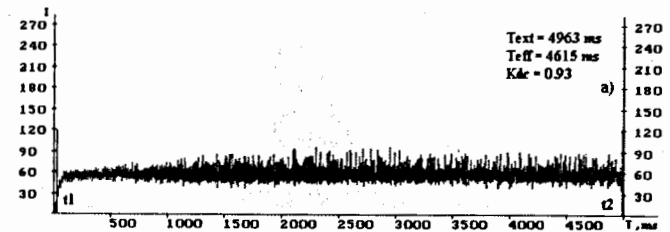


Fig. 77. Nuclotron beam spill with feedback system on – [136]

The beam spill has modulation components in the range from 10 Hz up to 600 Hz which are due to the current ripples in the power supplies of the extraction quadrupoles and extraction septum magnets. For extraction duration from 0.4s to 5s the spill could be made smooth (uniformity of 0.9) by applying of a feedback control – Fig. 77 – [136].

### II.3.3. Stochastic Resonant Extraction

This extraction mechanism was proposed by S. van der Meer in 1978 – [137] and further developed in antiproton storage ring LEAR at CERN by W. Hardt and others – [138,139]. As the stochastic extraction may last too long, up to hours, it is also known as ultraslow extraction.

The principle of the stochastic resonant extraction is to apply filtered RF noise over a frequency band that overlaps the revolution frequencies of the circulating particles. Under the influence of this noise the particles start to diffuse in the longitudinal phase space toward the resonance.

The advantages of stochastic extraction is that the particles could be guided very slowly across the resonance and that the extracted flow of particles has much lower ripples than in conventional resonant extraction.

Let:

$$\Psi = \frac{dN}{d(\frac{\Delta P}{p})} \quad (107)$$

be the particle density as a function of fractional momentum.

The diffusion by stochastic noise is described by the following equation:

$$\frac{\partial \Psi}{\partial t} = \frac{\partial}{\partial (\frac{\Delta P}{p})} D \frac{\partial \Psi}{\partial (\frac{\Delta P}{p})}, \quad (108)$$

where the diffusion coefficient is:

$$D = \frac{1}{2} \frac{V^2}{\Delta f} \frac{1}{(2\pi R B \rho)^2}, \quad (109)$$

$V$  – RMS noise voltage;

$\Delta f$  – the band width covered by the noise;

$R$  – mean machine radius.

The noise is applied by a dedicated RF-cavity.

The stochastic extraction starts with a flattening and widening procedure. To do this white RF noise with rectangular power density distribution is applied. It makes the particles to diffuse toward a uniform distribution over the frequency band – Fig. 78.

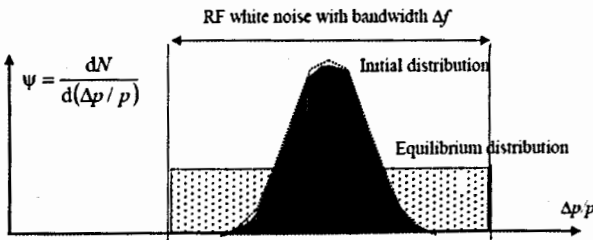


Fig. 78. Beam shaping and homogenization by filtered RF noise

After beam flattening a wider band RF noise is applied with carrier frequency that moves so that the low frequency edge of the noise spectrum coincides with the high frequency edge of the beam – Fig. 79. Stochastic extraction follows the linear sweep of the carrier frequency.

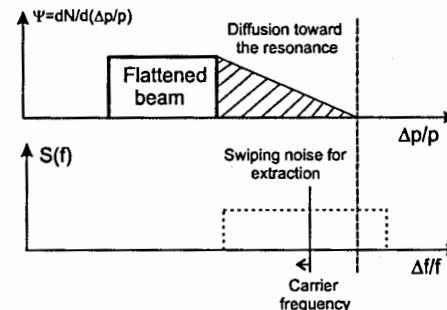


Fig. 79. Stochastic resonant extraction

In stochastic resonant extraction a duty factor as high as 99% has been achieved.

### II.3.4. RF Knock-Out Extraction

In RF Knock-Out extraction method (RF-KO) the beam is excited by transverse stochastic noise – [140-142]. This noise causes the circulating particles to diffuse in the transverse phase space which makes the amplitude of the betatron oscillations increase slowly with small fluctuations – Fig. 80. When the amplitude passes a threshold value the motion becomes unstable and the particle will be extracted.

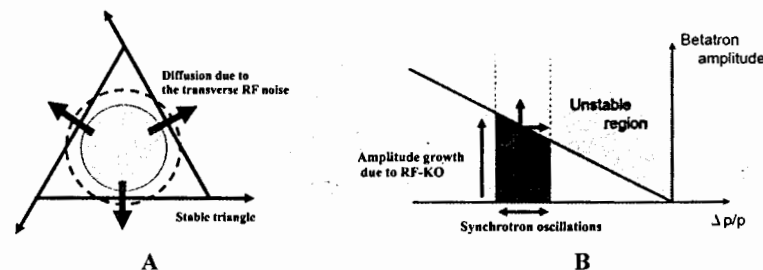


Fig. 80. Principle of the RF knock-out extraction method

Since the separatrix is kept constant the orbit gradient and turn separation at the ejection septum are constant. Due to this condition the emittance of the extracted beam is small which leads to small loss during transportation of the particles through the extraction channel.

The frequency of the transverse RF signal must be equal to the product of the revolution frequency times the fractional part of the tune. Due to the amplitude dependence of the tune in the presence of nonlinear magnetic field and to the momentum dependence when the chromaticity is non-zero the RF frequency has to be modulated. At HIMAC the frequency of the transverse RF field is modulated with saw-tooth wave in order to match both the tunes

which lie near the separatrix(extraction region) and tunes that lie deeply inside it (diffusion region).

Because of the effect of random motion due to the applied noise the spill ripples in the RF-KO method are much smaller. The method provides for fast response of the switching beam on/off. With modulation of noise amplitude one can control the time structure of the extracted beam. Together with the use of feedback-systems this will result in a square shaped spill.

The RF-KO method is routinely used at HIMAC medical synchrotron in Chiba. A fast response of beam on/off is achieved with cut-off time of 50  $\mu$ s. The global time structure of the extracted beam is controlled by a proper amplitude modulation of transverse RF field.

The RF-KO extraction method is used in the upgraded synchrotron SIS 12/18 – [143-45]. The RF exciter consists of two parallel stripline electrodes each 750 mm long and 200 mm apart. They provide the horizontal electric field with maximum effective voltage of 1.3 kV.

RF-KO method will be used also for the resonant beam extraction out of the SIS-100 FAIR synchrotron.

### II.3.5. Extraction by Betatron Core

In betatron core driven extraction induction acceleration is used to change the particle tune via the chromaticity and to move the beam toward the resonance. The hardware consists in a ferromagnetic core with induction coil wound on it – Fig. 81. A time variable magnetic flux through the ring induces a curl electric field on its axis. This electric field accelerates the circulating particles changing their momenta. Similar equipment is used in the linear induction accelerators.

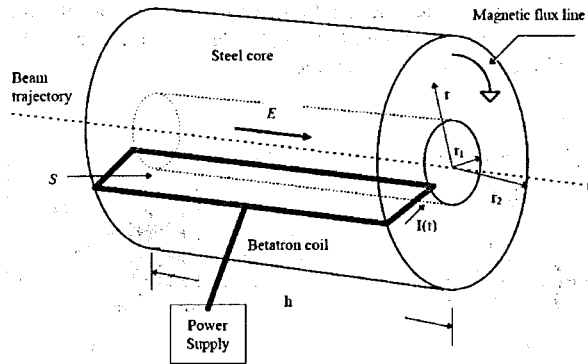


Fig. 81. Schematic view of the betatron core

Extraction separatrix and spill step are constant during extraction. The Hardt condition could be fulfilled, i.e. the extraction separatrices of different momenta could be superimposed. Particles with different amplitudes and momenta are extracted at the same time. For that reason in the betatron core driven extraction the sensitivity to current ripples is reduced and the spill is smoother – [146].

Betatron core driven extraction has been used for first time in Saturn-II synchrotron at Saclay. A  $\pm 20\%$  stability of the spill intensity has been reached which corresponds to a duty factor of 0.98.

## II.4. RF SYSTEM

The RF system of an accelerator creates stable areas in the longitudinal phase space, the so-called RF buckets, in which the injected ions are captured forming tight bunches of particles – [147, 148]. Then the RF system accelerates ions to the top energy in synchrotrons or makes them circulate at a constant energy in storage rings. The RF system is also used to perform different kind of manipulations of the beam in the longitudinal phase space, known as RF gymnastics. These are bunch splitting, bunch shaping using higher harmonics, bunch rotation, longitudinal emittance blowup etc.

We can divide the ion accelerators to low- $\beta$  ( $\beta=v/c$ ) machines and high- $\beta$  machines.

In low- $\beta$  accelerators the ion velocity changes significantly during the machine cycle. The frequency of the accelerating RF field must also vary significantly following the synchronous energy. In narrowband (high- $Q$ ) systems this is done by using in the accelerating cavities magnetic materials with adjustable permeability. Recently RF cavities with novel amorphous or nanocrystalline metal alloy (MA) have been developed. These are wideband (low- $Q$ ) cavities which allows RF frequency sweep without cavity tuning.

In large synchrotrons and storage rings the ion beams are ultrarelativistic (high- $\beta$ ) which relieves the bandwidth constraints.

The block-diagram of an accelerator RF system is shown on Fig. 82.

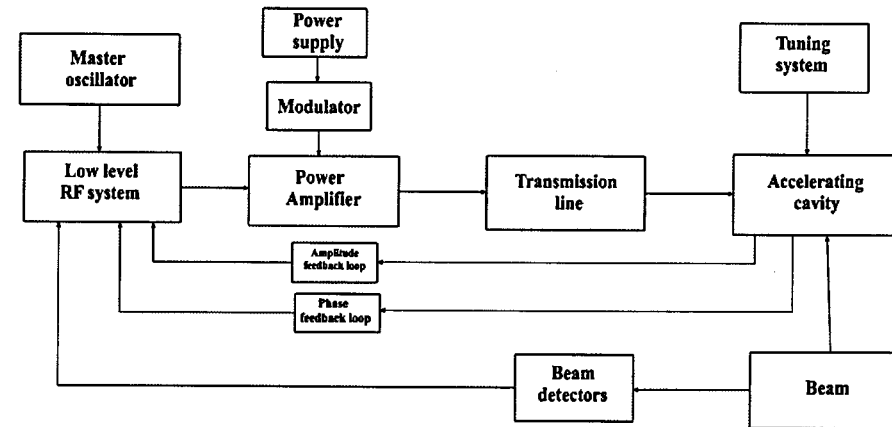


Fig. 82. Block diagram of an RF system – [148]

The necessary RF power is provided to the cavity by the power amplifier. RF tubes (tetrodes) or klystrons are used as active devices. The transmission lines are either coaxial cables or waveguides. The input impedance of the cavity could be matched to the feeder line or not matched (only for tube amplifiers). The Low Level RF electronics (LLRF) is used to stabilize the accelerating field in the cavity. Two kinds of feedback loops are used. One of them measures the amplitude and phase of the accelerating RF field and feedback signals to LLRF system. The other feedback loop measure phase, transverse position or frequency spectrum of the beam, process the obtained information and pass control signals back to LLRF system. Then the LLRF system drives the power amplifier.

### II.4.1. Ferrite Cavities

The revolution frequency even in small ion accelerators is less than 10 MHz. For that reason the accelerating cavities will have reasonable sizes only by using magnetic materials with high permeability.

In narrowband cavities stacks of NiZ based ferrite ring cores are used – [149,150]. The cavity is tuned by adjusting the current in bias windings. This may be figure-of-eight current windings around two ferrite stacks with a gap in the middle. In the so-called 1:2 transformation solution the two ferrite stacks are excited due to bias current windings but the coupling loop surrounds only one of the stacks.

Disadvantages of the ferrites are:

- Low saturation field ( $\sim 0.3$  T) which leads to relatively low accelerating gap voltages;
- Low Curie temperature ( $100^\circ\text{--}250^\circ\text{C}$ ) i.e. a proper cooling of the ferrite ores is necessary.

Typical parameters of ferrite cavities are:  $\mu_r \sim 100$  and  $Q \sim 10\text{--}50$ .

For magnetic materials an important figure of merit is the  $(\mu_r Q)$  product. It could be shown that the shunt impedance of the coaxial ferrite cavity is given by:

$$R_p = \mu_0 N t (\mu_r Q f) \ln \frac{r_o}{r_i}, \quad (110)$$

where  $N$  is the number of ferrite ring cores,  $t$  is the thickness of one core,  $r_i$ ,  $r_o$  are the inner and outer radii.

In ferrites the power loss product  $(\mu_r Q f)$  decreases at high flux densities.

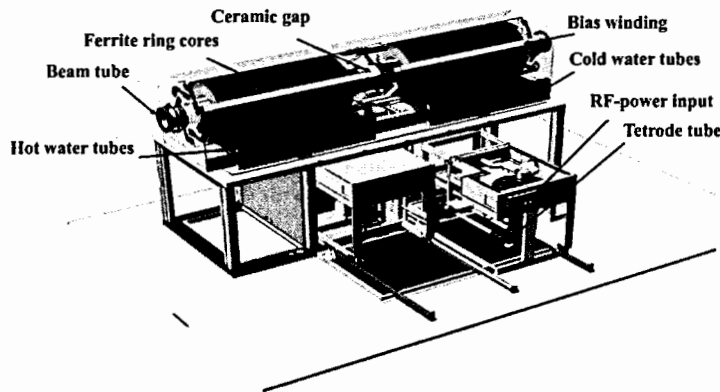


Fig. 83. SIS-18 accelerating cavity – [150]

As an example of ferrite cavity we will describe the SIS-18 accelerating cavity- Fig. 83, 84. The length of the cavity is 3.4 m. It is filled with 64 ring cores with dimensions  $r_o=249$  mm,  $r_i=110$  mm and  $t=25$  mm. The ring cores are cooled by copper ring disks. The maximum accelerating voltage is  $V_{gap}=16$  MV. A single-ended tetrode amplifier supplies the necessary energy. The quality factor is  $Q=10$ . The RF frequency vary from 0.8 MHz to 5.4 MHz ( $h=4$ ).

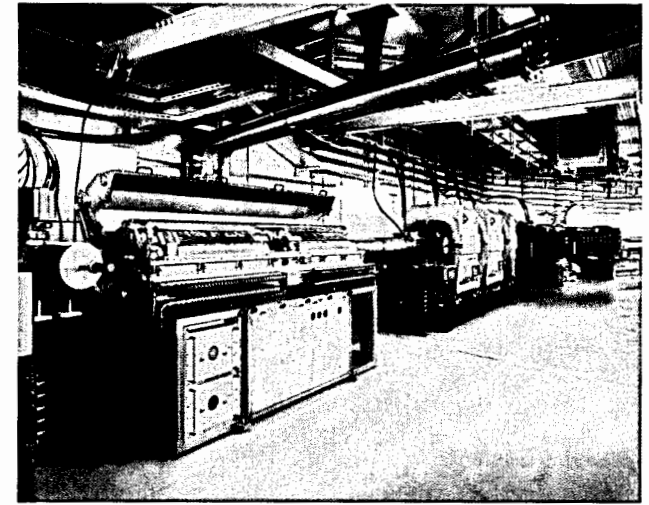


Fig. 84. SIS-18 accelerating cavity at the ring – [151]

### II.4.2. Magnetic Alloy (MA) Cavities

A new development in the field of RF cavities is the cavities filled with novel amorphous (Co-based) or nanocrystalline (Fe-based) magnetic alloy materials – [152,153]. One example of MA is Finemet from Hitachi Ltd.

The main characteristics of this type of magnetic materials are:

- Low  $Q$ -factor (0.6-1.0) i.e. this are wideband cavities and no tuning for frequency sweep is necessary. Due to low  $Q$  arbitrary waveforms are possible;
- The  $(\mu_r Q f)$  product does not depend on the flux density – Fig. 85;

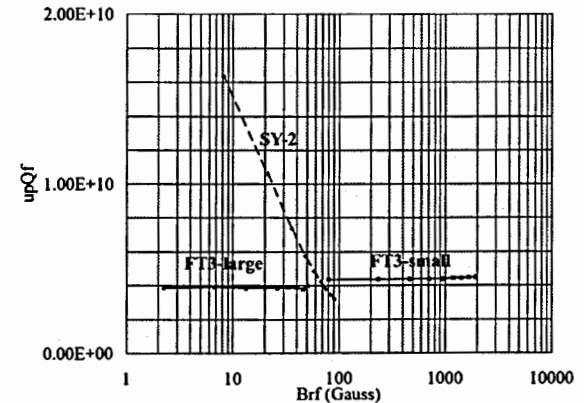


Fig. 85. Magnetic flux density dependence of magnetic materials. SY-2 is a typical ferrite core; FT3-small and FT3-large are MA cores with different sizes – [152]

- Very high Curie temperatures ( $\sim 570^\circ\text{C}$ ) i.e. the parameters of the core remain constant below  $100^\circ\text{C}$ ;
- Linear permeability  $\mu(B)$ ;
- Low power density at high voltages;
- High saturation field ( $\sim 1.2\text{ T}$ ) which allows for high accelerating gap voltages to be generated and the overall length of the cavity can be very short-high gradient cavities (HGC) – Fig. 86;
- It is possible to produce large cores with about 100 cm in diameter.

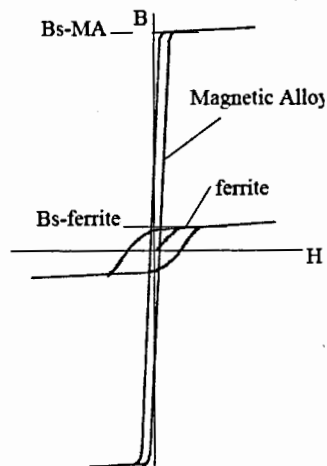


Fig. 86. The hysteresis curves for magnetic materials – [152]



Fig. 87. The high gradient cavity installed in HIMAC – [153]

An example of MA cavities is the accelerating cavity of the medical heavy ion synchrotron HIMAC – Fig. 87. With 60 kW of RF power a maximum voltage of 4 kV is obtained with a cavity only 40 cm in length. The frequency range is 1-8 MHz. A push-pull RF amplifier with two tetrodes drives the MA cavity. Due to the large bandwidth of the MA cavity the frequency sweeping is achieved without tuning circuit.

### II.4.3. Storage RF System

In colliders at colliding mode the purpose of the RF system is to provide longitudinal focusing to maintain short bunches for the physical investigations at the presence of strong intrabeam scattering. As a rule this is done by a separate RF system, the so-called storage RF system.

In RHIC ion collider the storage RF system consists of four cavities placed in an interaction area and common for both beams and three cavities per ring in the arc region – [87]. It operates at 196.1 MHz. The accelerating voltage is 6 MV.

Prior to the transfer of the beam to the storage RF system it is usually necessary to reduce the bunch length by means of bunch rotation. In RHIC when the ions are accelerated by accelerating RF system ( $f=28.15\text{ MHz}$ ,  $h=360$ ) to the top energy the bunch is shifted to the unstable fixed point. There the bunch is enlarged in a fraction of synchrotron period. After that the bunch is shifted back to the stable fixed point. Being mismatched with the RF bucket it starts to rotate. In  $3/8$  of a synchrotron period the bunch reaches its minimum length position and the storage RF system is switched on.

In SIS-18 another method for fast bunch compression is applied. It consists in sudden switch on of an additional RF voltage. The bunch is now mismatched with the RF bucket and starts to rotate. The compression takes only a quarter of a synchrotron period. Final bunch length depends on the initial momentum spread. The SIS-18 bunch compressor cavity is a MA cavity with length of 1 m, gap voltage 30 kV, resonant frequency 0.8 MHz, quality factor  $Q=1.0$ , and pulse duration 0.1 ms. The result of the compression is shown on Fig. 88.

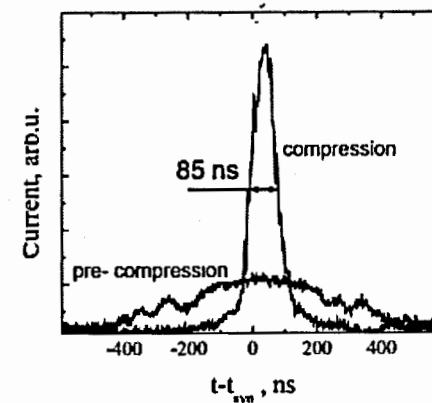


Fig. 88. Fast bunch compression in SIS-18

### II.4.4. Double RF System

In order to reduce the space-charge problems, especially harmful during injection, an RF system working at two times higher harmonic number is used in addition to the fundamental accelerating RF system – [154]. The accelerating voltage in such double RF system is:

$$V(\phi) = V_0(\sin \phi - \sin \phi_s - 0.5 \sin 2(\phi - \phi_s)). \quad (111)$$

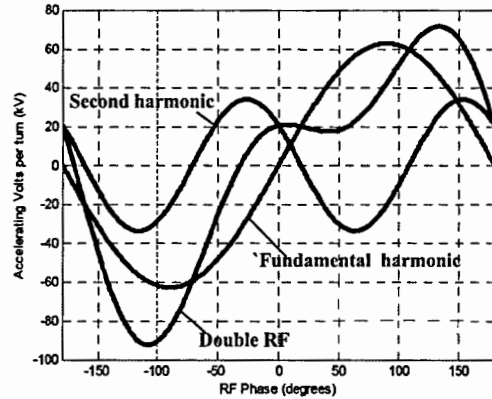


Fig. 89. Acceleration voltage in a double RF system

In double RF system the bunches are longer and more flattened. This makes the bunching factor higher and reduces the space-charge forces. Moreover in double RF systems the synchrotron tune spread in the bunches is also higher. This helps damping the couple bunch instabilities through the Landau damping mechanism.

Double RF systems are used in many accelerators: PSB, ISIS, J-PARK, SIS 12/18, LEIR etc.

During the SIS-18 upgrade program one of the existing ferrite cavities working at fourth harmonic of the revolution frequency was replaced by a  $h=2$  cavity thus forming double RF system – [155-157]. The new cavity is wide bandwidth cavity utilizing Fe-based magnetic alloy Finemet FT-3M ring cores from Hitachi Metals Ltd. The gap voltage is 50 kV. A 300 kW tetrode based push-pull RF power amplifier is placed on the top of the cavity – Fig. 90.

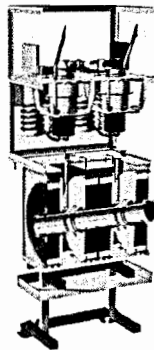


Fig. 90. Broadband cavity at SIS-18 with the power amplifier on top – [155]

The effect of SIS-18 double RF system is shown on Fig. 91.

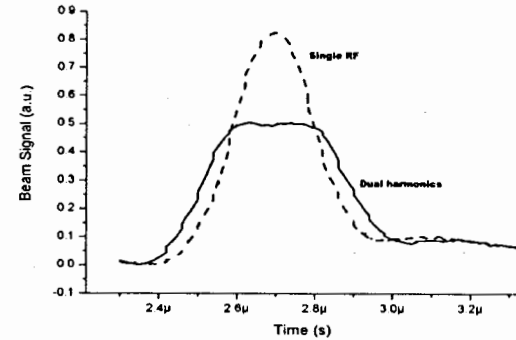


Fig. 91. Bunch profile with single and double RF systems at SIS-18 – [157]

### II.4.5. Transition Crossing

In some synchrotrons the ions must cross the transition energy during acceleration. For example in the heavy ion collider RHIC all ions except protons are accelerated though the transition energy at  $\gamma_{tr}=22.86$  – [158]. At transition crossing the synchronous phase has to change rapidly from  $\phi_s$  to  $(\pi - \phi_s)$  in order to reduce the particles loss and longitudinal emittance increase. But in superconducting accelerators like RHIC the acceleration rate is low. In RHIC it is  $\frac{d\gamma}{dz} = 0.4 s^{-1}$ . To solve the transition crossing problems in RHIC a  $\gamma_{tr}$  – jump method is applied. It consists in increase of the transition crossing speed by means of fast pulsed quadrupoles. These quadrupoles are placed in nonzero dispersion areas and they change rapidly the momentum compaction factor  $\alpha$  and hence  $\gamma_{tr}$ . It could be shown that to first order of the jump quadrupole strength  $q_j$ :

$$\Delta\gamma_{tr} = \frac{v_{tr}^2}{2C} \sum_i q_i D_i^2, \quad (112)$$

where  $C$  is the accelerator circumference and  $D_i$  is the dispersion at the jump quadrupole.

In an synchrotron particles cross transition at different times according to their momentum. For particles with maximum relative momentum deviation  $\delta = \pm \delta_{max}$  the transition crossing time offset is equal to  $\pm T_{nl}$ .  $T_{nl}$  being the so-called nonlinear time. Particles with different momenta cross the transition at times that satisfy the condition:

$$|\gamma_{tr} - \gamma(t)| < \dot{\gamma} T_{nl}. \quad (113)$$

In RHIC  $T_{nl}=355$  ms. During that time there are particles in the beam which undergo an unstable motion.

Each sextant of RHIC rings contains two families of the jump quadrupoles. One family is placed in dispersive section and they produce fast change of  $\gamma_{tr}$ . The polarity of the jump quadrupoles are changed in 40 ms time – [159]. This increases the rate of the transition crossing by factor 60 and reduces the nonlinear time below 20 ms – Fig. 91.

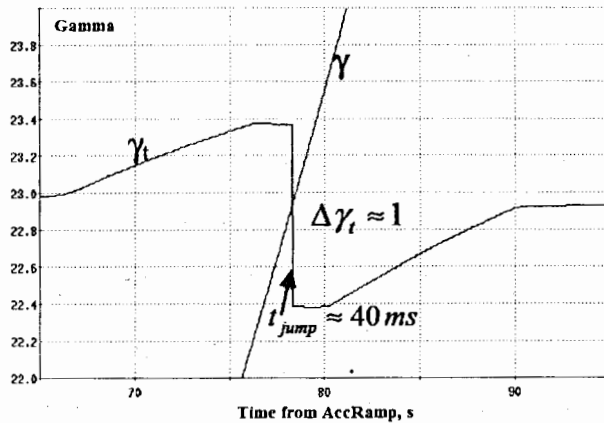


Fig. 92. Changes of  $\gamma$  and  $\gamma_{tr}$  in vicinity of transition crossing at RHIC – [159]

Another jump quadrupole family is lace in a low dispersion region. They compensate the betatron tune change caused by the first family.

#### II.4.6. Superconducting Cavities

In LHC the choice was in favor of superconducting acceleration cavities – [160,161]. Niobium on copper technology is used. The cavities operate at 4.5K. The major advantage of superconducting cavities is the extremely low surface resistance. The quality factor is very high.

In LHC the beam consists of trains of bunches spaced by empty gaps which are larger than the rise time of the injection kickers. Due to the gaps the RF system undergoes periodic loading by the beam. This effect is proportional to  $(\frac{R}{Q} \times \frac{1}{V})$ ,  $\frac{R}{Q}$  being the geometric cavity parameter and V the cavity voltage. For superconducting cavities this parameter can be made one order of magnitude smaller than for normal-conducting copper cavities. Also superconducting cavities offer the possibility of running the collider with much less RF power, and the contribution of the superconducting cavity to the overall machine impedance is much smaller.

Eight RF stations per beam tuning at 400 MH push the particles to the top energy. The accelerating field in the cavity is 5.3 MV/m. Each station includes a single-cell superconducting cavity – Fig. 93, a 330 kW klystron and low level RF electronics. The accelerating voltage per beam is 16 MV. The LHC cavity uses a purely mechanical tuner.

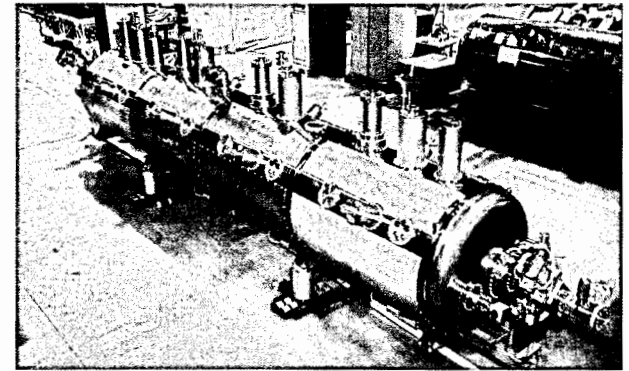


Fig. 93. LHC superconducting cavity

### II.5. ION COLLIDERS

Although the heavy ion and the hadron colliders are based on one and the same principles the very nature of heavy ions sets specific constraints on the collider performance and affects the design of the collider systems.

The physical phenomena that determine the features of a heavy ion collider have been discussed in the first part of this book.

For example due to the intrabeam scattering the heavy ion beams grow within a few hours to large transverse and longitudinal dimensions. This demands for stronger focusing by the magnetic system and for larger aperture of the magnets. The longitudinal bunch dimensions at the end of the storage determine the parameters of the RF system.

Another limit on the collider performance comes from the ion induced vacuum pressure instability. To cope with this adverse effect besides the increase of pumping power and the use of low outgassing materials a sophisticated collimation system must be applied.

The possibility for formation of an electron cloud that accompanies the ion beam must also be taken into account, especially when the collider works with a large number of highly populated bunches. In ion machines this was observed for the first time at RHIC in 2001. In an attempt to work with intense ( $1 \cdot 10^9$  ions/bunch), closely spaced (107 ns) bunches an intolerable vacuum pressure rise up to  $7 \cdot 10^{-7}$  Torr was measured. As the pressure rise was sensitive to the bunch intensity and spacing it was attributed to the electron cloud effect. How it is possible to overcome the formation of electron cloud was described in I.2.4.

As a rule the heavy ion collider is built on the base of already existing in the laboratory chain of accelerators which serves as ion injector. This circumstance imposes significant constraints on the design of the collider.

Contrary to the hadron colliders the heavy ion colliders operate with a large range of mass numbers (theoretically from 1 to 238) and atomic numbers (theoretically from 1 to 92). The figure of merit is the ratio  $A/Z$  which varies from 1 for protons up to 2.03 for  $^{197}\text{Au}^{79+}$  (BNL), and 2.54 for  $^{208}\text{Pb}^{82+}$  (CERN). It determines the beam rigidity as the energy per nucleon in the two beams must be the same in order to maintain equal revolution frequencies in both rings.

For the physical program it is important that the collider could work not only at the maximum energy but over an energy range and that it supports the option of colliding beams

of different species. The extreme case is colliding protons on the heaviest for the collider ions. To do this the collider must be based on two essentially separate rings (including interaction regions) that are capable to work at different magnetic fields.

At the moment there are two heavy ion colliders in operation: RHIC and LHC. The main parameters of these colliders at collision energy are summarized in Table 6.

**Table 6.** Parameters of existing heavy ion colliders

Parameter	RHIC	LHC
Reference ion	$^{197}\text{Au}^{79+}$	$^{208}\text{Pb}^{82+}$
Energy per nucleon, GeV/u	100	2759
Circumference, km	3.83	26.66
Dipole field, T	3.45	8.33
Peak luminosity, $\text{cm}^{-2} \cdot \text{s}^{-1}$	$1.0 \times 10^{27}$	$1.0 \times 10^{27}$
Number of bunches	56	592
Number of ions per bunch	$1 \times 10^9$	$7.0 \times 10^7$
RMS beam size at IP, $\mu\text{m}$	110	15
RMS bunch length, cm	18	7.5
Twiss beta-function at IP, m	1.0	0.5
Beam-beam tune shift per IP	0.002	0.00015
Stored energy per eam, MJ	0.2	3.81
Luminosity lifetime, h	10	9.3

A new heavy ion collider called NICA (Nuclotron-based Ion Collider facility) is under construction at JINR, Dubna. The main parameters of this new collider are listed in the Table 7.

**Table 7.** Parameters of the heavy ion collider NICA

Maximum energy ( $\text{Au}^{79+}$ )	4,5 GeV/u
Circumference	503.04 m
Number of bunches	23
Ions per bunch	$6.1 \cdot 10^9$
Beta-function at IP	0.35 m
RMS bunch length	60 cm
Luminosity	$6.7 \cdot 10^{27} \text{ cm}^{-2} \cdot \text{s}^{-1}$

### II.5.1. Luminosity

The luminosity  $L$  is a measure of the ability of the collider to produce events – [162]. It is defined as the event rate per unit cross-section:

$$\frac{dR}{dt} = L\sigma, \quad (114)$$

where  $dR/dt$  is the counting rate for the event of interest and  $\sigma$  – the event cross-section.

In accelerator practice it is accepted to measure the luminosity in  $[\text{cm}^{-2} \cdot \text{s}^{-1}]$ .

For the case of head-on collisions of two round beams with Gaussian bunches the peak luminosity per interaction point is given by:

$$L = \frac{N_B^2 f}{A}, \quad (115)$$

where:  $N_B$  is the number of particles per bunch,

$f = f_{rev} B$  – the collision frequency,

$f_{rev}$  – the revolution frequency,

$B$  – the number of bunches,

$A$  – the bunch transverse area,  $A = 4\pi\sigma^2$ ,

$\sigma^*$  – the RMS transverse bunch size at interaction point.

The true figure-of-merit is the integrated luminosity:

$$L_{int} = \int_0^T L(t) dt. \quad (116)$$

It determines the whole number of registered events through  $R = L_{int}\sigma$  and is measured in units of reversed picobarns,  $[\text{pb}^{-1}]$ .

The optimum luminosity is achieved if the collisions are head-on. This option could be applied in cases when the bunches are spaced enough so that there are not parasitic collisions.

Head-on collisions are used in the heavy ion collider RHIC at BNL – [87]. The interaction region of RHIC is shown on Fig. 94.

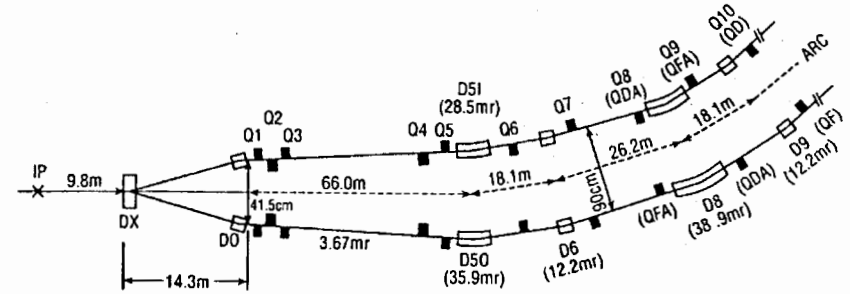


**Fig. 94.** Optics of RHIC interaction region – [87]

RHIC collides bunched beams with the same horizontal and vertical transverse emittances. The number of bunches is 56. Each bunch has  $1 \times 10^9$  ions. The bunches are spaced by 63.9 m.

In RHIC the final focusing is done by a quadrupole triplet (Q1, Q2, Q3) and doublet (Q4, Q5). As RHIC supports the possibility to collide beams with ions of different species these quadrupoles are separate for each ring.

Two common DX dipoles split the colliding beams. The free space around IP for installing detectors is 17.2 m. In IP the two colliding beams have the same focusing properties. In IP  $\alpha^* = 0$  (waist),  $D^* = 0$  (dispersion free) and  $\beta^*$  is changed from 10 m during injection and acceleration to 1 m during the collisions. The RMS bunch length  $\sigma_x$  is kept by the storage RF system much shorter than  $\beta^*$ .

The optical functions in the RHIC interaction region are shown on Fig. 95.

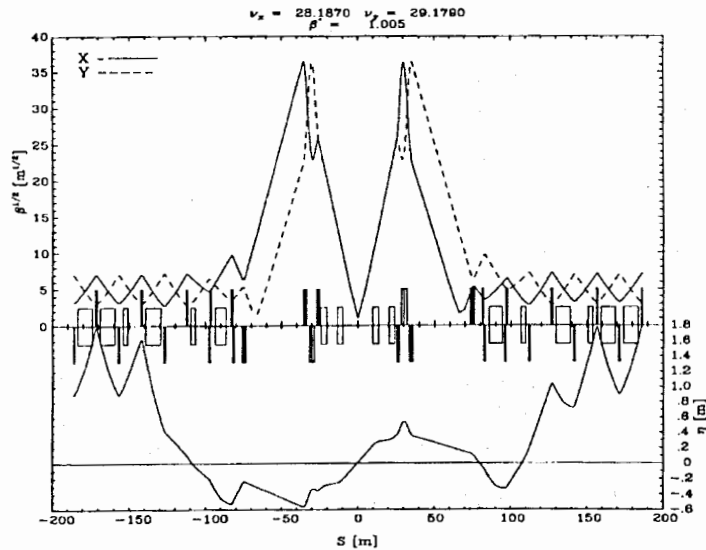


Fig. 95. Optical functions at RHC interaction region – [87]

If the collisions are head-on and the bunch spacing is smaller than the interaction region length parasitic collisions between bunches will take place. When the bunches of one of the beams approach IP or leave it they will meet the bunches of the counter-rotating beam at intervals equal to half of the bunch spacing. To reduce the effect of parasitic collisions a non-zero crossing angle  $\theta_c$  between the two colliding beams is introduced – Fig. 96.

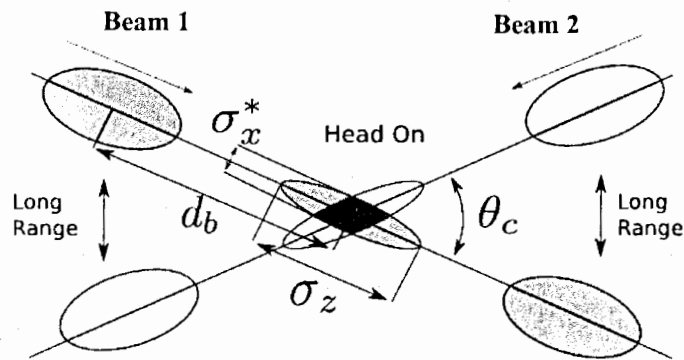


Fig. 96. Colliding beams with a crossing angle – [165]

The parasitic collisions on either side of IP are now replaced by long range interactions. In practice beam separation by  $10\sigma_x$  is acceptable. Introducing a non-zero crossing angle reduces the luminosity (115) by a factor:

$$F(\theta_c, \sigma_x, \sigma_s) = \frac{1}{\sqrt{1 + \left(\frac{\theta_c \sigma_s}{2\sigma_x}\right)^2}} \quad (117)$$

For the operation of LHC with protons there are up to 2808 closely spaced bunches. For proton bunches  $\sigma_x^* = 16.7 \mu\text{m}$ ,  $\sigma_s = 7.7 \text{ cm}$ ,  $\theta_c = 285 \mu\text{rad}$  and therefore  $F = 0.835$ . There are 30 long range interactions per insertion.

For operation with fully stripped lead ions however the number of bunches for the nominal ion scheme is “only” 592 with  $7 \times 10^7$  ions/bunch,  $\sigma_s = 7.94 \text{ cm}$ ,  $\sigma_x^* = 15.9 \mu\text{m}$  ( $\beta^* = 0.5 \text{ m}$ ) – [64]. Due to the relatively low intensity of the ion beams and to the much larger spacing of the ion bunches compared with proton ones the beam-beam effects in colliding ion beams will be rather weak. Therefore separation of the beams around the IP would not be necessary and we could work with a zero crossing angle. However the parasitic head-on beam-beam interactions will reduce the beam-beam lifetime and will be a source of background radiation.

In LHC collisions between ion beams will take place principally at IP2, where the ALICE detector is installed. The total separation of the ion beams at IP2 is a superposition of the vertical bump provided by the magnetic field of the ALICE spectrometer and the external vertical bump. Several scenarios have been considered – Fig. 97. In the upper separation scheme the crossing angle is  $\theta_c = 81 \mu\text{rad}$ . It provides separation of  $7\sigma_y$  at the first parasitic collision. In the lower scheme the crossing angle is almost zero.

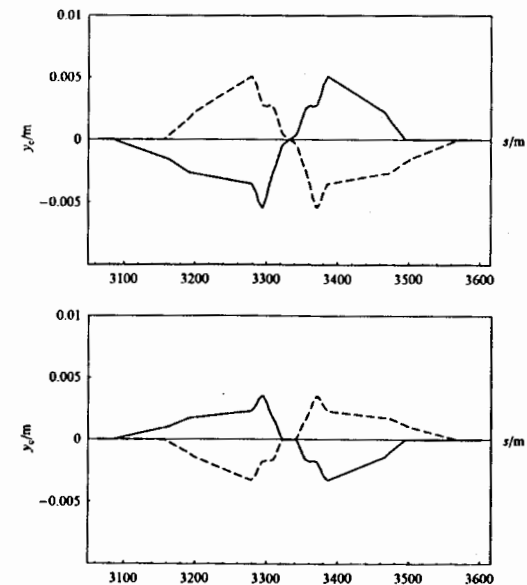


Fig. 97. Separation of LHC lead ion beams around IP2. The vertical trajectory of Beam 1 is represented by a solid line, while that of Beam 2-by a dashed line – [64]

Another phenomenon that could reduce the collider luminosity is the so-called “hour glass effect”. The origin of this effect is in the fact that in the interaction region the rms beam size depends on the longitudinal position:

$$\sigma(s) = \sigma^* \sqrt{1 + \left(\frac{s}{\beta^*}\right)^2}. \quad (118)$$

Hour glass effect is significant for long bunches and small  $\beta^*$ . The luminosity is reduced by a factor  $H\left(\frac{\beta^*}{\sigma_s}\right)$ :

$$L(\sigma_s) = L(0) \cdot H, \quad (119)$$

$$H\left(\frac{\beta^*}{\sigma_s}\right) = \sqrt{\pi} \left(\frac{\beta^*}{\sigma_s}\right) \exp\left(-\left(\frac{\beta^*}{\sigma_s}\right)^2\right) \operatorname{erfc}\left(\frac{\beta^*}{\sigma_s}\right). \quad (120)$$

In ion colliders  $\sigma_s \ll \beta^*$  and the hour glass effect has a little influence on the luminosity.

### 11.5.2. Beam-Beam Interaction

The particles in the collider see the electromagnetic field produced by the counter-rotating beam – [163]. This phenomenon is known as beam-beam interaction and it is one of the main limiting effects on the collider performance. The beam-beam interaction is extremely nonlinear. The linear part of the interaction acts like a quadrupole and gives rise to a linear tune shift – Fig. 98. For the case of head-on interactions and round beams with Gaussian bunches the linear beam-beam tune shift is given by:

$$\xi_{HO} = \Delta Q_{HO} = \frac{N_B r_i}{4\pi \epsilon_N}, \quad (121)$$

where  $r_i$  is the classical ion radius and  $\epsilon_N$  is the normalized emittance.

The quantity  $\xi$  is known as “linear beam-beam parameter”.

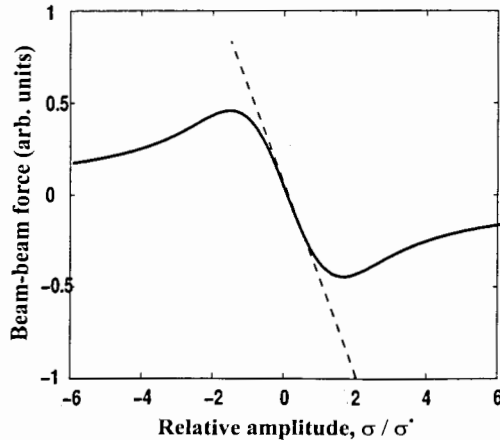


Fig. 98. Beam-beam force for round beams; dashed line represents the linear approximation

It turns out that the nonlinear part of the beam-beam force is also proportional to the quantity  $\xi$ . In RHIC the beam-beam parameter  $\xi_{HO} = 0.002$  is small compared to hadron colliders and does not limit the collider performance.

Due to the nonlinear character of the beam-beam force the beam-beam tune shift becomes amplitude dependent – Fig. 99.

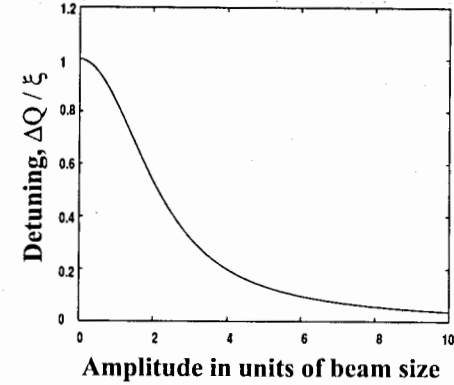


Fig. 99. Nonlinear beam-beam detuning as a function of the test particle amplitude for round beams – [163]

The tune shift for long range beam-beam interactions is given by:

$$\Delta Q_{lr} = \frac{r_i N_b}{2\pi \beta_y \theta_y^2 \beta^*}. \quad (122)$$

Combining (115) and (121) we will receive:

$$L = \frac{\beta_y \xi}{2r_i \beta_y^* \Delta t} \frac{1+k}{\Delta t} N_B, \quad (123)$$

where:  $k = \frac{\sigma_x^2}{\sigma_y^2}$  is the aspect ratio at the collision point, for round beams  $k=1$ ,

$\Delta t = \frac{1}{Bf_{rev}}$  is the bunch spacing in s.

The last factor in (123) is the total beam current. As the value of the beam-beam tune shift is limited it follows from (123) that we can increase the collider luminosity by reducing the value of the beta-function at IP and/or increasing the number of ions per bunch and the number of bunches. Thus for increasing the RHIC luminosity four times to  $L=8 \cdot 10^{26} \text{ cm}^{-2} \cdot \text{s}^{-1}$ , averaged over 10 h storage time, the number of bunches in each ring will be doubled to 112 (100 ns bunch spacing) and  $\beta^*$  will be reduced from the design value of 2 m to 1m.

In colliders two models of beam interactions are applied.

In ion colliders the so-called strong-strong interaction model is used. In this model both beams are affected and change by the beam-beam interaction.

In the second model, called weak-strong, only one of the beams (the weak one) is affected and changed by the beam-beam interaction while the other beam (the strong one) is kept unchanged. This scheme is appropriate for proton-antiproton colliders (Tevatron, SpS).

### II.5.3. Luminosity Lifetime

The luminosity decreases during the storage time from the peak value due to loss of particles and emittance blow up. Many processes as synchrotron radiation damping, intrabeam scattering (IBS), RF noise, multiple scattering on molecules of the residual gas result in evolution of the beam emittances. Particles are lost when the beam dimensions exceed the magnet aperture or the RF bucket area. Beam-beam interactions could also be a source of particle losses.

In RHIC the luminosity lifetime is determined by the intrabeam scattering which results in emittance blow up and loss of particles when the bunch area grows beyond the bucket area. The luminosity lifetime of gold beams is 10 h which leads to an average luminosity of  $2 \times 10^{26} \text{ cm}^{-2} \cdot \text{s}^{-1}$  – Fig. 100.

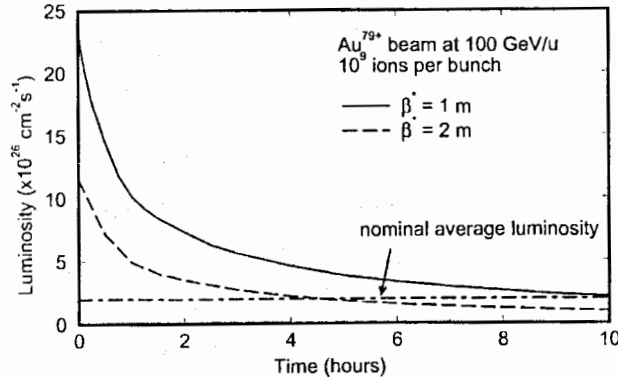


Fig. 100. Reduction of RHIC luminosity caused by IBS – [87]

Ultra-relativistic ion beams in storage rings are source of synchrotron radiation with considerable power. On one hand the synchrotron radiation is a sizable heat load on the cryogenic system. On the other hand radiation damping has significant effect on the beam dynamics. LHC is the first heavy ion collider in which synchrotron radiation plays an important role.

Calculations show that for the nominal ion scheme at collision energy the power of the synchrotron radiation in LHC per ring will be 83.9 W. The radiation damping time scales as  $A^4/Z^5$  and for lead ions is compatible with the growth time due to intrabeam scattering. While for horizontal emittance the radiation damping time at collision mode is 12 h the horizontal emittance growth time due to IBS is 13 h. For the longitudinal emittance the figures are respectively 6.3 h and 7.7 h.

If there were not radiation damping after few hours the transverse emittance would exceed the acceptance leading to beam losses – Fig. 101. It is radiation damping in LHC that cancels the effect of intrabeam scattering and thus allowing collider to work with high luminosity [164].

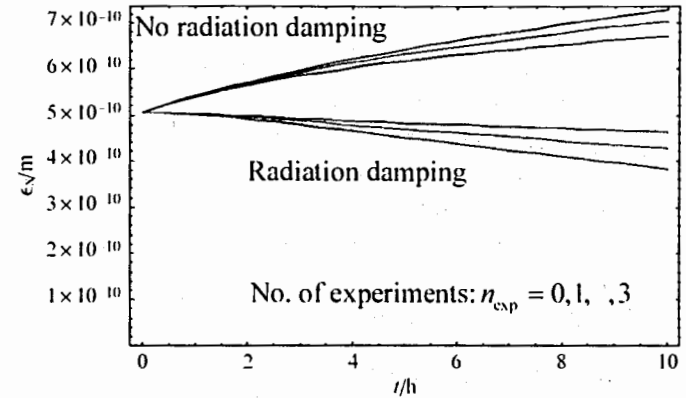


Fig. 101. Evolution of the LHC horizontal emittance due to radiation damping and intrabeam scattering – [164]

In ion colliders with very high energy of the beams, like LHC, the main source of particle losses are the electromagnetic processes in ion collisions – [64]. These processes have been described in 1.2.5. In the ECPP process a secondary beam of  $^{208}\text{Pb}^{81+}$  ions is generated while in EMD process the secondary beam is of the lighter isotope of lead  $^{207}\text{Pb}^{82+}$ . Both these beams are lost some distance downstream from the IP. Luminosity lifetime for the nominal ion scheme has been estimated to be 5.6 h – [64], accounting beam-beam, radiation damping and IBS effects.

Cooling of the colliding ion beams could counteract emittance growth due to IBS and beam-beam interaction and thus increase the luminosity and the luminosity lifetime. For example a ten times increase of the RHIC average luminosity, to  $L=7 \cdot 10^{27} \text{ cm}^{-2} \cdot \text{s}^{-1}$ , could be achieved by electron cooling at collision energy – [166, 167]. The electron cooling will suppress the emittance growth due to IBS. Electron beams with 54 MeV electrons and 200 mA average current will be necessary. The electrons could be accelerated by a linear accelerator (bunched electron beam). As the power of the electron beam will be very high-10.8 MW, this must be an energy-recovering linac (ERL). To avoid the recombination of the electrons with the gold nuclei the electron beam must be magnetized. The magnetization with 1T magnetic field in the cooling section will increase the transverse electron temperature to 1000 eV.

In the ion collider NICA to increase the peak luminosity and the luminosity lifetime electron and stochastic cooling will be applied – [168]. When the equilibrium between intrabeam scattering and cooling is reached the luminosity lifetime will be determined by the interaction of the ions with the residual gas. The electron cooling will be used in the energy range 1-3 GeV/u while the stochastic cooling in the range 3-4.5 GeV/u.

## References

1. Keller R.// GSI Annual Report 1987, p. 360.
2. Reich H., Oks E.M., Spädike P.// Rev. Sci. Instrum., v.71, 2000, p. 707.
3. Leitner D, Lyneis C.M.// Proc. of 2005 Part. Accel. Conf., Knoxville, Tennessee, p. 179.
4. Beebe E., Alessi J., Kponou A., Pikin A., Prelec K.// Proc. Europ. Part. Accel. Conf., EPAC'02, Paris, 2002, p. 281.
5. Donets E.D.// Rev. Sci. Instrum., v. 71, 2000, p. 810.
6. Franzke B. SIS Parameter List. GSI-SIS-TH/87-13, Darmstadt, 1987.
7. Blasche K, Franzke B.// Proc. of Europ. Part. Accel. Conf., EPAC'94, London, 1994, p. 133.
8. Ratzinger U.// Proc. of Europ. Part. Accel. Conf., EPAC'00, Vienna, 2000, p. 98.
9. Conceptual Design Report (CDR) "An International Accelerator Facility for Beams of Ions and Antiprotons", GSI, 2001.
10. FAIR Baseline Technical Report, GSI, 2006.
11. Harrison M.// Proc. of the 1999 Part. Accel. Conf. (PAC'99), New York, 1999, pp. 6-10.
12. Roser Th.// Proc. of the 2005 Part. Accel. Conf. (PAC'05), Knoxville, Tennessee, pp. 358- 362.
13. Fischer W.// Proc. of Europ. Part. Accel. Conf. (EPAC'06), Edinburgh, 2006.
14. Zhao H.W.// Proc. of the First Int. Part. Accel. Conf. (IPAC'10), Kyoto, 2010, pp. 31-35.
15. Chanel M.// Proc. of Europ. Part. Accel. Conf., EPAC'02, Paris, 2002.
16. Beuret A. et al.// Proc. of Europ. Part. Accel. Conf., EPAC'04, Lucerne, 2004, p. 1153.
17. Kovalenko A.D.// Proc. of Europ. Part. Accel. Conf., EPAC'00, Vienna, 2000, p. 554.
18. Conceptual Design Report of Nuclotron-based Ion Collider Facility (NICA). JINR, Dubna, 2009.
19. Fischer W.// Proc. of Europ. Part. Accel. Conf., EPAC'06, Edinburgh, 2006.
20. Donets E.E, Donets E.D., Syresin E.M.// Proc. of Russian Part. Accel. Conf., RuPAC – XIX, Dubna, 2004, p. 453.
21. Bohr N.// Kgl. Danske Videnskab. Mat., Fys., Medd, v. 18, No. 8, 1948.
22. Nikolaev V.S., Senashenko V.S., Sidorovich V.A., Shafer V.Yu.// Zh. Techn. Fiz., v.48, 1978, p. 1399.
23. Franzke B.// IEEE Trans. Nucl. Sci., v. NS-28, 1981, p. 2116.
24. Madsen N. Preprint CERN, PS/DI Note 99-21, 1999.
25. Smolyakov A., Spiller P. Preprint GSI, 51-1, 2006, Darmstadt.
26. Bransden B.H.// Atomic Collision theory. 2<sup>nd</sup> ed., Benjamin Press, 1983.
27. Oppenheimer J.R.// Phys. Rev., v.31, 1928, p. 349.
28. Schlachter A.S., Stearns J.W., Graham W.G., Berkner K.H., Pyle R.V., Tanis J.A.// Phys. Rev., v.A27, 1983, p. 3372.
29. Warner D.(editor). CERN Heavy-Ion Facility Design Report. CERN-93-01, Geneva, 1993.
30. Roser T., Ahrens L.A., Hseuh H.C.// Fourth Europ. Part. Accel. Conf., EPAC'94, London, 1994, p. 2441.
31. Teplova Ya.A., Dmitriev I.S., Belkova Yu.A.// Nucl. Instr. Methods, v. B164-165, 2000, p. 291.
32. Nikolaev V.S.// Uspekhi Fiz. Nauk, v.85, 1965, p. 679.
33. Betz H.D.// Rev. Mod. Phys., v.44, 1972, p. 465.
34. Fettouhi A. PhD Thesis, Giesen, 2006.
35. Toleberger P., Wegner H.E., Alonso J., Gould H., Munger C., Anholt R., Meyerhof W.E.// IEEE Trans. Nucl. Sci., v. NS-32, 1985, p. 1767.
36. Nikolaev V.S., Dmitriev I.S.// Phys. Lett., v.28A, 1968, p. 277.
37. Roser T.// Fourth Europ. Part. Accel. Conf., EPAC'94, London, 1994, p. 151.
38. Bethe H.A., Ashkin J.// Experimental Nuclear Physics (ed. E. Segre), vol.1, John Wiley, NY, 1959.
39. Rozet J.P., Stephan C., Vernhet D.// Nuclear Instruments and Methods, v. B107, 1996, p. 67.
40. Joy J.// Nucl. Instr. Methods, v. 106, 1973, p. 237.
41. Franzke B.// CAS – Fourth Adv. Accel. Phys. Course, Noordwijkerhout, Netherlands, 1991 (CERN 92-01), p. 100.
42. Hedblom K., Frissel D.L.// Sixteenth Particle Accelerator Conference, Dallas, 1995, p. 1861.
43. Gröbner O., Calder R.// Part. Accel. Conf., San Francisco, 1973, p. 760.
44. Fischer E.// IEEE Trans. Nucl. Science, v. NS-24, No 3, 1977, p. 1227.
45. Gröbner O. Dynamic outgassing in CAS Vacuum Technology, Sneeversten, Denmark, CERN 99-05, 1999.
46. Mahner E., Hansen J., Laurent J.M., Madsen N.// Phys. Rev. ST-AB, v. 6, 2003, p. 013201.
47. Zhang S.Y., Ahrens L.A.// Part. Accel. Conf., New York, 1999, p. 3294.
48. Kramer A., Boine-Frankenheim O., Mustafin E., Reich-Springer H., Spiller P.// Proceedings of Eurp. Part. Accel. Conf. EPAC'02, Paris, 2002, p. 2547.
49. Fisher W. et al.// Proceedings of Eur. Part. Accel. Conf. EPAC'02, Paris, 2002, p. 1485.
50. Hseuh H.C., Smart L.A., Zhang S.Y.// Proceedings of Eur. Part. Accel. Conf. EPAC'02, Paris, 2002, p. 2559.
51. Zhang S.Y. BNL Preprint, C-A/AP/190, 2005.
52. Collins I.R., Gröbner O., Malyshev O.B., Rosi A., Strubin P., Veness R.// Int. Workshop on Performance Improvements of e<sup>+</sup>e<sup>-</sup> Factories, KEK, Japan, 1999.
53. Bruck H., Le Duff J.// Int. Conf. on High Energy Accelerators, Frascati, 1965.
54. Piwinsky A.// Proc. CERN Accel. School, CERN 92-01, Gif-sur-Yvette, Paris, 1984, p. 405.
55. Sorensen A.// CAS, Second General Accel. Phys. Course, Aarhus, 1986, p. 135.
56. Fedotov A.V. BNL Preprint, C-A/AP/168, Upton, NY, 2004.
57. Martini M. CERN Preprint, PS/84-9, Geneva, 1984.
58. Bjorken J., Mtingwa S.// Part. Accel., v.13, 1983, p. 115.
59. Meshkov I., Sidorin A., Smirnov A., Trubnikov G., Fedotov A. Physics guide of BETACOOOL code. Version 1.1. BNL report C-A/AP/262, 2006.
60. Parkhomchuk V., Ben-Zvi I. BNL, C-A/AP/47, 2001.
61. Wei J.// Proc. 1993 Part. Accel. Conf., Washington, 1993, p. 3651.
62. Fischer W., Connolly R., Tepikian S., van Zeijts J., Zeno K.// Proc. of Europ. Part. Accel. Conf., EPAC'02, Paris, 2002, p. 236.
63. Fischer W.// 2005 Part. Accel. Conf., Knoxville, Tennessee, 2005, p. 122.
64. The LHC Design Report (Chapter 21), CERN-2004-003, Geneva, 2004.
65. Prost L.R. et al.// Proc. of RuPAC'06, Novosibirsk, 2006, pp. 28-30.
66. Zimmermann F.// Proc. of 2001 Part. Accel. Conf., Chicago, 2001, pp. 666-670.
67. Arduini G.// Proc. of Europ. Part. Accel. Conf. EPAC'2002, Paris, 2002, pp. 94-98.
68. Blaskiewicz M.// Proc. of the 2003 Part. Accel. Conf., Portland, Oregon, 2003, pp. 302-306.
69. Irizo Ariz U. PhD Dissertation, Univ. of Barcelona, 2005.
70. Budker G.I., Dimov G.I., Dudnikov V.G., Sokolov A.A., Shamovsky V.G.// Sixth Int. Conf. on High En. Accel., Cambridge, Massachusetts, 1967.

71. *Hereward H.G.* CERN Preprint, CERN 71-15, Geneva, 1971.
72. *Keil E., Zotter B.* CERN Preprint, CERN-ISR-TH-71-58, Geneva 1971.
73. *Grobner O.* // Proc. of 1997 Part. Accel. Conf., Vancouver, 1997, pp. 3589-3591.
74. *Blackiewicz M., Furman M.A., Pivi M., Macek B.J.* // Phys. Rev. ST-AB, v. 6, 2003, p. 014203.
75. *Grobner O.* // Proc. of 10<sup>th</sup> Int. Conf. on High En. Accel., Protvino, 1977.
76. *Ohmi K.* // Phys. Rev. Letters, v.75, 1995, p. 1526.
77. *Arduini G. et al.* // Proc. of 2001 Part. Accel. Conf., Chicago, 2001.
78. *Furman M., Pivi M.* Report of LBNL, LBNL-52872/CBP/Note 516, 2003.
79. *Blackiewicz, Irizo U.* BNL Report, C-A/AP/260, 2006.
80. *Shulte D., Zimmermann F.* // 31<sup>st</sup> ICFA Beam Dynamics Workshop: Electron Cloud Effects (E-CLOUD'04), Napa, California, 2004.
81. *Zhang S.Y. et al.* // Proc. of 2003 Part. Accel. Conf., Portland, Oregon, 2003, p. 54-56.
82. *Iriso-Ariz U. et al.* // Proc. of 2003 Part. Accel. Conf., Portland, Oregon, 2003, pp. 797-799.
83. *Jowett J.M. et al.* // Proc. of Europ. Part. Accel. Conf., EPAC'04, Lucerne, 2004, p.578.
84. *Meier H. et al.* // Phys. Rev. A, v. 63, 2001, p. 032713.
85. *Pshenichnov I.A., Bondorf J.P., Mishustin I.N, Venture A., Nasetti S.* // Phys. Rev. C, v. 64, 2001, p. 024903.
86. *Roszbach J, Schmuser P.* // Basic Course on Accelerator Optics. CAS-Fifth General Accelerator Physics Course, Javaskyla, 1992, pp. 19-88.
87. *Hahn H. et al.* // Nucl. Instr. and Meth., v. A499, 2001, pp. 245-263.
88. *Spiller P., Blasche K., Franczak B., Stadlmann J., Omet C.* Optimization of the SIS-100 Lattice and a Dedicated Collimation System for Ionization Losses // AIP Conf. Proc. 773 "High Intensity and High Brightness Hadron Beams", NY, 2005, pp. 40-44.
89. *Stadlmann J. et al.* // Europ. Part. Accel. Conf. EPAC'06, Edinburgh, 2006, pp. 214-216.
90. *Franczak B., Blasche K., Reich K.H.* // IEEE Trans. Nucl. Sci., v. NS-30, No 4, 1983, pp. 2120 – 2122
91. *Blasche K., Franczak B.* // Europ. Part. Accel. Conf., EPAC'92, Berlin, 1992, pp.9-13.
92. *Chanel M.* // Europ. Part. Accel. Conf., EPAC'02, Paris, 2002, pp. 563-565.
93. *Carli C., Belohitskii P., Chanel M, Pasternak J.* // Proc. of Europ. Part. Accel. Conf., EPAC'06, Edinburgh, 2006, pp. 261-263.
94. *Autin B.* // IEEE Trans. Nucl. Sci., v.NS-26, No 3, 1979, pp. 3493-3495.
95. *Rees G. H.* Injection. CAS-Fifth General Accelerator Physics Course, Yawaskyla, 1992.
96. *Anguelov V., Issinsky I.B., Kovalenko A.D, Mikhailov V.A., Monchinsky V.A., Seleznev V.V., Volkov V.I.* Development of the Beam Injection into the Nuclotron.
97. *Eickhoff H., Blasche K, Blell U., Franzke B., Pinkow J.* // First Europ. Part. Accel. Conf., EPAC'88, Rome, 1988.
98. *Reinstad D.* // Second Europ. Part. Accel. Conf., EPAC'90, Nice, 1990, p. 128.
99. *Van der Stok P.D.V.* // IEEE Trans. Nucl. Sci. v. NS-24, No 3, 1977, pp. 1417-1419.
100. *Bovet C., Lamotte D.* Preprint CERN, SI 69-13, Geneva, 1969.
101. *Anguelov V., Dinev D.* // Bulg. J. Phys., v. 23, 1996, p. 28.
102. *Blasche K., Franczak B.* // Third Europ. Part. Accel. Conf., EPAC'92, Berlin, 1992, pp. 9-13.
103. *Bär R., Blasche K., Eickhoff H., Franczak B., Hofmann I., Moritz P., Dolinski A., Dimnikov A.* // Proc. of Europ. Part. Accel. Conf., EPAC'98, Stockholm, 1998, p. 499.
104. *Tumov B.A., Шукейло И.А.* // Журнал технической физики, 1968, т. 38, стр. 1752.
105. *Gromov A.M., Cherenkov P.A.* // Thirteen Allunion Part. Accel. Conf., M., 1973, p. 110.
106. *Bryant P.J.* // CERN Accelerator School, 1999, p. 50.
107. *Roser T.* // Fourth Europ Part. Accel. Conf., EPAC'94, London, 1994, p. 151-155.
108. *Symon K.R., Sessler A.M.* // CERN Symposium on High Ener. Accel. and Pion Phys, 1956, Report CERN 56-26, v. 1, p. 44.
109. *Bruckner A. et al.* // Nucl. Instr. and Methods, 1970, v. 77, p. 78.
110. *Ciapala E.* // CAS-General Accelerator Physics Course, Gif-sur-Yvette, 1984, Report CERN 85-19, v. 1, p. 195.
111. *Montague D.W.* // First Int. School on Part. Accel., "Ettore Mayorana" Center, 1976.
112. *Bruck H.* // Accelateur circulaire des particules. Paris, Press Universitaires, 1966.
113. *Le Duff J.* // CERN Accelerator School, 1994, v.1.
114. *Lichtenberg A.J.* // Phase-Space Dynamics of Particles, NY, John Willey and Sons, Inc., 1969.
115. *Лебедев А.Н.* // Атомная Энергия, 1960, т. 9, стр. 189.
116. *Symon K. et al.* // Int. Conf. High Ener., Geneva, 1959, v. 1, p. 58.
117. *De Jonge M.J., Messerschmidt E.W.* // IEEE Trans. Nucl. Sci., 1973, v. NS-20, p. 796.
118. *Bisoffi G.* Ph. D. Thesis, Heidelberg Universitat, 1989.
119. *Eickhoff H., Beckert K., Franzak B., Franzke B.* // First Europ. Part. Accel. Conf., EPAC'88, Rome, 1988, pp. 1059-1060.
120. *Carly Ch., Mohl M.D.* // IEEE Trans. Nucl. Sci., 1998, pp. 976-978; CERN Preprint PS/AR/ Note 94-12, Geneva, 1994.
121. *Steck M., Groening L., Blasche K., Eickhoff H., Franczak B., Franzke B., Winkler T., Parkhomchuk V.V.* // Proc. 1999 Part. Accel. Conf., New York, 1999, pp. 1704-1706.
122. *Syresin E., Noda K., Shibuya S., Uesugi T.* // Proc. of Europ. Part. Accel. Conf., EPAC'06, Edinburgh, 2006, pp. 2907-2909.
123. *Grieser M., Habs D., Hahn R., Kleffner C., Repnow R., Stampfer M., Jaeschke E.* // Part. Accel. Conf., 1991, pp. 2817-2819.
124. *Hedblom K., Johansson A., Reistad D.* // Third Europ. Part. Accel. Conf., EPAC'92, Berlin, 1992, pp. 462-464.
125. *Abrahamsson K. et al.* // Third Europ. Part. Accel. Conf., EPAC'92, Berlin, 1992, pp. 441-443.
126. *Skrinsky A.N., Parkhomchuk V.V.* // Physics of Particles and Nuclei, v. 12, p. 579, 1981.
127. *Franzke B. et al.* // IEEE Trans. Nucl. Sci., 1993, pp. 1645-1649.
128. *Bhat C. M.* Preprint Fermilab, AB-FN-0916-AD, 2011.
129. *Steck M. et al.* // Proc. of COOL'11, Alushta, Ukraine, 2011, pp. 140-143.
130. *Rees G.H.* // Extraction. CAS-General Accelerator Physics Course, Gif-sur-Yvette, 1984 (CERN 85-19), p. 346.
131. *Pyka N., Blell U., Spiller P., Stadlmann J.* // Proc. of Europ. Part. Accel. Conf., EPAC'08, Genoa, 2008, pp. 3605-3607.
132. *Symon K.R.* Extraction of a Third Integral Resonance, I, II, III, IV. Fermi Lab. Notes, FN-130, 134, 140, 144, 1966.
133. *Teng L.C.* // Beam Extraction from a Circular Accelerator // AIP Conf. Proc., No 87, 1982, pp. 69-76.
134. *Badano L. et al.* Proton-Ion Medical Machine Study (PIMMS), Part I, CERN/PS 99-010 (D1), Geneva, 1999.
135. *Agapov N.N. et al.* // Part. Accel. Conf., PAC'01, Chicago, 2001, pp. 1646-1648.
136. *Volkov V.I. et al.* // Europ. Part. Accel. Conf., EPAC'04, Lucerne, 2004, pp. 2718-2720.
137. *Van der Meer S.* Preprint CERN, CERN/PS/AA Note 78-6, Geneva, 1978.
138. *Hardt W.* Preprint CERN, CERN/PS/DL/LEAR Note 81-6, Geneva, 1981.

139. *Cappi R., Giannini R., Hartd W.* Preprint CERN, CERN/PS/DL/LEAR 82-3, Geneva, 1982.
140. *Noda K. et al.*// Nucl. Instr. and Meth., v. A492, 2002, pp. 241-251.
141. *Hiramoto K., Tadokora M., Hirota J., Nishi N.*// Nucl. Instr. and Meth., v. A322, 1992, pp. 154-160.
142. *Feldbauer G., Benedikt M., Dorda U.*// Proc. of Int. Part. Accel. Conf., IPAC'2011, San Sebastian, 2011, pp. 3481-3483.
143. *Forck P., Eickhoff H., Peters A., Dolinskii A.*// Proc. of Europ. Part. Accel. Conf., EPAC'00, Vienna, 2000, pp. 2236-2238.
144. *Blell U. et al.*// Proc. of Part. Accel. Conf., PAC'07, Aluquerque, USA, 2007, pp. 17-169.
145. *Kirk M., Ondreka D., Spiller P.*// Proc. of Int. Part. Accel. Conf., IPAC'13, Shanghai, 2013, pp. 297-299.
146. *Badano L., Rossi S.* Preprint CERN, CERN/PS/97-019/DI, Geneva, 1997.
147. *Boine-Frankenheim O.* High power, high intensity hadron synchrotrons// CERN Accelerator School, Bilbao, May, 26, 2011.
148. *Dome G.* RF Systems: Waveguides and Cavities// AIP Conference Proceedings No. 153, New York, 1987.
149. *Klingbeil H.* Ferrite Cavities. arXiv:1201.1154v1 [physics.acc-ph] 5 Jan 2012.
150. *Schnase A.*// Cavities with a Swing. CAS- Radio Frequency Engineering, Seeheim, Germany, 3-16 May 2000.
151. *Mohite T.* Beam Loading Effect and Adiabatic Capture in SIS-18 at GSI. PhD Dissertation, Darmstadt, 2011.
152. *Ohmori C. et al.*//Proc. of 1999 Part. Accel. Conf., New York, 1999.
153. *Muramatsu R. et al.*// Proc. of 1999 Part. Accel. Conf., New York, 1999.
154. *Hofman A., Myers S.* Preprint CERN, CERN ISR-TH-RF/80-26, 1980.
155. *Ningel K.-P. et al.*// Proc. of Int. Part. Accel. Conf., IPAC'10, Kyoto, Japan, pp. 1420-1412.
156. *Huelsmann P.*//Proc. of Int. Part. Accel. Conf., IPAC'10, Kyoto, Japan, 2010, pp.744-746.
157. *Huelsmann R. et al.*// GSI Scientific Report , PNI-ACC-01, 2011.
158. *Harrison M., Peggs S., Roser T.*// Ann. Rev. Nucl. Part. Sci. 2002. 52:425-69.
159. *Ptitsyn V. et al.*//Proc. of Hadron Beam 2008, Nashville, Tennessee, USA.
160. *Boussard D., Linnekar T.* The LHC Superconducting RF Sytem. LHC Project Report 316, 1999.
161. *Boussard D. et al.*// Proc. of 1999 Part. Accel. Conf., New York, 1999, pp. 946-948
162. *Herr W., Muratori B.*// Concept of luminosity. CAS-Intermediate accelerator physics, Zeuthen, 2003, CERN-2006-002, 2006, p. 36.
163. *Herr W.*// Beam-beam interaction. CAS-Intermediate accelerator physics, Zeuthen, 2003, CERN-2006-002, 2006, p. 379.
164. *Manglunki D. et al.*// Proc. of Europ. Part. Accel. Conf., EPAC'08, Genoa, 2008, pp. 376-378.
165. *De Maria R.* LHC Interaction Region Upgrade. PhD thesis. Ecole Polytechnique Federal de Lausanne, 2008.
166. *Roser Th.*//Proc. of 2005 Particle Accelerator Conference, PAC'05. Knoxville, 2005, pp. 358-362.
167. *Ben-Zvi I.*// Proc. of 2005 Particle Accelerator Conference, PAC'05. Knoxville, 2005, pp. 2741-2743.
168. *Kozlov O. et al.*// Proc. of HB2012, Beijing, 2012, pp. 522-526.